INVESTIGATIONS OF STANDING HEAT LOSS FROM SOLAR DOMESTIC HOT WATER TANKS

Si Thu Paing

A thesis submitted to

Auckland University of Technology

in fulfilment of the requirements for the degree of

Doctor of Philosophy (PhD)

2022

School of Engineering, Computer and Mathematical Sciences

Abstract

Heat loss from vertical solar hot water storage cylinders is detrimental to their thermal performance. As such, many researchers devoted their attention to investigating changes in the rate of heat loss in response to different cylinder designs and initial temperature profiles. Despite the extensive literature relating to heat loss from vertical solar hot water storage cylinders, few studies have examined passive means of controlling the natural convection flow behavior inside the tank as it loses heat to the surroundings.

Based on this gap in our understanding, a preliminary study was performed to examine transient natural convection inside vertical hot water cylinders experiencing a standing heat loss using Computational Fluid Dynamics (CFD). The model was validated with experimental temperature measurements and boundary layer velocity measurements from Particle Image Velocimetry (PIV). From this, it was found that the natural convection heat transfer coefficient changed with time, partly due to the development of a thermocline in the tank.

Based on this observation, it was decided to decouple the natural convective heat transfer coefficient from time and the temperature profile in the cylinder by modelling it under a quasi-steady state condition. Using this approach, it was shown that natural convection heat transfer decreases with increases to the cylinder's aspect ratio. Furthermore, it allowed a generalized heat transfer correlation to be developed to describe the natural convection heat transfer inside the cylinder regardless of time or the temperature profile.

Over the course of these preliminary studies, it was apparent that the side wall boundary layer flow had a major impact on the natural convection heat transfer. As such, research was focused on attempting to control this flow. In the first instance, a series of cylindrical jacket-type baffles were placed inside the cylinder. It was shown how the baffle jacket was able to deliver a 40% reduction in the Nusselt number and led to an understanding of the baffle geometry best suited to this purpose. This led to the development of a generalized heat transfer correlation to determine Nusselt number inside tanks with baffle jackets as a function of the baffle's geometry and proportions.

Given the potential for simple baffle structures to reduce heat loss, it was decided to examine if another modification could also deliver an improvement: replacing the usual insulation material with a layer of trapped air (much like an inverted ThermosTM flask). Again, CFD was used to examine the flow in 'trapped' air gaps around the cylinder of between 10 and 100 mm. It was shown that increasing the aspect ratio of the inner cylinder (i.e. the storage tank) alters the flow behavior in the region intersecting the side and top air gap cavities. Because of this, convective heat transfer decreases as the aspect ratio increases. Based on the analysis, a heat transfer correlation that describes the change of the convective heat transfer coefficient with geometrical changes to the 'trapped' air insulation layer was developed.

Finally, using the correlations developed in this work, the long-term performance of a solar water heating system incorporating the studied storage cylinders was modelled analytically. The results indicate that a baffle jacket could improve the thermal performance by up to 3%, while the level of insulation provided by an air cavity could enhance the thermal efficiency by up to 8%. This indicates that the amount of traditional insulation required could potentially be reduced by using an air insulation layer.

In summary, this work has delivered an improved relationship for predicting the rate of natural convection heat transfer from vertical solar hot water storage cylinders, by developing a generalized correlation that can predict it irrespective of time or the

initial temperature profile. Furthermore, the work has shown that the use of a simple passive baffle that alters the natural convection flow inside a cylinder can reduce the heat loss in experiences. Finally, it was also found that, with good design, an air gap that serves as an insulation layer could also markedly reduce heat loss. It suggests that despite the mature nature of the technology, there may be opportunities to include simple design modifications that could lower capital costs without compromising the system's performance.

Contents

List of Tables

List of Figures

Attestation of Authorship

I hereby declare that this submission is my own work and that, to the best of my knowledge and belief, it contains no material previously published or written by another person nor material which to a substantial extent has been accepted for the qualification of any other degree or diploma of a university or other institution of higher learning.

_____

Signature of candidate

Publications

The following publications have been derived in whole or in part from the work contained within this thesis.

Journal Papers:

Paing, S. T., Anderson, T., & Nates, R. (2022). Reducing heat loss from solar hot water storage tanks using passive baffles. *Journal of Energy Storage*, *52*, 104807.

Conference Papers:

Paing, S. T., Anderson, T., & Nates, R. (2021). Estimation of natural convection heat transfer inside stratified vertical cylindrical solar storage tanks. *Proceedings of ISES Solar World Congress*, Virtual, December 2021.

Paing, S. T., Anderson, T., & Nates, R. (2019). Modelling and experimental validation of natural convection heat loss from a solar hot water storage tank. *Proceedings of Asia-Pacific Solar Research Conference*, Sydney, December 2019.

Acknowledgements

I am indebted to my supervisor, Dr. Timothy Anderson, for your valuable suggestions and guidance. I have benefited greatly from your wealth of knowledge in heat transfer, and concise writing style, which is something I hope to carry forward throughout my career. I am extremely grateful that you took me on as your doctoral student and continued to have faith in me over the years. I would also like to thank my co-supervisor Dr. Roy Nates for his patience, guidance, and support.

I gratefully recognize the invaluable help I received from my research colleagues, Djamal Benhadji, Delight Sedzro and Sulaiman Omar. Your encouraging words and thoughtful, detailed feedback have been very important to me during this journey.

Most importantly, I am grateful for my family's unconditional, unequivocal, and unparalleled support. Mom (Aung), thank you for being an inspiration for me to pursue Chemical Engineering in the first place, for your support, and for always believing in me over the years. Late Dad (Soe Paing), I do this in honour of you, and I will always love and miss you. I hope I am making you proud up there in heaven. Sister (Win Le' Yi Thant), thank you for always being there for me, for your support, and for believing in me during difficult times.

Nomenclature

A	Surface area	(m^2)
c_p	Specific heat capacity	$(J/kg \cdot K)$
D	Diameter	(m)
F'	Collector heat removal factor	
G	Incident solar radiation	(W/m^2)
g	Gravitational acceleration	(m/s^2)
H	Height	(m)
h	Convective heat transfer coefficient	$(W/m^2 \cdot K)$
$\bar{h}$	Average convective heat transfer coefficient	$(W/m^2 \cdot K)$
h_w	Wind induced heat transfer coefficient	$(W/m^2 \cdot K)$
k	Thermal conductivity	$(W/m \cdot K)$
L	Thickness	(m)
L_c	Characteristic length	(m)

l_b	Baffle jacket height	(m)
$\dot{m}$	Mass flow rate	(kg/s)
N	Number of glazing covers	
Nu	Nusselt number	
$\bar{Nu}$	Average Nusselt number	
P	Perimeter	(m)
Pr	Prandtl number	
q"	Surface heat flux	(W/m^2)
$\bar{q}$"	Average surface heat flux	(W/m^2)
$\dot{q}_{gen}$	Volumetric heat generation rate	(W/m^3)
$\dot{q}_{loss}$	Rate of heat loss	(W)
$\dot{q}_{rad}$	Radiation heat transfer rate	(W)
$\dot{q}_{useful}$	Collector useful energy gain	(W)
R	Thermal resistance	$(m^2 \cdot K/W)$
r	Radius	(m)
r_b	Radial position of baffle jacket	(m)
Ra	Rayleigh number (transient)	
Ra_A	Rayleigh number (air gap)	
$Ra_{i,gen}$	Rayleigh number (internal heat generation)	

Ra_T	Rayleigh number (isothermal)	
T	Temperature	$(^\circ C)$
T'	Reference temperature	$(^\circ C)$
T^o	Initial temperature	$(^\circ C)$
$\bar{T}$	Average temperature	$(^\circ C)$
T_{col}	Collector outlet water temperature	$(^\circ C)$
t	Time	(s)
U	Overall heat loss coefficient	$(W/m^2 \cdot K)$
U_L	Collector heat loss coefficient	$(W/m^2 \cdot K)$
V	Volume	(m^3)
v	Wind velocity	(m/s)
$(\tau\alpha)_T$	Transmittance-absorptance product of collector	
α	Thermal diffusivity	(m^2/s)
β	Volume expansion coefficient	$(1/K)$
ϵ_g	Glass cover emittance	
ϵ_p	Collector plate emittance	
ϵ_w	Tank wall emittance	
η	Storage tank thermal efficiency	
θ	Collector mounting angle	

υ	Kinematic viscosity	(m^2/s)
ρ	Density	(kg/m^3)
σ	Stefan-Boltzmann constant	$(W/m^2 \cdot K^4)$

Number Sets

$air, conv$	Convection inside air gap
air, rad	Radiation inside the air gap
b	Bottom wall
col	Solar collector
$edge$	Collector's edge
env	Ambient
$e, conv$	External convection oustide the tank
f	Fluid (water)
in	Collector inlet
ins	Insulation
ins, col, e	Insulation at the collector's edge
ins, col, b	Insulation at the collector's back
$ins, cond$	Conduction through the insulation
$i, conv$	Internal convection inside the tank
j	Intermediate node

L	Hot water load
n	Total number of intermediate nodes
p	Absorber plate
s	Side wall
sp	Seeding particles
t	Top wall
$total$	Total surface area of the wall
w	Wall
$w, cond$	Conduction through the wall
$w1$	Inner tank wall of the air gap
$w2$	Outer tank wall of the air gap

Chapter 1

Introduction

1.1 Overview

Today, one of the most critical challenges that humanity faces is to meet the growing energy demand. Heavy reliance on traditional fossil fuels such as coal, natural gas and crude oil to meet the energy demand raises concerns over running out of energy in the future if this continues since fossil energy is not unlimited. On top of that, fossil fuel is mainly utilized via direct combustion to produce electricity and thermal energy, which leads to adverse impacts on the environment including air pollution and greenhouse gas emission. Renewable energy with the benefits of unlimited resource and environmental friendliness can be the solution to overcome current environmental issues. Among the renewable energy sources, solar energy is recognized as one of the most promising sources because it supplies in the order of 3.78 million EJ that reaches the surface of the earth, which represents 6,500 times the global energy consumption of 580 EJ in the year 2018 (Kober et al., 2020).

1.2 Solar Energy

Solar energy that reaches to the surface of the earth by radiation can be harnessed to produce thermal energy using solar thermal collector or electricity using photovoltaic collector. The efficiency of solar thermal conversion is about 70% while the efficiency of solar electricity direct conversion system is still limited around 17% (Sadhishkumar and Balusamy 2014). Therefore, conversion of solar energy into thermal energy is more efficient and it is the most widely used method. Statistics shows that the global thermal capacity in operation had seen a growth from 62 GW in 2000 to 479 GW in 2019. The corresponding solar thermal energy yields amounted to 51 TWh in 2000 to 389 TWh in 2019, as shown in Figure 1 (Weiss and Spörk-Dür 2020).

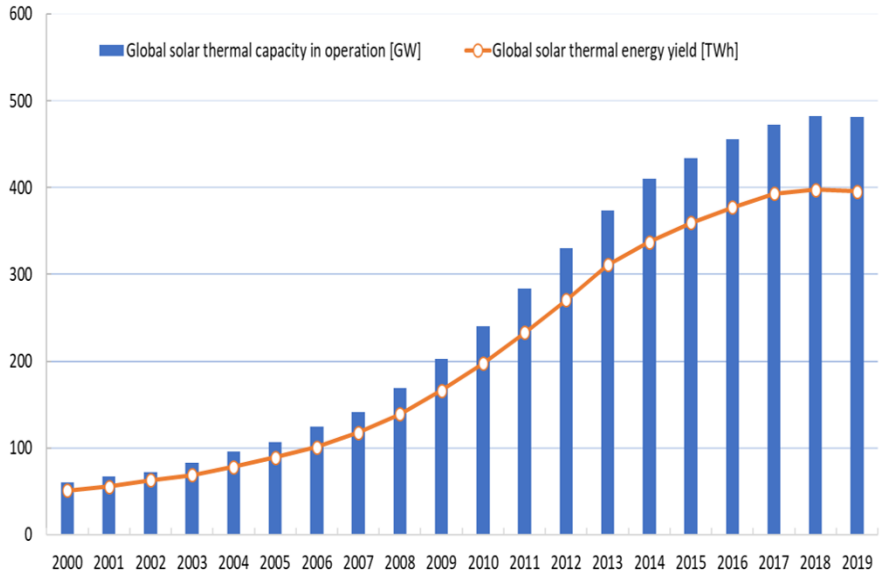

Figure 1: Global solar thermal capacity in operation and corresponding yields (adopted from Weiss and Spörk-Dür (2020))

1.3 Solar domestic hot water (SDHW) systems

Solar water heating systems harness solar energy to heat water which can be used to fulfill domestic hot water and space heating demands. A solar domestic hot water (SDHW) system shown in Figure 2 was developed by Kemp 1891, and consists of a solar collector connected through pipes to the storage tank to collect heat, which is often referred to as the solar heating loop. Similarly, a load loop consisting of pipes connecting the utility to the storage tank is also part of a SDHW system for hot water discharge. In addition to the collector and storage tank, a SDHW system often has an auxiliary energy backup heater to supply heat in periods where available solar energy is insufficient to heat the water to the required temperature. The auxiliary heating system can either be an electric heating element or a heat exchanger attached to an oil/gas burner. Depending on how water from the tank circulates through the collector to get heated, SDHW systems can be classified into active and passive systems.

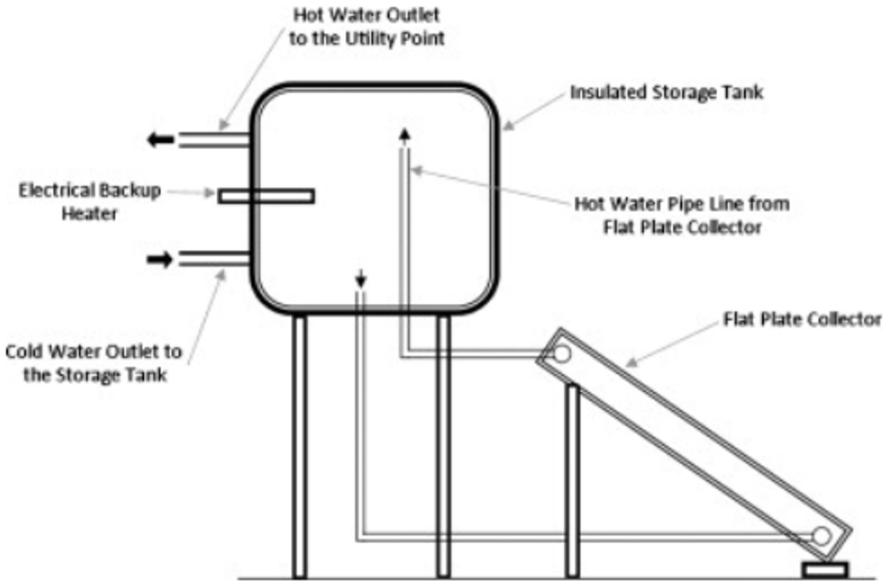

Figure 2: The first commercial solar water heater, “Climax” (adopted from Kemp 1891)

In passive systems, circulation of a heat transfer fluid is achieved through natural convection driven by the temperature difference between the hot and cold fluid in different parts of the system, hence these systems do not require pumps to function. Passive systems can be divided into two main categorizes, the integral collector storage (ICS) and the thermosyphon systems (Mekhilef et al., 2011).

Integral collector storage (ICS) systems incorporate both solar collector and storage tank into a single unit, as shown in Figure 3. Despite being one of the simplest forms of solar water heaters and cost effective due to the integration of the collector and tank in the same unit, ICS systems suffer from heavy heat losses during off-sunshine hours. To mitigate heat loss, insulating materials such as fiber glass, organic-based transparent foams, inorganic glass foams, and honeycomb structures can be used in different designs of ICS systems (Goetzberger and Rommel, 1987, Rehim, 1998).

In the late 19th century, ICS systems were supplanted by thermosyphon systems due to their issues regarding heat loss (Shukla et al., 2013). Thermosyphon systems, shown in Figure 4 circulate water between the solar collector and storage passively using natural convection. Heat absorbed from solar radiation by the collector raises the density of water in it, causing it to rise through the collector. Subsequently it enters the top of the tank which forces cold water from the bottom of the tank into the collector to take its place. To achieve this, the storage tank is required to be placed above the collector. This requirement often makes the installation of thermosiphon systems difficult given that domestic houses have limited roof space.

Although the concept of passive solar water heating systems is simple and requires less maintenance due to natural circulation of water based on buoyancy, Khalifa (1998) showed that active solar water heating systems have higher efficiencies, their values being 35–80% over that of the passive systems in the range of 30-50% (Nahar, 2002).

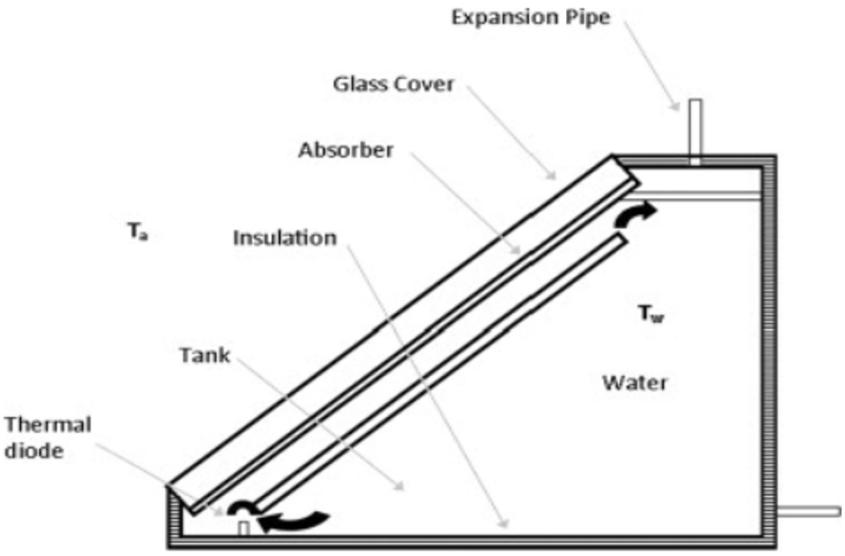

Figure 3: Integral collector storage solar water heating system (adopted from (Mohamad, 1997))

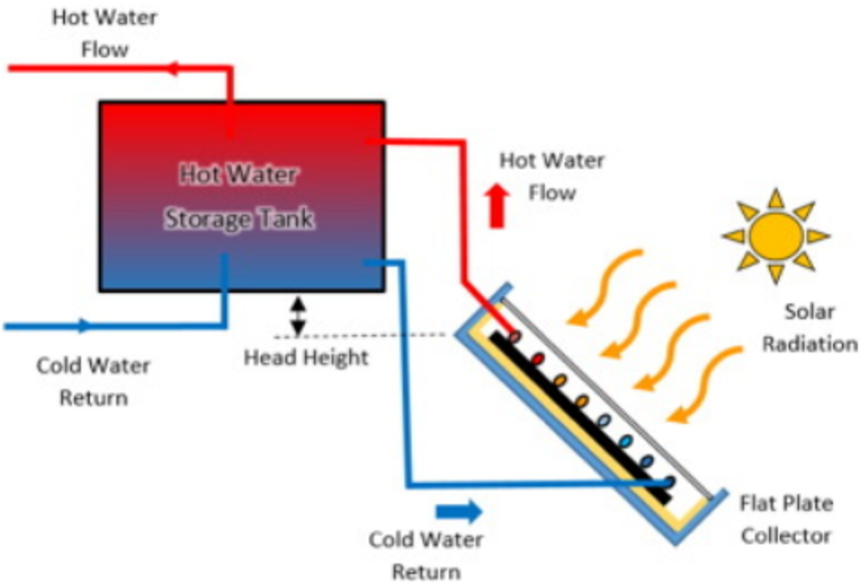

Figure 4: Schematic diagram of a typical passive solar water heating system (adopted from (Jamar et al., 2016))

In active systems, water is pumped from the storage tank to the collector during daytime when there is enough available solar energy to increase its temperature, and the heated water is then sent back to the tank for future use. Unlike passive systems, the collector can be installed separately from the storage tank and can be mounted either above or below the tank since a pump is used to circulate the water.

Active SDHW system can be designed to operate in either direct circulation in which water is circulated through a solar collector to receive heat or indirect circulation in which a suitable heat transfer fluid is circulated through a solar collector and a heat exchanger to indirectly heat the water (Li, 2016), as indicated in Figure 5.

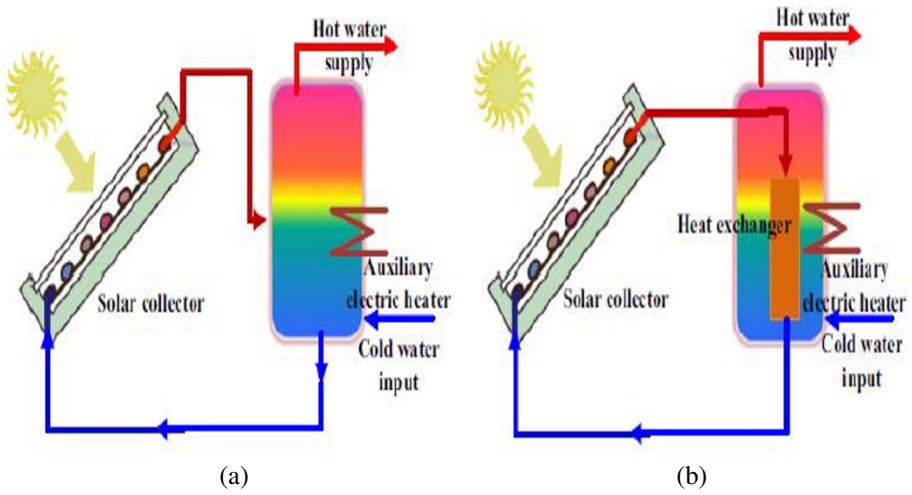

Figure 5: Schematic of active water heating systems (a) direct circulation, (b) indirect circulation (adopted from (Li, 2016))

Direct circulation systems are suitable for use in areas with ample sunshine and experience moderate ambient conditions because they are sensitive to freezing conditions For extreme weather conditions, freeze protection is usually provided by operating the system in drain-back mode, in which a differential controller-integrated pump is used to recirculate hot water from the tank to the solar collectors. For regions with less sunshine hours and extreme weather conditions, indirect heating systems are favorable because freeze protection of indirect circulation systems are more capable than direct circulation

systems since heat transfer fluids, such as water-ethylene glycol solution with a low freezing point, is used instead of water (Kalogirou, 2004). However, indirect circulation systems are costly to operate since the heat transfer fluid needs to be checked on an annual basis and replaced every few years, depending on the fluid quality and system temperatures achieved (Souliotis et al., 2009). Having said that, active direct circulation SDHW systems are still a preferable choice to indirect systems in moderate weather conditions because it requires neither a heat exchanger nor heat transfer fluid to operate which would otherwise increase both capital and operating costs.

1.4 Performance of active direct solar water heating system

A principal component of active direct solar heating system is the storage tank since it is responsible for storing the collected thermal energy from collectors. In this respect, thermal efficiency of the storage tank can have a marked influence on the efficiency of the whole system (Ghaddar, 1994).

The operation of hot water storage tank in a typical active direct SDHW system shown in Figure 5(a) is classified as charging, discharging and standby modes. During charging, water is circulated through a solar collector to receive heat, while stored hot water is transferred to the load, and equal amount of cold water is supplied to the tank during discharging. During periods when there is no charging or discharging taking place, the tank is in standby mode.

In an active direct SDHW system, water entering the tank falls or rises to a level where its density is equal to the density of surrounding water due to buoyancy. Therefore, water at different temperatures forms different layers along the height of a tank. Hotter water rises and accumulates at the top while cooler water drops and gathers at the

bottom leading to a phenomenon known as 'thermal stratification'. The degree of thermal stratification is often reflected by the thickness of the thermocline, the region between the hot and cold water, as shown in Figure 6. Mixing of incoming water with stored water during charging or discharging, heat conduction along the tank wall, heat conduction between layers of water at different temperatures, and heat loss to ambient all increase the thermocline thickness, thus influencing the stratification (Njoku et al., 2014).

During charging or discharging, studies have shown that the overall performance of a SDHW system can be significantly improved by having a high degree of thermal stratification inside the tank (Sheridan et al., 1967, Gutierrez et al., 1974, Fischer et al., 1978, Han et al., 1978, Sharp and Loehrke, 1979)). On this basis, several researchers have attempted to increase the extent of thermal stratification by exploring inlet and outlet ports' size and location (Lavan and Thompson, 1977, Jordan and Furbo, 2005), inlet pipe configuration or stratifiers (Zurigat et al., 1991, Shah and Furbo, 2003, Shah et al., 2005, Andersen et al., 2007, Andersen et al., 2008, Brown and Lai, 2011, García-Marí et al., 2013, Wang and Davidson, 2015, Moncho-Esteve et al., 2017, Wang and Davidson, 2017), baffle plates (Zachár et al., 2003, Altuntop et al., 2005, Bouhal et al., 2017) and tank shapes (Khurana et al., 2021).

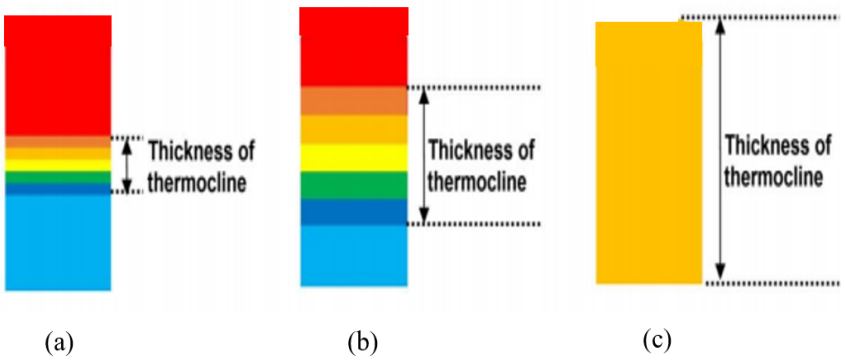

Figure 6: The degree of thermal stratification indicated by thermocline thickness (a) a highly stratified tank, (b) a moderately stratified tank, and (c) fully-mixed tank (Yu, 2020)

On the other hand, the performance of SDHW system can be improved by reducing standing heat loss to the ambient, which is pronounced during off-sunshine hours (particularly night standby mode) due to lower ambient temperature compared to daytime (Yang et al., 2019). Heat loss to the ambient takes place through a series of thermal resistances, as shown in Figure 7. Based on thermal resistances in Figure 7, it is obvious that heat conduction through the tank insulation can be easily controlled by varying insulation thickness and materials. As for convection heat loss from insulation to ambient, it is difficult to control since it is one of the environmental factors. However, natural convection thermal resistance between water and tank wall could be controlled based on the depth of understanding on its flow behavior. The extent to which heat loss affects the performance varies depending on the initial temperature profile (stratified or unstratified), which varies with charging and discharging process during the day.

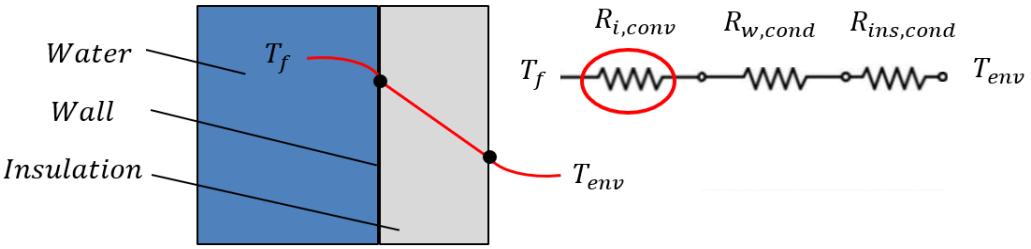

Figure 7: Thermal resistance network for static heat loss to the ambient

Knowing this, several researchers attempted to examine the natural convection flow inside vertical cylindrical tanks and its relation to thermal stratification for both initially stratified and unstratified temperature profiles.

Lin and Armfield (1999) numerically investigated transient cooling of an initially homogenous fluid inside a vertical cylindrical tank. Their numerical simulations revealed that vigorous flow activities take place in the vertical thermal boundary layer on the sidewall and the lower section of the tank, but a noticeable decrease in the intensity of both flows is observed due to gradual thermal stratification of fluid as the tank cools.

They managed to scale the time required for full thermal stratification of fluid with Rayleigh numbers and aspect ratios. Lin and Armfield (2001) later extended their study to investigate the transient cooling on rectangular and cylindrical enclosures in which the top and bottom walls were insulated, and treated as adiabatic, while the sidewalls were isothermally cooled. In their study, it was numerically shown that the time needed to reach full thermal stratification of fluid in the cylinder is faster than in the rectangular case, with the difference increasing with Rayleigh number. Lin and Armfield (2005) also investigated the long-term behavior of transient cooling on vertical cylinders for two cases; isothermal cold side wall with adiabatic end walls and isothermal cold walls with adiabatic top wall. They provided correlations to predict rate of natural convection heat transfer using scaling analysis.

From these previous studies, it is apparent that heat loss leads to the formation of thermal boundary layer flow on the sidewall which is part of the natural convection heat transfer inside a tank. Fan and Furbo (2012a) attempted to study the dependence of the boundary layer velocity on the vertical temperature gradient inside tanks subjected to natural convective cooling boundary condition on every wall. The authors found that there was a strong boundary layer flow with high velocity in tanks with initially weak thermal stratification (i.e. the temperature gradient smaller than 2 K/m). Moreover, a reduction in the boundary layer velocity with the progression of cooling time was noted due to decreased temperature difference between the tank and the ambient. They also developed an equation to predict the velocity of this buoyancy driven flow for a given vertical temperature gradient. Fan and Furbo (2012b) also showed that the volumetric flow rate of the boundary layer in a tank markedly decreases with increasing tank aspect ratio. The authors believed that this behavior is associated with increasing degree of thermal stratification with increasing aspect ratios, which suppresses the downward boundary layer flow.

Similarly, in an experimental study of cooling initially stratified vertical cylindrical

tank conducted by Jaluria and Gupta (1982), it was shown that buoyancy-induced maintains a layer of hot water at the top of the tank with almost no horizontal temperature gradient. In addition, heat loss to the ambient initially increased the temperature of cold layer of water at the bottom of the tank due to boundary layer flow, followed by an overall decrease in water temperature throughout the entire tank. The authors also reported the notable decrease in vigor of buoyancy-induced boundary layer flow compared to that of initially non-stratified tanks, owing to the initial existence of the thermal stratification.

1.5 Research question

Having examined the literature, it is apparent that there is an extensive body of work on improving the performance of storage tanks by providing means to maintain high degree of thermal stratification during charging or discharging process. Few of the existing studies examine how the natural convection flow behaves inside the tank as it loses heat to the surroundings, how can its heat transfer rate be estimated and passive means of controlling this. Given that this plays a strong part in the heat loss, there is still a need to improve our understanding of the flow behavior due to natural convection inside these tanks when they lose heat to the surroundings. By developing passive methods of reducing heat loss from these tanks, it may be possible to reduce their use of insulation materials while maintain their thermal performance.

- Therefore, this thesis asks: Can the estimation of standing heat loss from vertical solar storage water cylinders be improved, and are there passive ways to reduce these losses?

Chapter 2

Pilot study of transient natural convection

2.1 Introduction

In Chapter I, it was shown that heat loss to the ambient is one of the main factors that reduces the performance of solar water storage tanks. Standing heat loss to the ambient takes place through a series of heat transfer modes, as shown in Figure 8. The first resistance represents the natural convection heat transfer inside the tank due to temperature gradient between the water and the wall. Heat is then conducted through the tank wall and insulation before it is lost to the ambient. Although the thermal resistance to conduction through the tank wall and insulation can be easily estimated using Fourier's law (Cengel, 2004), the natural convection heat transfer resistance between the water and the wall (circled) is difficult to predict since there are only a limited number of studies that exist on understanding its relation to the rate of heat loss.

Given that the natural convection within a tank is essential in determining standing heat loss, it is important to understand its transient response to a change in tank wall temperature before attempting to predict it.

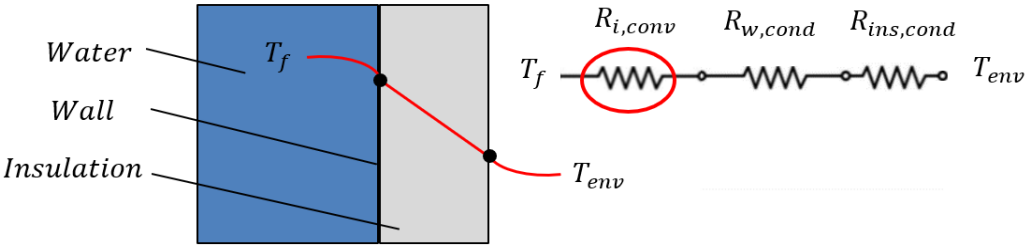

Figure 8: Thermal resistance network for static heat loss to the ambient

Otis and Roessler (1987) experimentally investigated transient cooling of gas in a vertical cylinder. The authors revealed the existence of internal waves and provided various time constants that characterize this complex process. Hyun (1984) conducted a numerical investigation on the development of transient flow and temperature fields of an initially unstratified fluid in response to a linearly heated side wall. The outcome of the study revealed that the primary flow is the clockwise circulation of fluid near the sidewall driven by boundary layer pumping due to cooling in the bottom section of the wall. It was also observed that the temperature at a given point in the core of the fluid is constant until the fluid that has progressed through the boundary layer returned to the interior. As a result, the fluid ahead of this boundary layer flow remain unstratified while the fluid behind is stratified. Similar flow behavior was observed by other studies (Kwak et al., 1998, Lim and Armfield, 1999, Lim and Armfield, 2001, Fan and Furbo, 2012a, Fan and Furbo, 2012b).

Studies on transient process of cooling down and stratifying an initially homogenous fluid by natural convection in a vertical cylindrical enclosure as it loses heat are still rare. Therefore, there is still a need to improve our understanding of this complex flow behavior of natural convection inside solar storage tanks when they lose heat to the surroundings.

2.2 Numerical method

The problem of natural convection heat transfer within enclosures is driven by density variations within a fluid body induced by heating or cooling conditions at the boundaries. Analytical solutions to these problems are considerably difficult to obtain due to the coupling of flow and heat transfer, and the complexity of the Navier-Stokes equations that govern these systems. As a result, many of the earliest studies have been based on experimental work (Chaney et al., 1984, Le Quere, 1990). However, with the rapid advent of computers over the past decade, computational modelling, especially computational fluid dynamics (CFD), has emerged to become a viable approach to not only solve problems in the area of fluid dynamics and heat transfer, but also assist researchers in evaluating different design parameters without the cost of performing numerous parametric experiments (Tu et al., 2018). Hence, it would appear to provide an opportune solution to understanding the heat loss from a water heater.

As the starting point for answering the research question, transient natural convection inside a vertical cylindrical storage tank was examined using a CFD approach. The aim of this was to develop an understanding of how natural convection flow, induced by standing heat loss, is developed inside a tank. To this end, a commercial computational fluid dynamics package, FLUENT was used to simulate the natural convection in a solar hot water storage tank in this study. FLUENT adopts the finite-volume approach which discretizes the computational domain into a finite number of control volumes in which the convective terms of the conservation equations are solved at the centroids. Interpolation is then used to approximate variables at the bounding surfaces as functions of centroid values of each control volume in the upstream since the convective properties and pressure on cell faces are largely dependent on upstream cell-centered values, especially in cases where dominant convection take place (Tsukaguchi et al., 2007).

Some commonly used interpolation methods for the convective terms include first or second order upwind, QUICK, Power Law and hybrid schemes each of which is derived based on different weightings on the effect of the upstream cells. Similarly, common interpolation methods for pressure include PRESTO, second order and body-force weighted algorithms. Prior to using the above-mentioned interpolation methods to approximate cell face values of convective terms however, the velocity field in the flow domain that is coupled to the pressure distribution, is required. Given that no general equation that relates the pressure to velocity exists, both fields need to be solved iteratively in such a way that the resulting velocity distribution computed from corrected pressure field satisfies continuity. Well-known algorithms that are used to resolve the coupling between the pressure and velocity fields include SIMPLE, SIMPLC and PISO. The output from interpolation of transport properties consists of a system of linear algebraic equations which can be solved either sequentially using a segregated solver or computed simultaneously with the help of coupled solver (Tsukaguchi et al., 2007).

In this chapter, convective terms were discretized using the second order upwind method while the pressure-velocity coupling was handled with the SIMPLE algorithm (Fan and Furbo, 2012a, Li et al., 2018). Interpolation of pressure was realized using a body-force weighted scheme, since it computes the pressure on cell faces by considering the influence of buoyancy-driven body forces on pressure (Tsukaguchi et al., 2007). The resulting equations were solved with the segregated solver for all the numerical simulations, in the case of FLUENT, the iterative point-implicit Gauss-Seidel method with Algebraic Multi Grid (AMG) (Hutchinson and Raithby, 1986).

To simulate transient heat loss from a fully mixed vertical cylindrical tank, a three-dimensional cylindrical tank model was developed using the CFD code, ANSYS Fluent 18.2. The computational domain consists of a fluid (water) domain and solid (tank) domain of 3 mm thick stainless-steel tank walls. The dimensions of the chosen hot water cylindrical tank model are given in Table 1. Thermal properties of stainless steel

were adopted from ANSYS Fluent database. Given that a typical average daily hot water usage of one individual is about 50 L, this configuration is in line with the product manufacturing standard of AS/NZS2712 with hot water capacity up to 2 times the daily use for a single residence consisting of two people (SIA, 2004).

Table 1: Data related to the cylindrical tank model

Dimensions	
Hot water tank volume (m^3)	0.2
Tank height (m)	1.22
Tank inner diameter (m)	0.452
Tank wall thickness (m)	0.003
Aspect ratio	2.7
Stainless-steel thermal properties	
Density (kg/m^3)	8030
Specific heat capacity (J/kgK)	502.48
Thermal conductivity (W/mK)	16.27

As shown in Figure 9, most of the flow domain was paved with a coarse mesh with a maximum grid size of 15 mm. The regions close to the tank wall where concentrated grid points were created by inflating the grid with 10 layers having a first-layer thickness of 0.05 mm and a growth rate of 1.2. Figure 9 shows the mesh used for the developed CFD model.

Convective boundary conditions were imposed on the outer walls as well as the top and bottom ends with an external heat transfer coefficient of 10 W/m^2K used. This coefficient describes the situation experienced in the laboratory and it represents common practical situations (Cotter and Charles, 1993, Adhikari et al., 1995, Oliveski et al., 2003, Rodriguez et al., 2009). As the initial conditions, a water temperature of $62°$C and an ambient temperature of $23°$C were used throughout the simulation of a 6 hour standby period.

Since natural convection heat transfer is strongly coupled with buoyancy forces,

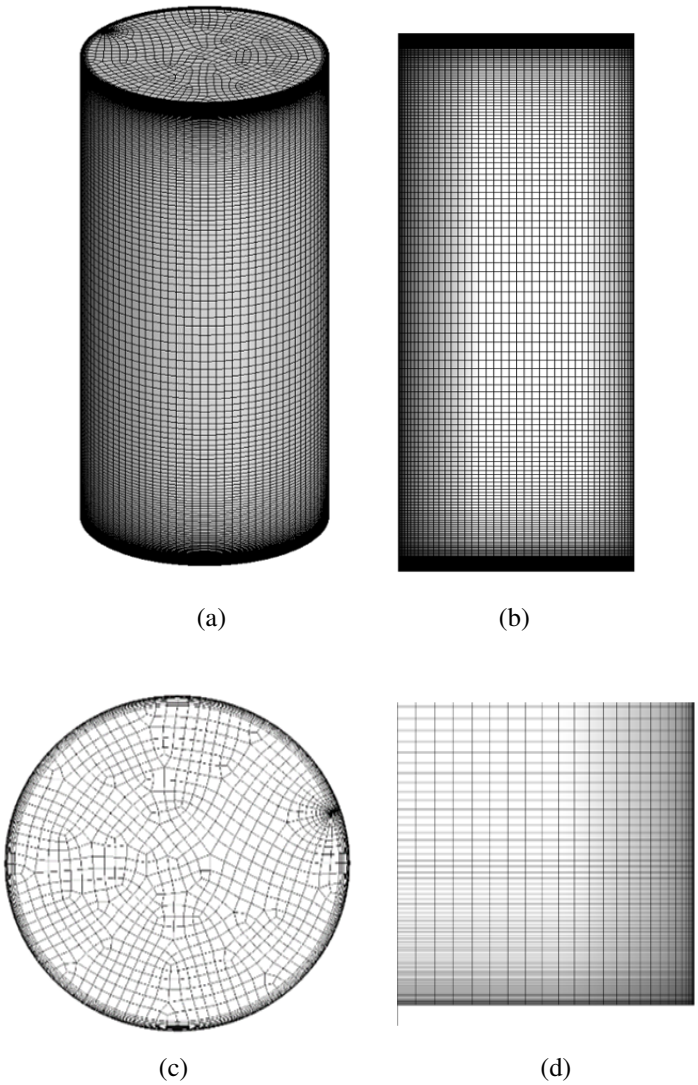

Figure 9: Mesh of developed vertical cylindrical CFD tank model (a) isometric view, (b) side view, (c) top view and (d) enlarged view of the corner region

the movement of fluid is dependent on the nonlinear variation of water properties with temperature, especially the density of water. To simplify the analysis, the Boussinesq approximation model for the density is often recommended for cases in which the temperature gradient within the domain is small, usually of the order of $5°$C (Budihardjo, 2005). In convective cooling of a thermal storage tank, the temperature difference of water inside the tank rarely exceeds $5°$C, even with thermal stratification, hence the

Boussinesq approximation was used in this study. The approximation considers the density of water to be a linear function of temperature only during the computation of body force in the momentum equation as shown in Equation (1).

$$\rho = \rho_o - \beta\rho_o \left(T_f - T'_f\right) \tag{1}$$

To lessen the error of density arising from the Boussinesq approximation, Basu et al. (2013) suggest using the average temperature as the reference in the operation of single-phase natural circulation loops. When using the thermal expansion coefficient of water evaluated at the reference temperature of $34°$C, the average between the initial hot water temperature of $40°$C and the final cooled temperature of $28°$C, the maximum error in density resulting from Boussinesq approximation was shown to be less than 0.03% in comparison to the IAPWS-IF97 (non- Boussinesq) from (Wagner et al., 2008) which indicates the validity of using Boussinesq approximation for the current problem.

Before the CFD model can be solved, it was necessary to determine the flow regime of natural convection that takes place in the cavity. Rayleigh number for transient cooling of tanks subjected to convective boundary condition can be determined, as shown in Equation (2).

$$Ra = \frac{g\beta_f(\bar{T}_f - T_{env})H^3}{\upsilon_f \alpha_f} \tag{2}$$

Rodriguez et al. (2009) reported that the flow regime can be considered as laminar for Rayleigh number below 10^{13} for tanks exposed to convective boundary conditions. Based on the Rayleigh number calculated at the reference temperature of $34°$C, which is less than 10^{12}, it was hypothesized that the flow regime is laminar and modelled as such.

Numerical solutions to flow and heat transfer problems obtained from CFD contain errors arising from discretization of the continuous flow domain. Generally, these

discretization errors can be minimized by meshing the flow domain into a large number of control volumes. However, there is a trade-off between the accuracy of the solution and the computing time as the computational cost increases with increasing number of mesh points. In this study, two mesh distributions on the cross section of the tank model were generated for the purpose of choosing the optimal grid size, as shown in Figure 10. Mesh sensitivity analysis was performed using the Grid Convergence Index (GCI) proposed by Roache (1998) with two different grids having maximum cell sizes of 7.5 mm and 15 mm. It is based on Richardson's extrapolation and assumes that only truncation errors arise from discretization of the computational domain, which tend to disappear when the spatial intervals within the mesh becomes close to zero. The GCI between the fine and coarse mesh is calculated as shown in Equation (3).

$$GCI = \frac{F_s|\epsilon_r|}{{r_m}^{(p_m-1)}} \tag{3}$$

Where, F_s the safety coefficient, p_m is the order of the solver method, r_m is the mesh refinement ratio which is the ratio of maximum cell sizes of coarse mesh over fine mesh and ϵ_r is the relative error between the solutions obtained from different meshes.

Mesh sensitivity analysis was performed using the Grid Convergence Index (GCI) with two different grids having maximum cell sizes of 7.5 mm and 15 mm. The calculated GCI between the coarsest and finest mesh, with a safety coefficient (F_s) of 3, using the average temperature of the tank showed a maximum error of less than 3%. This suggests that a mesh with 15 mm cell size (416,800 elements) was satisfactory.

To ensure the solution was not influenced by the time step size, solver times were submitted to a time step independence analysis, based on the estimation of time constant defined by (Bejan, 2013) as indicated in Equation (4) and (5).

$$\tau = \frac{H^2}{\alpha_f}(RaPr)^{-(1/2)} \tag{4}$$

$$\delta t \approx \frac{\tau}{4} \tag{5}$$

Where, τ is the time constant for natural internal convection (s), H is the height of the enclosure (m), $\alpha$is the thermal diffusivity (m^2/s), Pr the Prandtl number of the fluid at average temperature between the fluid and the ambient, δts the time step size (s).

The calculated time step size based on the estimation of time constant defined by Bejan (2013), δt is 2.82s. Therefore, solution time intervals of, 1.41, 2.82, and 5.64s were compared. Figure 11 shows CFD predictions of horizontal temperature variation at the height of 0.625 m for different time steps after 6 hours since the start of the test. The result show that the time step of 2.82 s is a good compromise between numerical accuracy and computational cost, hence was chosen for this study.

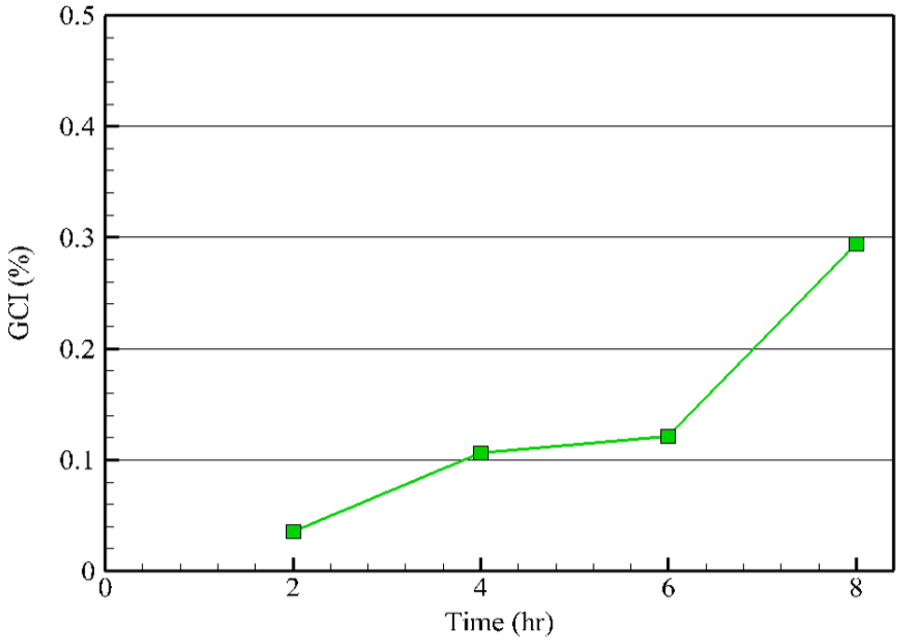

Figure 10: GCI variation of the average temperature of the tank during 6 hr standby period

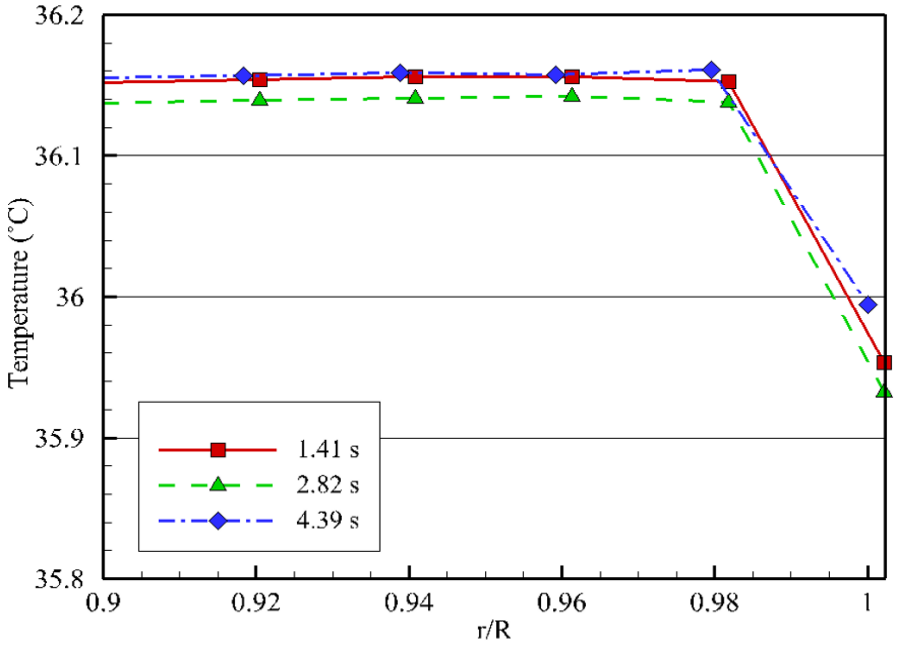

Figure 11: Horizontal temperature variation with solver steps at the height of 0.625 m after 6 hours of cooling

2.3 Experimental validation

To validate the CFD method used, it was necessary to construct a suitable experimental apparatus. To facilitate the measurement of spatially averaged velocity estimates using Particle Image Velocimetry (PIV), it was decided to conduct study on a rectangular storage tank instead of a cylindrical tank since it can provide a better optical access and successfully used in previous studies (Knudsen, 2004, Knudsen et al., 2005). On top of that, changing the shape of a tank from rectangular to cylindrical does not result in significant variations if the wall curvature is large enough (Equation (6)) (see Cengel (2004)). In this study, the ratio on the right-hand side of Equation (6) only accounts for about 15% of the tank diameter. The chosen rectangular storage tank has the dimensions close to the numerical model using CFD, as shown in Table 2.

$$D \geq \frac{35\ H}{(\frac{Ra}{Pr})^{1/4}} \tag{6}$$

To study the flow and thermal processes of water under natural convection, the tank was initially filled with cold water. A charging loop consisting of a pump that draws cold water from the bottom of the tank, heats it through a 3kW electric heater, and feeds it back to the top of the tank was then used to heat the water to the desired uniform temperature of 40°C. This condition could represent a typical fully charged SDHW system on a sunny day after the entire volume of water gets heated. The tank was then allowed to lose heat to the surroundings to imitate the process of standby operation of solar water tanks during which static heat loss to the ambient takes place.

Table 2: Data related to experimental rectangular tank

Dimensions	
Hot water tank volume (m^3)	0.195
Tank height (m)	1.22
Tank width (m)	0.4
Tank length (m)	0.4
Tank wall thickness (m)	0.015
Acrylic thermal properties	
Density (kg/m^3)	1188
Specific heat capacity (J/kgK)	1514
Thermal conductivity (W/mK)	0.173

To determine the temperature profile inside the tank, a series of eight copper-constantan (Type-T) thermocouples that were distributed along the height of the tank was used while a ninth thermocouple was used to measure the ambient temperature. The thermocouples were connected to two Picolog TC-08 data acquisition systems and temperature readings were recorded by a computer via USB interface. The data acquisition system was managed through a Picolog data logging software which has a built-in voltage to temperature conversion with cold junction compensation. The configuration

for experimental temperature measurement system is illustrated schematically in Figure 12.

For the distribution of thermocouples in the tank, the work of Oliveski (2000) was followed. The cylindrical reservoir used in their study satisfies the condition provided by Cengel (2004), which implies that the effect of the surface curvature of the cylinder can be neglected and the cylinder can be regarded as a rectangular tank (see equation (6)). Oliveski (2000) verified that the thermal gradients in the radial direction are almost non-existent except in the boundary layer. On the other hand, Rodriguez et al. (2009) showed that water inside the tank reaches the quasi- steady regime which includes a region of stratified fluid close to the bottom with a steep temperature gradient that occupies at most 25% of the tank volume, a mixed region near the upper part, with at least 25% of the tank volume, and a wide transition zone in the middle section of the tank after a period of cooling.

Based on their work, it was decided to place a single thermocouple in each of the stratified zone at the bottom and mixed region at the top of the tank, and evenly distribute the remaining 6 thermocouples in the middle section of the tank. An additional thermocouple was also used to monitor the surrounding air temperature. All the thermocouples used in the experiment were calibrated against a platinum resistance thermometer (PT-100) and the accuracy of the calibration was shown to be within the standard deviation of ± 1.16°C across the temperature measurement range. Detailed calibration of the thermocouples used for the measurements are discussed in Appendix A1.

The flow visualization was carried out on the experimental tank using a two-dimensional PIV system that is capable of indirectly determining the velocity field of a fluid in a plane by measuring the velocity of seeding particles that are introduced into the flow. A two-dimensional PIV system includes a dual-pulse PIV laser and a CCD camera that are synchronized with the help of a synchronizer.

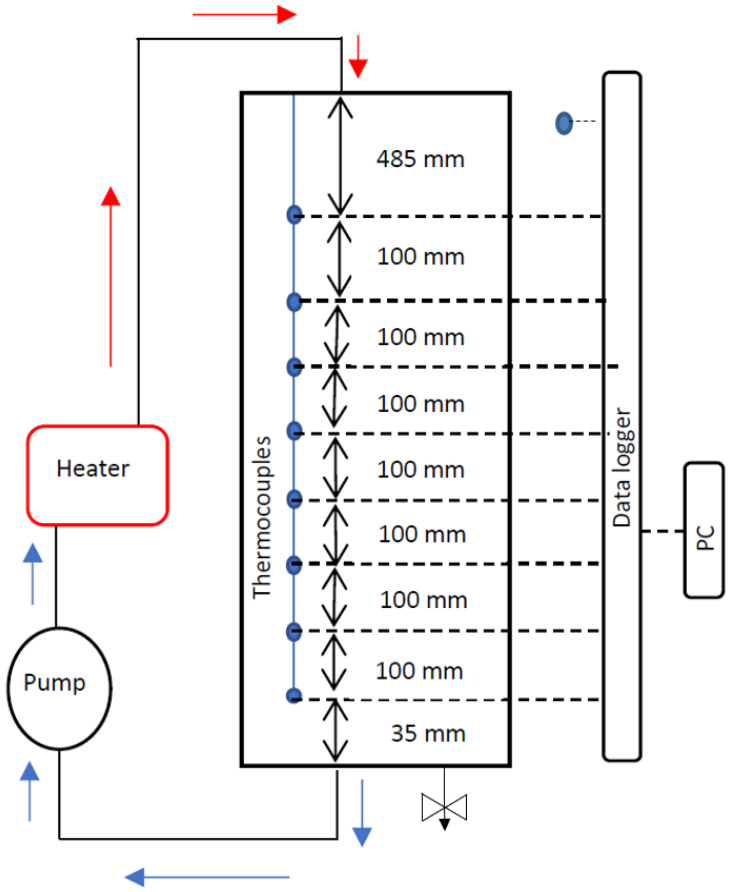

Figure 12: Schematic of experimental temperature measurement system

A digital CCD (Charge coupled device) camera with a frame rate of 16 fps and a resolution of 2456 x 2048 pixels was used to record the flow patterns. The data stored in the CCD is transferred to a frame-grabber using full-frame interline transfer method so that it can be processed in a PC. In this method, each active pixel has its own storage site provided by vertical shift register which allows to store the image temporarily while the second image is being captured. This enables the fast transfer of the captured image data to the adjoining storage sites which is particularly useful for high velocity flow measurements, where single exposure double frame PIV images need to be captured within short inter-frame time intervals.

Given that the PIV technique indirectly determines the fluid velocity by measuring the particle velocity, it is important to carefully choose suitable seeding particles to avoid a significant mismatch between the fluid and particle motion. A primary source of error is caused by gravitational forces generated by the difference in densities between the fluid and the particles. Raffel et al. (1998) showed that gravitationally induced velocity, u_g of spherical particles in a viscous fluid flowing at a very low Reynolds number (i.e. natural convection) can be determined using Stokes' drag law, as shown in Equation (7).

$$u_g = \frac{d_{sp}^2(\rho_{sp} - \rho_f)}{18\mu_f} \tag{7}$$

For the tracer particles, a mixture of 20m and 50m round-shaped polyamide particles with a density of 1030 kg/m^3 (Dantec Dynamics) were chosen. This mixture has gravitationally induced velocity, u_g of approximately 2×10^{-5} m/s which is about two orders of magnitude lower than the typical minimum velocity of natural convection flow inside a tank (Oliveski, 2000, Budihardjo, 2005, Fan and Furbo, 2012a). This suggested that it is unlikely for the measured particle velocity to be significantly different from that of actual fluid velocity.

Since the PIV method estimates the flow of fluid based on the number of seeding particles present per unit area of the measurement plane, it is recommended to have as many particles as possible to increase the accuracy of the PIV results (Raffel et al., 1998). However, having excessive number of particles can also interfere with the visibility of the measurement plane. Therefore, experimental trials were carried out to determine the maximum amount of seeding particles giving good seeding distribution over the measurement window without compromising the its visibility. It was shown that for the 200 L tank, the maximum amount of seeding particles should not exceed 30 g.

To improve the accuracy of velocity measurement by utilizing the available seeding particles in the tank, the measurement window is sub-divided into interrogation windows, typically 16x16, 32x32 or 64x64 pixels. The idea of choosing a smaller interrogation to obtain higher resolution vector map is limited by the number of seeding particles in the area. In this study, it was shown that the smallest interrogation window suitable for measurements with existing particle distribution is shown to be of 32x32 pixels. A way to enhance the resolution of the vector map without having a significant compromise in accuracy is to overlap interrogation windows. Thus, a 50% overlap was used between 32x32 pixel windows (i.e. the distance between the centers of adjoining interrogation areas is 16 pixels in each direction).

This experiment aims to measure the velocity profile of the boundary layer on the sidewall of the tank. This is because detectable natural convection flow due to heat loss has been numerically shown to occur in the form of buoyancy-driven boundary layer flow near the side wall using CFD models (Oliveski, 2000, Fan and Furbo, 2012a). Knowing that a clear high-resolution vector map using the current camera setup can only be obtained for a measurement plane of size (40mm x 70 mm), it is difficult to capture the full extent of boundary layer flow at a given time. Therefore, full tank (400mm x 1220mm) measurement at a given time cannot be performed.

Table 3: Locations of measurement planes with respective recorded time

Measurement plane	**Width, X (mm)**	**Height, H (mm)**	**Elapsed time (min)**
1	0-40	40-110	10
2	0-40	315-385	30
3	0-40	1150-1220	80

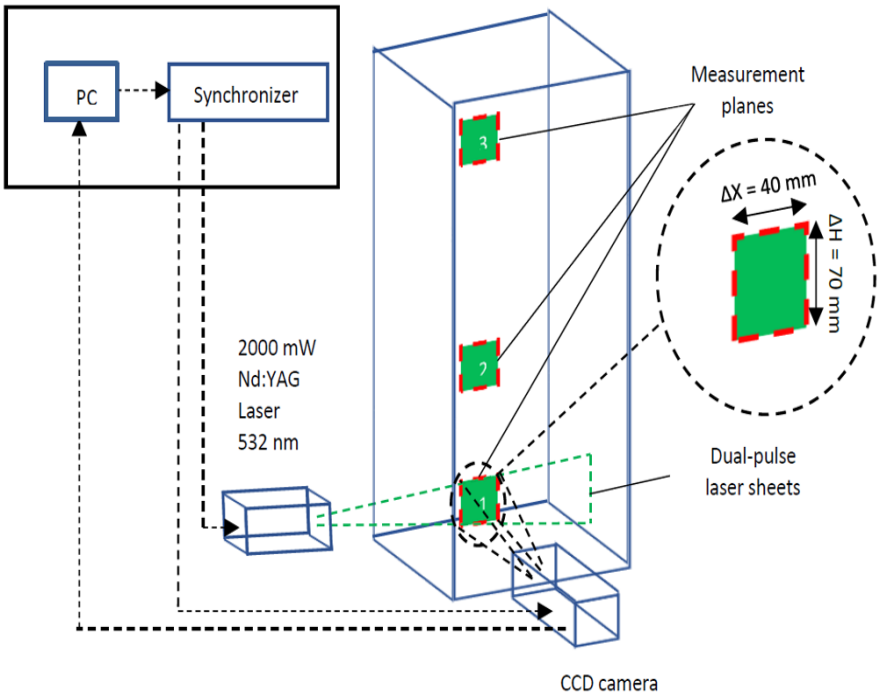

(a)

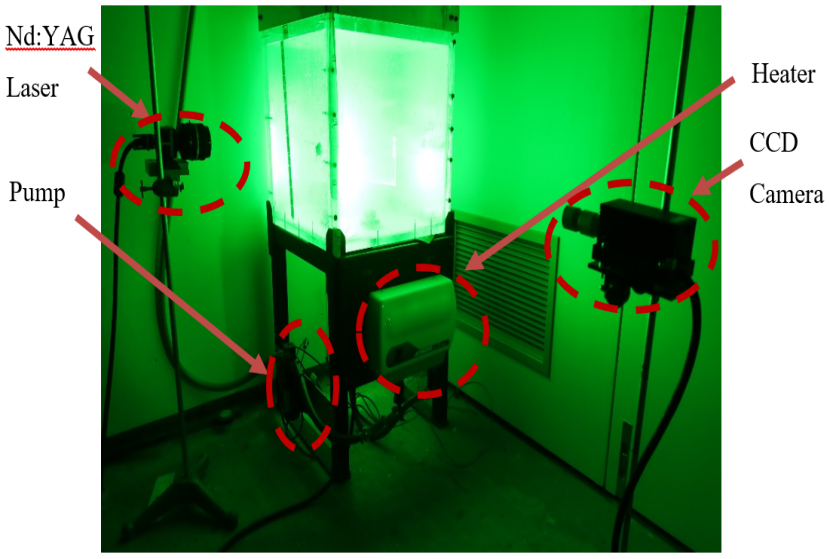

(b)

Figure 13: Experimental velocity measurement system (a) Schematic and (b) Actual

Previous studies showed that natural convection flow takes place in the boundary layer which leads to stratification in the lower section of the tank using CFD models. Along with the progression of cooling time, the region of stratification expands from the bottom to the top of the tank. This suppresses the boundary layer flow, resulting in weak natural convection flow inside the tank except the top section inside which recirculation flow persists, owing to heat loss from the top wall (Lin and Armfield, 1999, Oliveski, 2000, Fan and Furbo, 2012a, Fan and Furbo, 2012b). Given the above, it was decided to examine the flow in three selected planes (see Table 3) that characterizes this flow progression with time. Therefore, the selected frames and time were chosen according the latter mentioned flow behavior. By doing this, it is believed that the flow visualization captures the important features of the flow and would provide results that are strong enough to validate the CFD methodology. The configuration for experimental velocity PIV measurement system is illustrated in Figure 13.

The PIV recording technique used in this study was a double frame/single exposure, as sketched in Figure 14. This technique of recording inherently preserves the information on temporal order of particle images and illumination pulses. Thus, it is superior to the single frame/double exposure technique, which faces the potential issue of losing track of direction to which particles move in the captured single PIV image (Raffel et al., 1998).

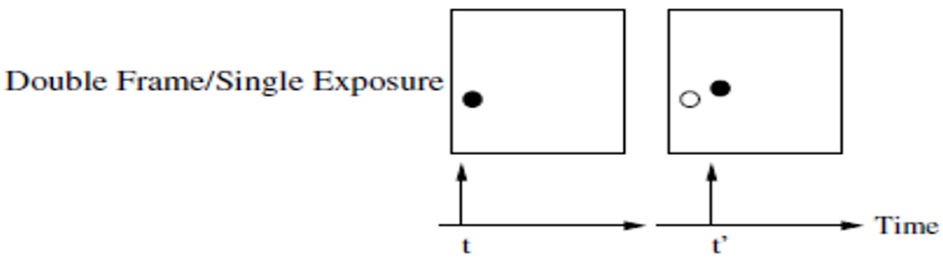

Figure 14: Double frame/Single exposure PIV recording technique (adopted from (Raffel et al., 2018))

The most critical parameter in double frame/single exposure PIV recording is the time interval between two successive images which influences the accuracy of the PIV results. The time interval between image pairs needs to be short enough to avoid particles from completely leaving the interrogation area. Adrian (1997) recommended that this time interval should be adjusted so that the maximum displacement of the seeding particles should be less than one quarter of the interrogation window. To achieve this, the particles inside the tank were illuminated with the laser sheet on a vertical symmetry plane through the middle of the tank while CCD camera is positioned at 600mm, perpendicular to the measurement plane. At this arrangement, the resolution of the images taken is approximately 25 pixels per mm. Based on this, an estimate of the laser pulse delay used in this experiment is 40 ms, as shown in Table 4.

Table 4: PIV parameters used in the study

Parameter	**Value**	**Unit**
Image resolution	0.04	$mm/pixel$
Max velocity (estimate)	8	mm/s
Interrogation window	32x32	$pixels$
Step (Overlap)	50	$\%$
Desired displacement	0.008	m/s
Laser pulse delay	40	ms

A series of image pairs are then processed using a statistical method, called cross correlation to obtain a velocity vector map. A cross-correlation technique compares the light intensity distribution between two images to determine the displacement, as indicated by peak intensity. The outcome of cross correlating between two images produces a correlation peak that represents the average displacement of the particles in each interrogation window. For a detailed mathematical derivation of cross-correlation, one can refer to (Raffel et al., 1998). A detailed analysis of errors related to PIV measurements are discussed in Appendix A2.

2.4 Results and Discussion

2.4.1 Validation of developed CFD model

Given that experimental setup used for validation was for rectangular tank, it was necessary to develop a CFD model with the same configuration and boundary conditions. Mesh and time sensitivity analysis related to the developed CFD model is provided in Appendix B1.

For ease of comparison with experimental data, the tank model was segmented into eight sections. To specify external heat loss coefficients corresponding to the experiment, measured rate of change of water temperature in each section was fitted based on Newton's law of cooling, as suggested by Mawire and Taole (2013). External convective heat loss coefficient for each section was then calculated by varying its value until the computed overall heat transfer coefficients (U_j) matches the measured values. This calculation assumes that computed internal convection heat transfer coefficients are the same as those in the experiment over the sampling period of 24 hours. The obtained external heat transfer coefficients along with measured ambient temperatures were specified by means of User Defined Function. Detailed calculations of external heat loss coefficients are provided in Appendix B2.

Figure 15 shows the measured, and CFD predicted, temperatures in the tank over a 24-hour period. The temperatures show that after 10 minutes there has been a gradual decrease in temperature from 40°C to 39.2°C at the bottom of the tank. As the tank continues to cool down, the water temperature at the bottom decreases at a faster rate than the top. The maximum temperature difference between the top and bottom of the tank reaches 4°C, 24 h after the start of the experiment. This is because of the progressive development of thermal stratification at the bottom formed by the downward flow of cold water along the tank wall. More details of this process will be discussed

when viewing the viewing the velocity contour plots later.

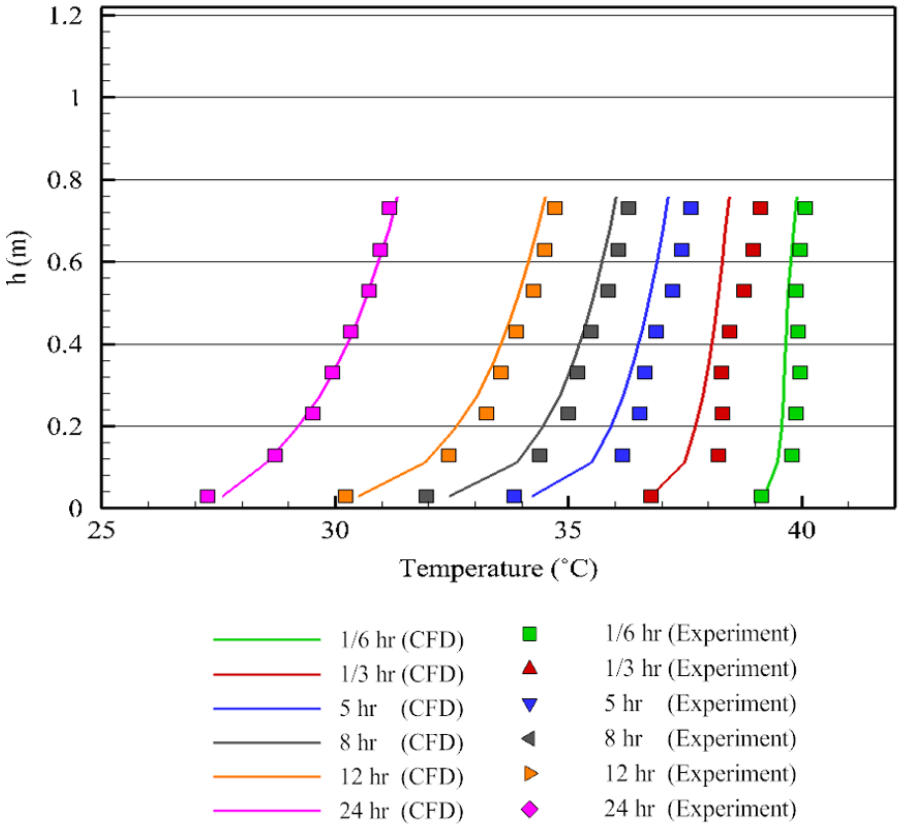

Figure 15: Temperature validation of CFD model for cool-down test

From these results, it is apparent that the temperature profile predicted by the CFD model is like that of the experiment. The same temperature trend has been observed between the two data sets (experiment and CFD) after 1/3 h (80 min) to 12 h of cooling, with deviations between the CFD prediction and the experimental data becoming negligible 24 h after the start of the cool-down test. The minor differences are likely due to the thermal stratification of the surrounding air during the experiment as a result of heat loss from the tank. Owing to heat loss from the tank, temperature of the ambient air near the top of the tank is higher compared to that close to the bottom of the tank, leading to the lower heat loss from the top section of the tank. This possible variation of ambient temperature with height of the tank is not considered in the CFD model since the average ambient temperature has been specified at every section of the tank. Similar

behavior was observed by Fan and Furbo (2012a).

The velocity field predicted from the numerical model was also validated with experimental PIV results obtained at the location of three measurement planes. Comparisons between the numerical and experimental data is limited to the near wall region inside which the boundary layer takes place. Figure 16 shows the time-averaged velocity contours at plane 3 for both the PIV and CFD between 80-82 min of the cooling test. From this the CFD model prediction compares reasonably well with the PIV data, displaying initial formation of the hydrodynamic boundary layer near the wall due to heat losses from both top and side tank walls. A comparison of the PIV and CFD boundary layer velocity magnitude at a height of 1.18 m is shown in Figure 16 (c). From these results it is apparent that the velocity in the experiment were slightly larger than those predicted by the CFD model. The maximum velocity inside the boundary layer peaks at approximately 2.2 mm/s for the CFD, whereas the PIV peaks at 2.4 mm/s. This may be due to higher buoyancy forces in the experiment with respect to the CFD model as a result of higher tank temperature at the top, as indicated in Figure 15. However, in general there is good agreement between the two results.

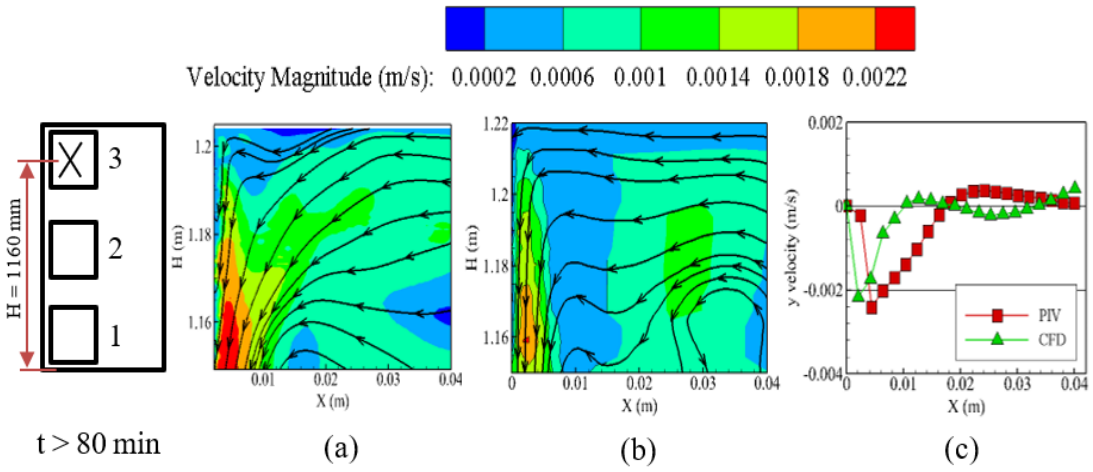

Figure 16: (a) Velocity field from experiment (left), and (b) CFD model (middle) at measurement plane 3 after 80 min of cooling, (c) Velocity magnitude in the boundary layer versus the distance from the wall at H = 1160 mm

Exploring the flow further, time-averaged flow patterns for plane 2 between 30-32 min of the cooling test are presented in Figure 17. Again, the CFD model agrees qualitatively well with the experimental results in terms of the velocity fields. In these, it is apparent that there is a downward flow of cold water in the boundary layer and an upward flow of hot water far from the sidewall. The flow velocities in the boundary layer at 360 mm are plotted in Figure 17(c) and again lower velocity values are estimated by CFD model, the highest velocity of 2.4 mm/s is seen in the numerical model, whereas PIV results showed the maximum velocity of 3 mm/s though they still correspond well with the experimental results. Again, this may be due to lower buoyancy forces in the CFD model because of the lower temperature at the tank top compared to the experiment.

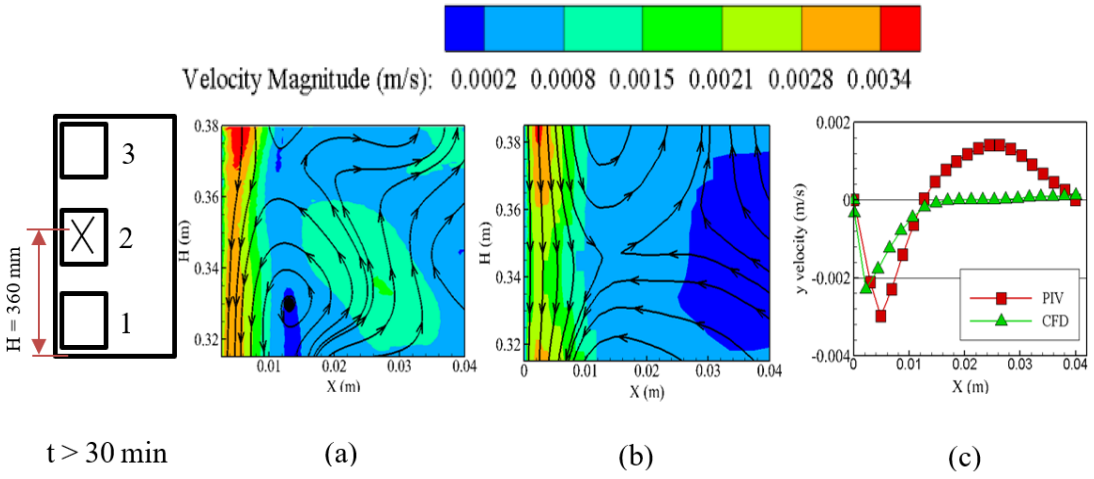

Figure 17: (a) Velocity field from experiment (left), and (b) CFD model (middle) at measurement plane 2 after 30 min of cooling, (c) Velocity magnitude in the boundary layer versus the distance from the wall at H = 360 mm

Finally, the velocity contours for plane 1 between 10-12 min of the cooling test are shown in Figure 18. Good validation of the numerical model is observed, displaying the detachment of boundary layer into the center at the bottom of the tank. The plot of velocities across the boundary layer at 80 mm indicate a velocity of approximately 2.1 mm/s in the PIV results, while the CFD model showed an estimate of 3 mm/s. This

might be due to low level of thermal stratification in CFD model as a result of higher tank temperature at the bottom predicted by CFD model as oppose to the experiment.

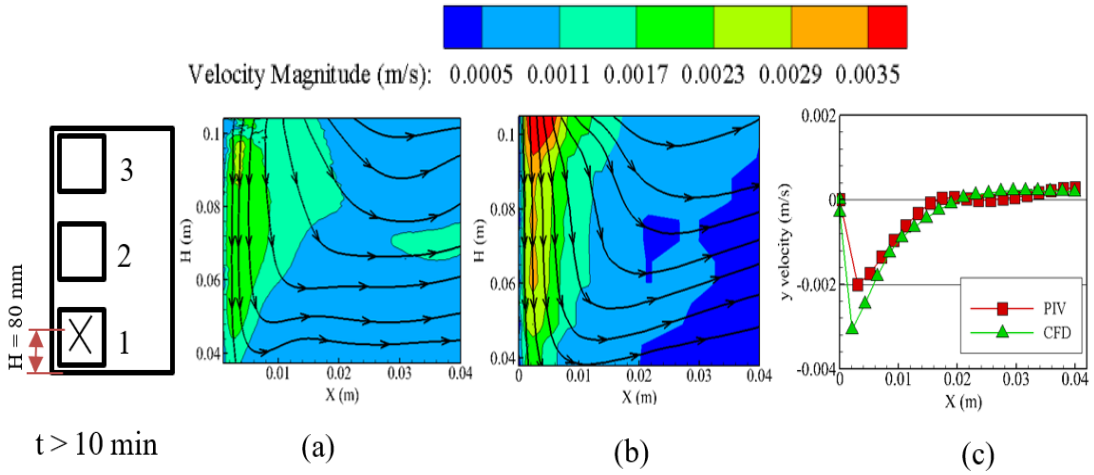

Figure 18: (a) Velocity field from experiment, and (b) CFD model at measurement plane 1 after 10 min of cooling, (c) Velocity magnitudes in the boundary layer versus the distance from the wall at H = 80 mm

2.4.2 Natural convection heat transfer inside a vertical cylindrical tank

Having validated the computational methodology using the rectangular storage tank, it was decided to examine flow and heat transfer inside a more commonly used vertical cylindrical storage tank to provide understanding of how natural convection flow induced by heat loss is developed inside the tank.

In Figure 19, it can be seen from the velocity contours that the flow with high velocity magnitudes takes place along the cooled side (right) wall of the tank. During the early stages of cooling, the thermal boundary layer develops rapidly on the side wall since the cooled water near the wall descends towards the bottom wall due to its density getting higher than the initially stored hot water. When it reaches the bottom of the tank, it advances towards the center of the tank and mixes with the surrounding

hot water at the bottom of the tank. This process continues for just a few instants until thermal stratification of water is formed inside the tank. At this point, secondary convective cells relatively low velocities are continuously formed underneath the top wall and transported to the core of the tank. The formation of theses convective cells was observed in the numerical work of Oliveski (2000) and can be linked to heat loss from the top wall which cools the water beneath the top wall and forces it to sink to a region of the same temperature. This necessitates the same amount of hot water to ascend and take its place to satisfy the conservation of mass.

As the cooling proceeds, the overall intensity of the flow gradually decreases due to the progressive lessening of temperature difference between the hot water and the ambient. In addition, hot water becomes thermally stratified with low temperature zones, filling up the tank from the bottom to the top, which consequently leads to the shortening of the vertical length of thermal boundary layer as the descending cooled water is forced to mix with thermally stratified region of the same temperature instead of travelling further towards the bottom of the tank, as shown in Figure 20.

Figure 21 shows the variation of average convective heat transfer coefficient inside the tank with cooling time. With respect to the flow behavior described above, convective heat transfer coefficient increases from 1 to 10 min of cooling due to the initial development of boundary layer on the side wall. As the tank cools from 10 min to 6 hours, convective heat transfer coefficient gradually decreases owing to increasing degree of thermal stratification and progressive lessening of temperature difference between the hot water and the ambient.

It is evident that convective heat transfer coefficient is highly dependent on cooling time since the initial condition of the tank (i.e. uniform temperature of water). This highlights the challenge in tracking the time elapsed from initially unstratified state of tank to determine the convective heat transfer coefficient inside the tank.

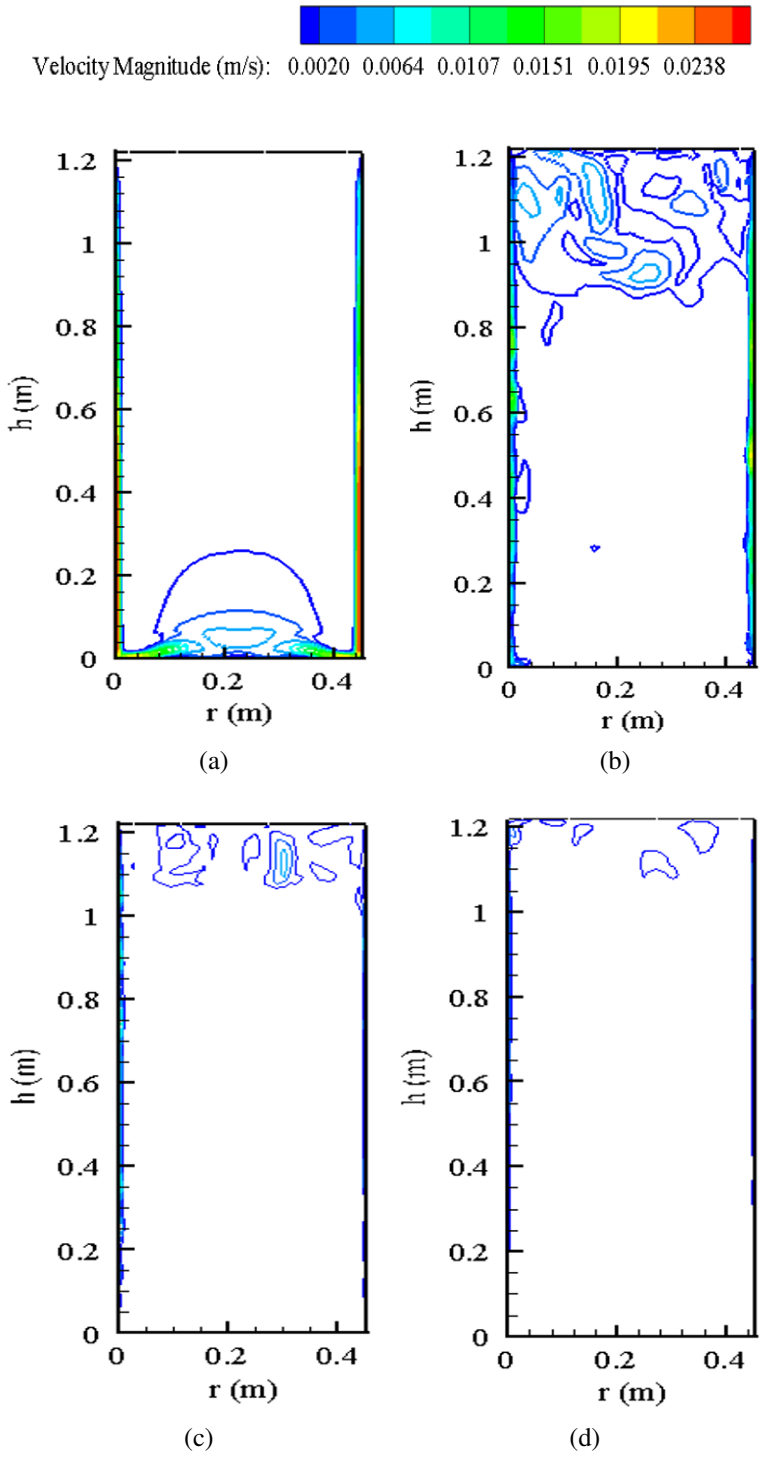

Figure 19: Transient evolution of the flow of the fluid inside the storage tank after (a) 1 min of cooling, (b) 10 min of cooling, (c) 1 hour of cooling, (d) 6 hours of cooling

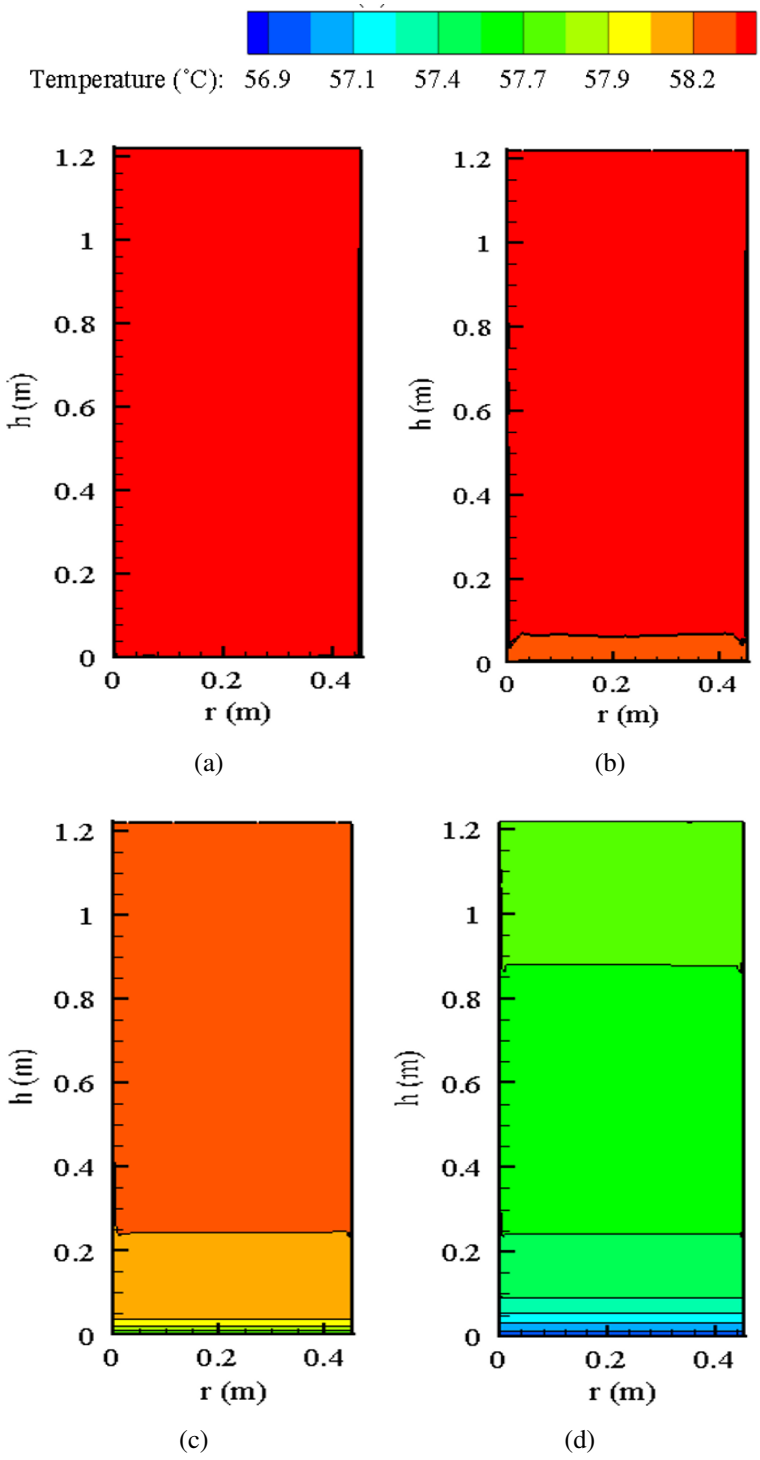

Figure 20: Transient evolution of the temperature of the fluid inside the storage tank after (a) 1 min of cooling, (b) 10 min of cooling, (c) 1 hour of cooling, (d) 6 hours of cooling

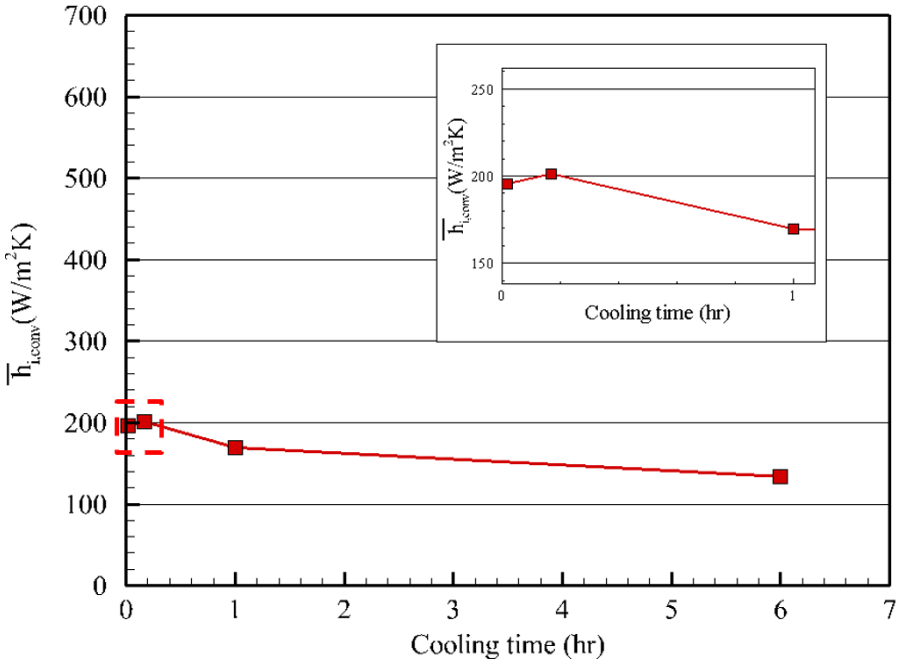

Figure 21: Variation of average convective heat transfer coefficient with cooling time

Knowing that the water inside solar storage tanks can be in a stratified state depending on charging and discharging process throughout the day, this indicates the need to develop heat transfer correlation that can predict convection heat transfer coefficient independent of both the initial condition and cooling time.

2.5 Conclusions

This purpose of this chapter was to examine the development of natural convection flow inside a vertical cylindrical storage tank due to static heat loss. To validate the CFD methodology, measurements of boundary layer velocity and temperature profile inside a laboratory-scale experimental rectangular tank were used as a benchmark validation data. The corresponding CFD model predicted results that are in good agreement with experimental measurements.

Having validated the computational methodology using the rectangular storage tank, natural convection flow and heat transfer inside a more commonly used vertical cylindrical storage tank due to static heat loss was examined. It was shown that during the early stage, thermal boundary layer develops on the side wall and falls towards the bottom of the tank which leads to formation of thermal stratification near the bottom. As time proceeds, the region of stratification expands which weakens the thermal boundary layer flow and as a result, only secondary recirculation cells are present close to the top section of the tank. The observed flow behavior agrees well with findings from previous studies.

It was also shown that internal convective heat transfer coefficient also varies with cooling time. This is because natural convection flow behavior inside the tank evolves with cooling time. This understanding serves as a preliminary step towards finding means to predict the rate of natural convection heat transfer due to static heat loss, which will be explored in Chapter 3.

Chapter 3

Numerical study of steady state natural convection

3.1 Introduction

In Chapter II, it was shown that the convective heat transfer coefficient inside a tank (see Figure 22) is dependent on cooling time.

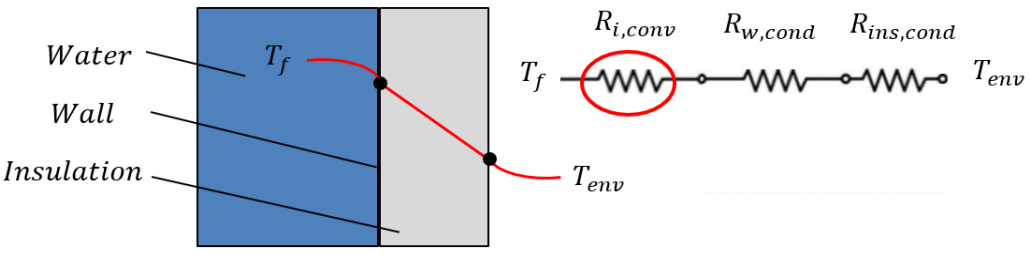

Figure 22: Thermal resistance network for static heat loss to the ambient

Given the importance of being able to predict the convective heat transfer coefficient in optimizing the performance of a storage tank, Oliveski et al. (2003) conducted a study on transient cooling of hot isothermal water in a cylindrical tank exposed to natural convective cooling. The influence of tank volume, aspect ratio and overall heat loss

coefficient on convective heat transfer coefficient were investigated. In the formulation of overall heat loss coefficient, both conduction resistances of the insulation and tank wall were considered. Based on the results, average Nusselt number correlations were proposed, as shown in Equation (8) and (9).

$$\bar{Nu}_{(V=100L)} = (9.40739U^{*0.288329})\ (1000(\bar{T}_f - T_{env})^{-1} - 20)^{0.00988842U^{*}-0.189428}(\frac{H}{D})^{0.3} \tag{8}$$

$$\bar{Nu}_{(V=200L)} = (10.6039U^{*0.310719})\ (1000(\bar{T}_f - T_{env})^{-1} - 20)^{0.013052U^{*}-0.224677}(\frac{H}{D})^{0.3} \tag{9}$$

Where U^* is the overall heat transfer coefficient defined by Equation (10) and the characteristic length is defined to be the ratio of tank volume over total surface area.

$$U^* = \frac{1}{R_{ins,cond} + R_{e,conv}} \tag{10}$$

Rodriguez et al. (2009) later pointed out that the Nusselt number correlation provided by Oliveski et al. (2003) had dimensional parameters associated with it, making it difficult to extrapolate their results to scenarios other than those in their work. They provided an equation that presents the variation of average convection heat transfer coefficient in the tank with relevant non-dimensional parameters including dimensionless time and heat loss coefficient, Rayleigh number and aspect ratio (see Equation (11)).

$$\bar{Nu} = 4.5851\ \tau^{-0.1686}\ Ra^{0.0686}\ (\frac{H}{D})^{0.5304}\ \hat{U}^{0.1981} \tag{11}$$

Where, τ is the dimensionless time related to the time elapsed since the tank was

fully charged and the characteristic length is defined as the total height of the tank.

A shortcoming of these equations is that they are either dependent on parameters such as material and thickness of insulation or time elapsed since the tank was fully charged (i.e. the entire tank was filled with hot water at uniform temperature). However, the water inside solar storage tanks is in a stratified state over a considerable period of time throughout the day due to heat loss and alternate charging and discharging operations (Jaluria and Gupta, 1982, Al-Najem, 1993). Therefore, it is desirable to have heat loss equations that can predict heat loss independent of both the initial condition and cooling time.

The closest study to this problem was conducted by Lin and Akins (1986) who numerically studied steady state heat gain inside a vertical cylindrical enclosure. The steady state condition was achieved by first specifying an instantaneous step change in wall temperature, which results in heating of the fluid from an initial uniform temperature. This temperature difference between the fluid and wall was then maintained by increasing the wall temperature continuously until a pseudo-steady state is reached, at which time the relative temperature of any two points in the fluid is independent of time. Based on the results, the authors proposed an equation that related the internal convective heat transfer coefficient to Rayleigh number and aspect ratio. However, the proposed equation is only valid for Rayleigh numbers less than 10^7, whereas solar storage tanks typically have Rayleigh numbers three orders of magnitude higher than this.

Given that there is a need to determine natural convection heat transfer coefficient independent of cooling time and initial temperature profile, the aim of this chapter is to investigate steady state heat loss from vertical cylindrical storage tanks.

3.2 Numerical method

To overcome the abovementioned shortcomings, a three-dimensional CFD model was developed using ANSYS Fluent 19.4. The computational domain consists solely of a fluid (water) domain, while the tank walls (solid) domains were modelled using the thin wall approach. The whole flow domain was paved with a coarse mesh with a maximum grid size of 15 mm except the regions close to the tank wall where concentrated grid points were created by inflating the grid with 10 layers having a first-layer thickness of 0.05 mm and a growth rate of 1.2. The storage tank model boundary conditions are shown in Figure 23, and the no-slip condition boundary condition was applied on all walls.

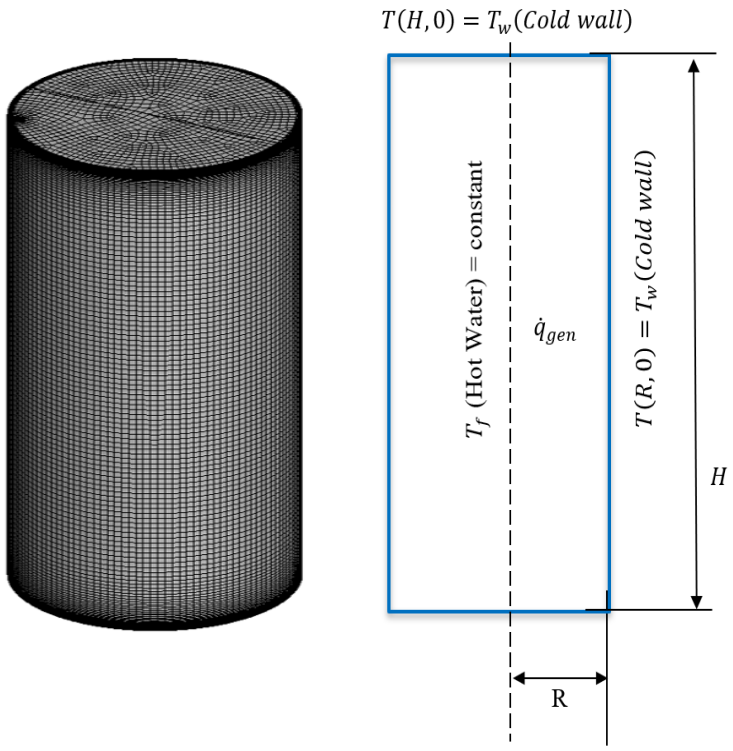

Figure 23: Developed vertical cylindrical CFD tank model (a) mesh and (b) boundary conditions

To estimate the natural convective heat transfer coefficient independent of time, it was necessary to maintain a constant average hot water temperature, and this was achieved by imposing a uniform volumetric heat generation source inside the tank. To achieve this, an energy source term was included in the energy equation to model the uniform volumetric generation of heat, $\dot{q}_{gen}$, which is active in the entirety of the tank. The rate of volumetric heat generation was not constant and varied for different tank geometries examined in this study to ensure that the average hot water temperature (T_f) is held at a constant temperature of $60°$C while the outer walls were specified to be isothermal at a lower temperature (T_w) of $59°$C.

This boundary condition corresponds to the case of a tank at rest at any given time inside which the fluid is weakly stratified while subjected to standing heat loss. This represents a relevant practical situation in which the tank has lost a certain amount heat from its fully charged state. The average hot water temperature was chosen to be at $60°$C since it falls within the operating conditions of solar water storage tanks while the chosen wall temperature of $59°$C resembles physical situation as the tank wall temperature is almost always close to the water temperature in the range of 1 – $3°$C irrespective of the presence of insulation. The selected boundary condition allowed us to examine the relation between tank geometry and natural convection independent of simulation time and insulation-related parameters.The aspect ratio and storage volume of the tank models were taken to be between 1 < AR < 3 and 100L < V < 400L respectively. This is typical of the range of storage tank sizes used in solar domestic hot water systems, as reported by Rodriguez et al. (2009).

Before the CFD model could be solved, it was necessary to determine the flow regime of the natural convection that takes place in the cavity. The Rayleigh number for a storage tank with internal heat generation source, $Ra_{i,gen}$ can be defined as in Equation (12) (see Dinh and Nourgaliev (1997)).

$$Ra_{i,gen} = \frac{g\beta_f\left(\frac{\dot{q}_{gen}H^2\rho_f c_{p,f}\alpha_f}{k_f}\right)H^3}{\upsilon_f\alpha_f} \tag{12}$$

In this vein, Steinberner and Reineke (1978) conducted a combined experimental and numerical study on natural convection in a rectangular cavity with internal heat generation and isothermal cooling on every wall. They concluded that turbulence modelling is necessary for Rayleigh numbers, $Ra_{i,gen}$ between 5 × 10^{12} and 3 × 10^{13}.

Rayleigh numbers based on temperature difference between hot fluid and isothermal cold wall investigated in the current study result in Ra between 10^{11} and 10^{12}. Referring to Oliveski et al. (2003) and Rodriguez et al. (2009), convection heat transfer losses from the water to the wall are in the magnitude of $10^2\ W/m^2K$. Taken this into consideration, the rate of volumetric heat generation required to keep the average temperature of water at $60°$C for the considered cases will result in Rayleigh number between 10^{13} and 10^{14}, which shows that turbulence modelling is necessary.

Regarding the treatment of turbulence inside volumetrically heated liquid pools, Dinh and Nourgaliev (1997) showed that low Reynolds number k – epsilon models can provide reasonable estimates when comparing to experimental data of Steinberner and Reineke (1978). Therefore, the two-equation low-Re turbulent model proposed by Lam and Bremhorst (1981) was chosen in this study.

The maximum error in density resulting from the Boussinesq approximation was shown to be less than 0.01% at a reference temperature of $59.5°$C, the average of the hot water temperature of $60°$C and the outer wall temperature of $59°$C. This indicates the validity of using Buossinesq approximation for the current problem.

A mesh sensitivity analysis was performed using the Grid Convergence Index (GCI) proposed by Roache (1998) with two different grids having maximum cell sizes of 15 mm and 7.5 mm. Since the order of the solver method (p_m) and the mesh refinement ratio (r_m)re equal to 2 in this study, the GCI with a safety coefficient (F_s) 3 directly

reflects the relative error of the solutions obtained from the two meshes. The difference in GCI observed, based on the temperature of the storage tank with 216 L, was only 0.013% between the grid sizes, indicating that a mesh with 15 mm cell size was adequate.

3.3 Results and Discussion

Given that the boundary conditions changed from to the previously validated condition of transient cooling in Chapter 2, it is good practice to revalidate the CFD methodology in light of the changes in the boundary conditions. For this purpose, experimental data obtained from the study of Steinberner and Reineke (1978), who investigated steady state cooling of rectangular tank, was used to validate results from the computational simulations, as indicated in Table 5. A mesh sensitivity analysis of the CFD model is provided in Appendix C.

Table 5: Considered parameters for storage tank models

H (m)	**AR**	**Volume** (L)	$\dot{q}_{gen}$ (W/m^3)	$Ra_{i,gen}$
0.5	1	125	2000	6.28 x 10^{12}
0.52	1	140	2000	7.64 x 10^{12}
0.55	1	157	2000	1.01 x 10^{13}
0.6	1	216	2000	1.56 x 10^{13}
0.63	1	250	2000	1.99 x 10^{13}
0.8	1	512	2000	6.58 x 10^{13}

From Figure 24, it can be seen that the simulated CFD results agree well with the published data of Steinberner and Reineke (1978), with the maximum difference being the Nusselt number on the top wall. Despite this, it is apparent that the model replicates the experimental results quite well. The validation results were considered to be acceptable if the agreement between the experimental data and CFD data or empirical

correlations is less than 15%.

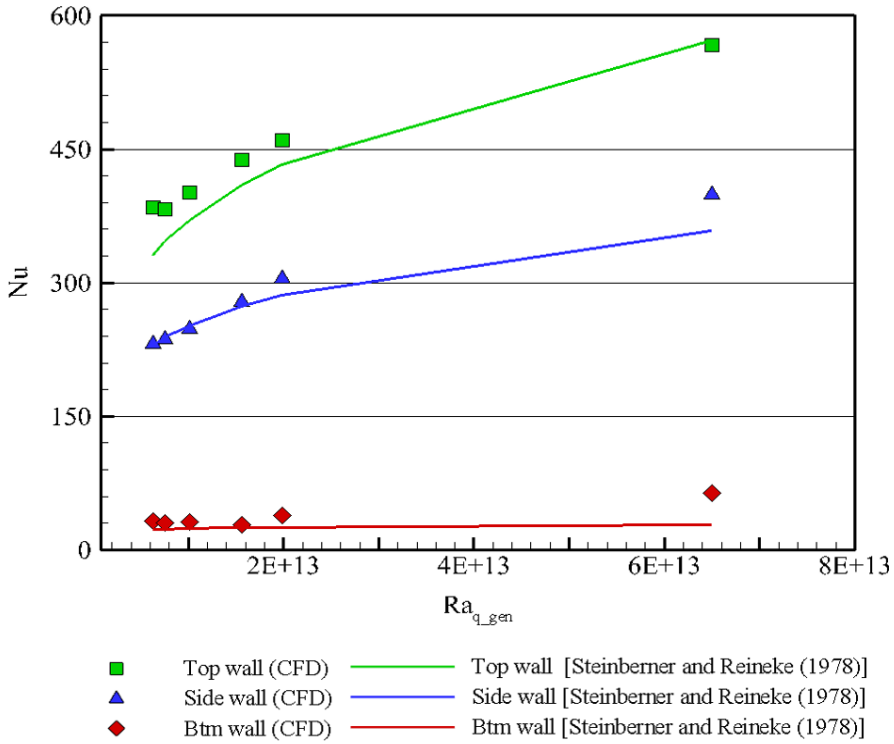

Figure 24: Validation of CFD model with published Nusselt correlations on top, side, and bottom walls

Having validated the methodology, with the revised boundary and heating conditions, it was decided to investigate the convective heater transfer coefficient inside commonly used vertical cylindrical storage tank geometries subjected to steady state heat loss.

Hence, the volume of the tank models were varied in order to change the Rayleigh number with internal heat generation. For this study, the range of tank volumes equated to Rayleigh numbers in the range of 10^{12} to 10^{14}, where the characteristic length was taken to be the ratio of volume divided by the surface area, and the physical properties of the water were calculated at the mean temperature between the water and the wall.

In Figure 25, it can be seen that the Nusselt number decreases with increasing Rayleigh number, for a tank with a fixed aspect ratio. This is typical of natural convection heat transfer, as buoyancy forces becomes stronger at high Rayleigh numbers,

resulting in a higher degree of turbulence and heat transfer.

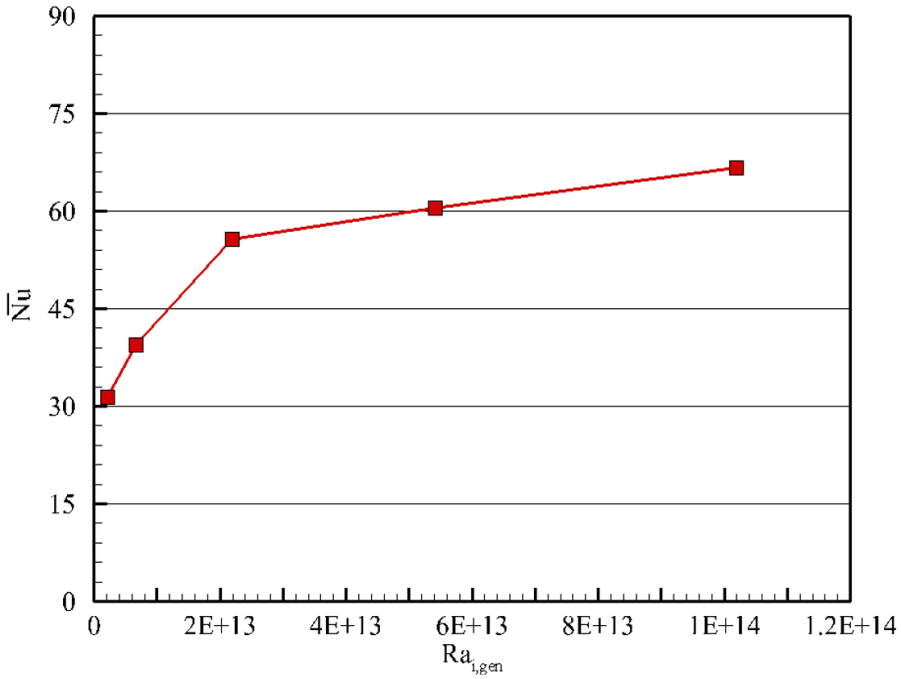

Figure 25: Changes in Nusselt number with Rayleigh number for a fixed aspect ratio (AR = 1)

In Figure 25, it was shown that for a tank with a fixed aspect ratio, Nusselt number was a function of Rayleigh number. That said, Figure 26 shows the velocity contours at the center plane of tanks with a fixed volume (V=402L) and different aspect ratios. In a tank with an aspect ratio of unity, there is significant natural convection flow throughout the entire tank, however increasing the aspect ratio, the natural convection flow appears to be restricted to the top section and near the side wall of the tank. From this, it is likely that convection heat transfer from the tank would be reduced as the aspect ratio increases.

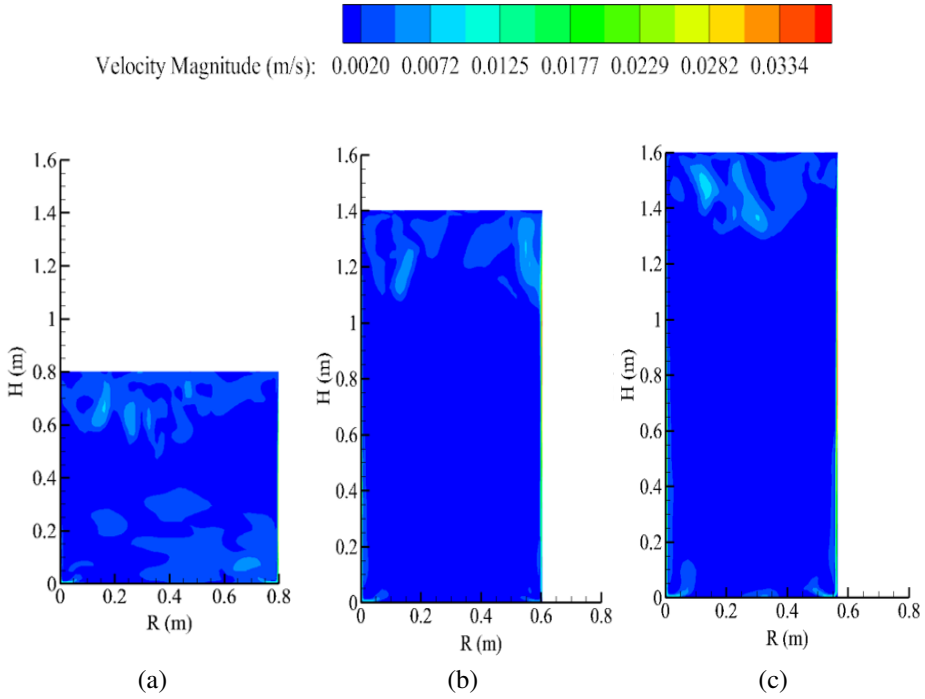

Figure 26: Velocity contours at the center plane of tanks with the volume of 402 L having different aspect ratios of (a) AR = 1, (b) AR = 2.3 and (c) AR = 2.8

Supporting this assertion, Figure 27 shows that the average Nusselt number decreases from aspect ratio of 1 to 2.8 for all tank models irrespective of their volume. To explain the reasons for this, the heat transfer coefficient on each wall of a tank with a volume of 402 L is shown in Figure 28.

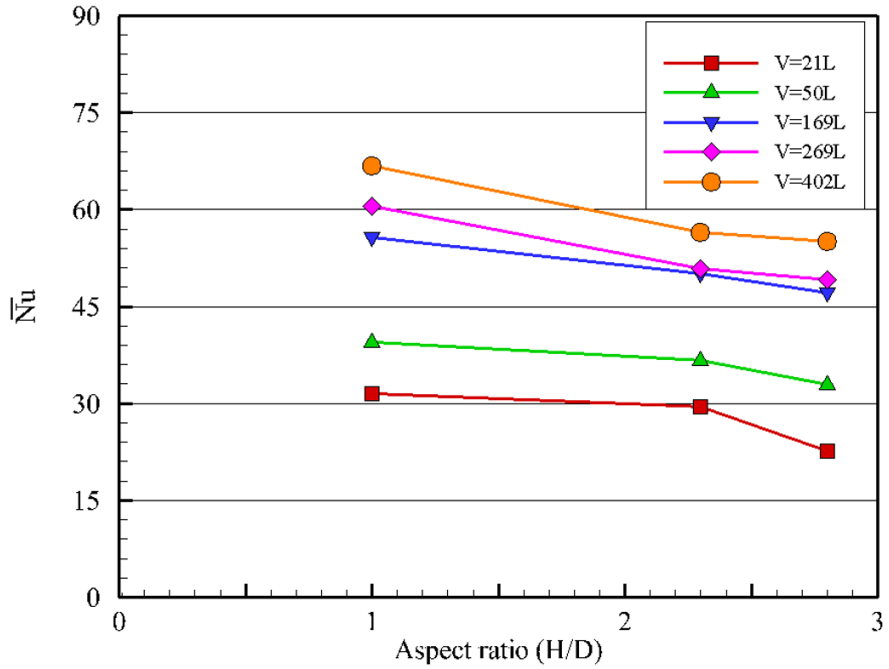

Figure 27: Average Nusselt number with aspect ratios for different tank volumes

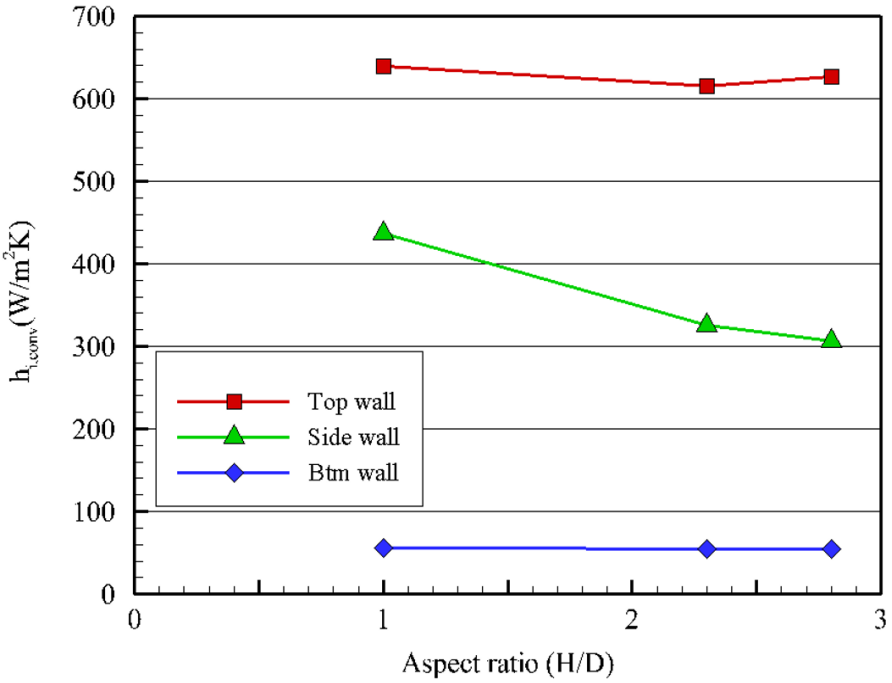

Figure 28: Convective heat transfer coefficient on top, side and bottom tank walls of different aspect ratios with a fixed volume of 402 L

It can be seen from Figure 28 that the average convective heat transfer coefficient inside tanks, with different aspect ratios, is particularly influenced by convective heat transfer on the side wall, which decreases as the tank aspect ratio increases (whereas the top and bottom surfaces remain relatively constant). This can be attributed to the increase in the degree of stratification with increasing aspect ratio, as evident from rise in maximum temperature difference within the tank in Figure 29. The increase restricts the downward flow velocity of the side wall boundary layer, which makes convection heat transfer on the side wall less efficient. This flow behavior can be seen in the velocity contours in Figure 26 and mirrors the findings of Fan and Furbo (2012a, 2012b).

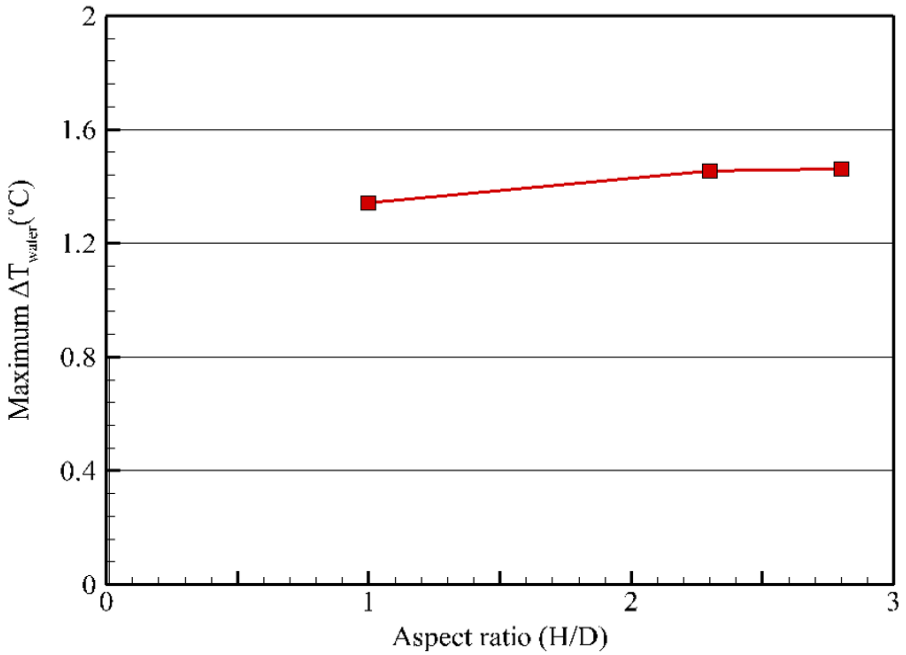

Figure 29: Maximum temperature difference of water inside the tank reflecting the degree of thermal stratification for 402 L tank with different aspect ratios

3.4 Development of a correlation for the convective heat transfer coefficient inside hot water tanks

In the previous section, the effect of varying tank volumes and aspect ratio on convective heat transfers was discussed. Knowing that the internal convective heat transfer coefficient is needed in order to predict heat loss from a tank, an equation that quantifies the convective heat transfer coefficient as a function of a wider range of geometric parameters would make a significant contribution to our ability to design storage water heaters.

From the modelling it was apparent that convective heat transfer, represented by the Nusselt number, was a function of not only Rayleigh number, but also the aspect ratio. Where the characteristic length in both these is defined in Equation (13).

$$L_c = \frac{V}{A_{total}} \tag{13}$$

This characteristic length was chosen because studying different volumes of tanks with fixed aspect ratios results in variation of their volumes and surface areas while investigating various aspect ratios with fixed tank volumes leads to variation of their surface areas. This characteristic length takes changes of both volume and surface area into account. Rayleigh number and aspect ratio are included in the correlation to account for changes in the geometry of the tank.

Hence, the results of convective heat transfer coefficients obtained from the simulations can be correlated, as shown in Equation (14).

$$\bar{Nu} = c\ Ra^m\ AR^n \tag{14}$$

Where, c, n and m are correlation coefficients.

The Rayleigh number for natural convection inside the tank, Ra_T was defined based on the difference between the average temperature of water and the tank wall, as indicated in Equation (15).

$$Ra_T = \frac{g\beta_f(\bar{T}_f - \bar{T}_w){L_c}^3}{\upsilon_f \alpha_f} \tag{15}$$

Based on the results, the fitted coefficients were shown to be c = 0.312, m = 0.285 and n = -0.042 The proposed Nusselt correlation is shown in Equation (16). Different coefficients of c, n and m may be needed for enclosures exceeding the limit of 1.52 x $10^4 < Ra_T <$ 8.97 × 10^6 and 1.7 < AR < 5.8.

$$\bar{Nu} = 0.312\ {Ra_T}^{0.285}\ AR^{-0.042} \tag{16}$$

The goodness of fit for the proposed correlation is illustrated in Figure 30. As can be seen, the proposed Nusselt correlation shows a good agreement with all the simulated data set, with a goodness of fit of $R^2 = 0.981$.

3.5 Utilization of developed correlation to predict rate of heat loss

The developed correlation can be used to predict the natural convection heat transfer coefficient inside any stratified tank within its range of validity, and subsequently the rate of heat loss to the ambient. To demonstrate its capability, the experimental study of Murthy et al. (1992) was adopted (see Table 6).

A one-dimensional storage tank model was developed in MATLAB, inside which the proposed correlation was implemented. To facilitate the stratification, it was assumed that the tank could be modelled with 5 nodes (n=5). Detailed energy balance related

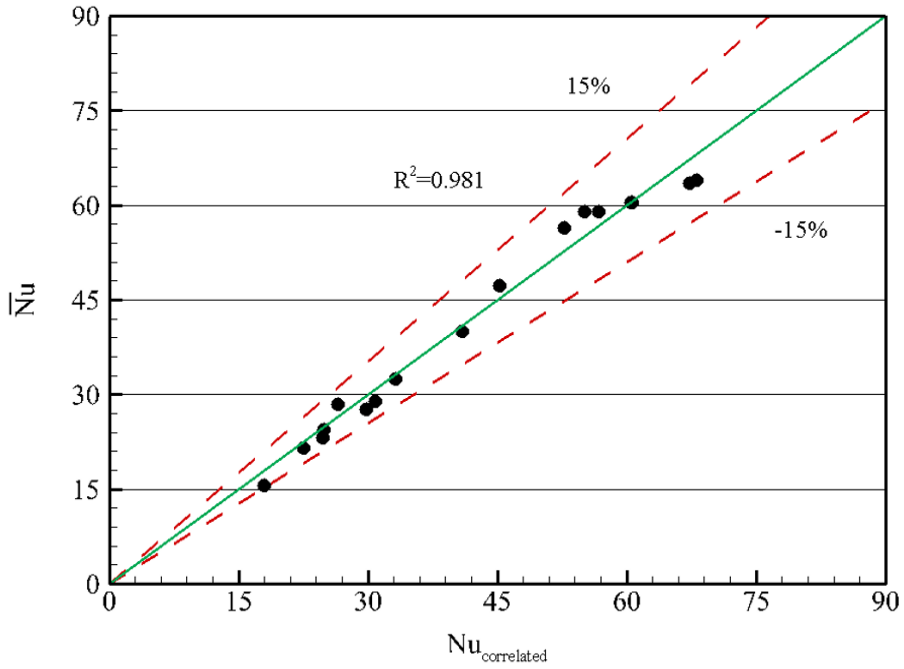

Figure 30: Correlation of convective heat transfer coefficient inside cylindrical tanks indicating the goodness of fit

Table 6: Data related to experimental tank of Murthy et al. (1992)

Dimensions	
Hot water tank volume (m^3)	0.215
Tank height (m)	0.65
Tank wall thickness (m)	0.001
Tank material	Aluminium
Insulation material	Glass wool
Aluminium thermal properties (assumed)	
Density (kg/m^3)	2719
Specific heat capacity (J/kgK)	871
Thermal conductivity (W/mK)	202.4
Glass wool thermal properties (assumed)	
Density (kg/m^3)	40
Specific heat capacity (J/kgK)	2300
Thermal conductivity (W/mK)	0.038

to water and wall can be shown in Appendix D. As for the boundary conditions, the tank was set to lose heat to the surroundings at 20°C, subject to external natural

convection heat transfer coefficients of 2 W/m^2K for the top node, 6 W/m^2K for the intermediate nodes and 4 W/m^2K for the bottom node. These values were adopted from experimental measurements from Murthy et al. (1992). As before, the thermophysical properties of water were recalculated at the average temperature between T_f and T_{env} for each time step.

The temperature profiles after 6 hours of standby period are shown in Figure 31. From this, it was observed that the proposed Nusselt correlation can predict the change of temperature distribution inside the tank reasonably in good agreement with the experimental data. The variations could be attributed to assumptions made on tank material thermal properties due to lack of data from Murthy et al. (1992). In Figure 31, predicted water temperature at the top section of the tank was slightly lower than the actual tank temperature. This can be associated with the fact that the correlation was developed based on less stratified tank with temperature difference of less than 2°C while the tank of the chosen study was initially highly stratified with temperature difference of about 40°C, which noticeably suppresses natural convection heat transfer inside the tank.

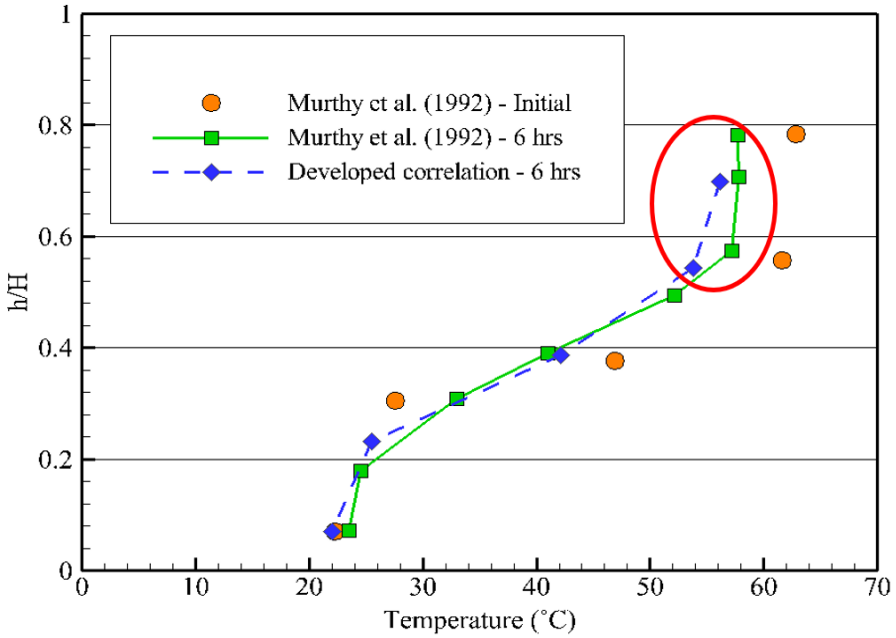

Figure 31: Comparison of prediction of axial temperature profiles between proposed correlation and existing correlations for initially stratified tank after 6 hours of standby operation.

3.6 Conclusion

This chapter provides analysis on steady state heat loss from vertical cylindrical storage tank. The results show that natural convection heat transfer inside the tank is significantly governed by convection heat transfer on the side wall at which the buoyancy induced boundary layer develops. It was also shown that increasing the aspect ratio reduces natural convection heat transfer inside the tank. This is because the degree of stratification becomes higher with increasing aspect ratio, which restricts the downward flow velocity of side wall boundary layer and makes convection heat transfer on the side wall less efficient.

Based on the findings, a new generalized correlation was developed that can predict natural convection heat transfer coefficient independent of initial condition of the tank and cooling time. Given the importance of being able to predict the convective heat

transfer coefficient in the analysis of heat loss from solar storage tanks, the developed correlation will significantly aid in designing solar storage tanks.

Chapter 4

Effect of baffles on heat loss from a solar hot water tank

4.1 Introduction

In Chapter 3, it was shown that the boundary layer flow on the side wall of the tank has a marked impact on the tanks heat loss. Thus, this purpose of this chapter was to find a way to suppress or control this flow in hope of reducing the convective heat transfer coefficient and subsequently the rate of heat loss from the tank. In essence we could increase the thermal resistance due to convection, as shown in Figure 32.

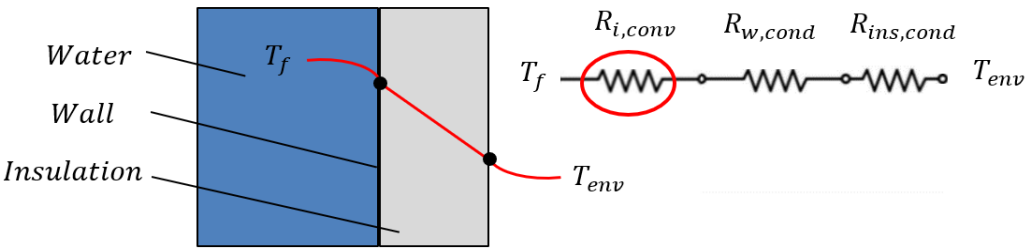

Figure 32: Thermal resistance network for static heat loss to the ambient

One way the suppression of flow inside the tank could be achieved, is by using passive baffles mounted inside the tank. Altuntop et al. (2005) numerically investigated the use of different shapes of baffle plates to minimize mixing near the hot water inlet of a tank during charging. The results showed that placing a baffle plate could alter the flow of hot water entering the tank and lead to better thermal stratification.

Similarly, Bouhal et al. (2017) examined the effect of tilting baffle plates at different angles inside a tank on mixing near the inlet and outlet of a tank. The finding showed that rotating baffles at different angles led to different flow alterations of hot water entering the tank, that altered mixing to varying extents.

From the studies mentioned above, it was apparent that the shape and position of passive baffles can be strategically chosen to suppress or alter the targeted flow that occurs inside a tank. Having said that, in the preceding chapter it was shown that the side wall had a significant impact on the heat loss. Therefore, if the boundary layer flow on the side wall could be suppressed from progressing towards the bottom region, this could lead to a reduction in the rate of heat loss from a tank. On this basis, it was decided to examine the effect of placing a passive cylindrical jacket baffle, parallel to the side wall, on the internal convective heat transfer coefficient.

4.2 Baffle configuration

Using a passive baffle, the intention was to provide a channel for cooled water from the boundary layer to be collected which would then redirect continuously falling boundary layer towards the inner side of the baffle due to stratification. The baffle configuration considered is shown in Figure 33.

As can be seen from Figure 33, a cylindrical passive baffle jacket was mounted inside the tank parallel to the side wall. Given that this study is a first attempt to explore the effect of baffle on natural convection in a storage tank, it is important to

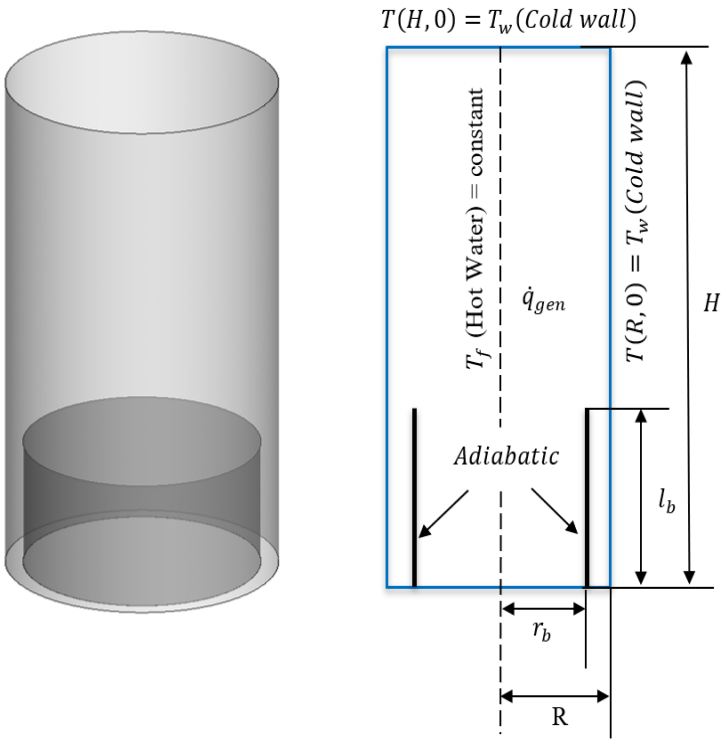

Figure 33: Passive baffle configuration of CFD model (a) Geometry and (b) Boundary conditions

fully understand the influence its geometrical parameters on heat transfer independently before incorporating the impact of its thermal conductivity. As such, it was assumed that the wall of the baffle was thin and did not have significant conduction heat transfer across the wall (i.e. a thin adiabatic fin). To examine how the proportions of such a baffling system would influence both heat transfer and flow within the tank, three baffle placements were considered, 6.5%, 13% and 26% of the tank radius. In addition, three baffle lengths were modelled, 25%, 50% and 75% of the tank height.

For this study two tanks of 169 L and 402 L volume and with aspect ratios of 1, 2.3 and 2.8 were considered. The characteristic length was taken to be the ratio of volume over surface area, and physical properties were calculated at the mean temperature between the water and the wall. All the investigated cases were modelled using the

same CFD methodology used in Chapter 3. In addition, the validated computational methodology in Chapter 3 will be sufficiently enough to be used for investigating the effect of baffle on natural convection heat transfer given that similar approach was successfully used in the previous studies (Pushpa, 2020, Fishbaugher, 1988).

4.3 Results and Discussion

The perceived benefit of placing a baffle inside the tank was to divert the sinking boundary layer flow towards the inner side of the baffle away from the side wall, where heat loss occurs. In Figure 34, it can be seen that the longest baffle placed closest to the side wall appears to achieve this to a certain extent, due to the presence of a stratified region between the baffle and the side wall (see Figure 35). In this jacket, the velocity of the boundary layer flow is also noticeably reduced compared to the tank without the baffle. It is important to note however that this flow behavior was achieved with the assumption that baffle jacket is adiabatic with no conduction heat transfer across it.

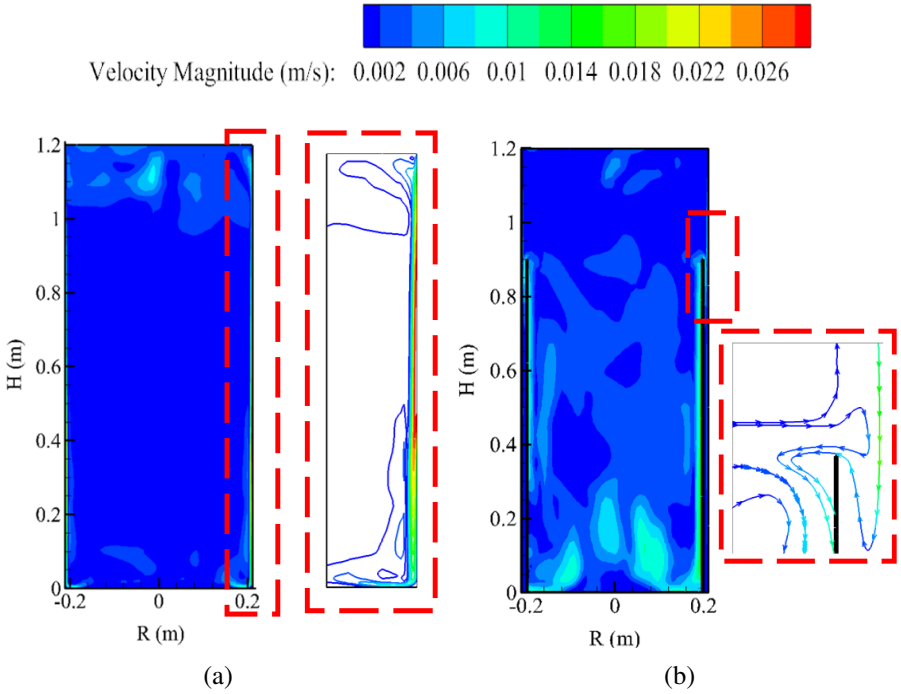

Figure 34: Velocity contours for tank model (V=169L, AR=2.8) at the center plane with (a) no baffle and (b) baffle at ((R-r_b)/R=0.065, l_b/H=0.75)

Similarly, in Figure 36, it is shown that baffles with shorter lengths, 50% and 25% of the height, were still able to redirect the boundary layer flow away from the side wall. However, it was also observed that shortening the length of the baffle allows boundary layer to grow and reach higher velocity in comparison to that of longest baffle, as shown in Figure 36(b), which could potentially enhance convection heat transfer inside the tank.

By diverting the boundary layer flow, and restricting it from flowing along the side wall, there is a marked decrease in convection heat transfer, as represented by Nusselt number in Figure 37. Here, it can be seen that all baffle configurations result in lower convection heat transfer when compared to the tank without a baffle. In addition, Nusselt number decreases with increasing baffle length since the growth of boundary layer and its velocity is proportional to the baffle length, as discussed before.

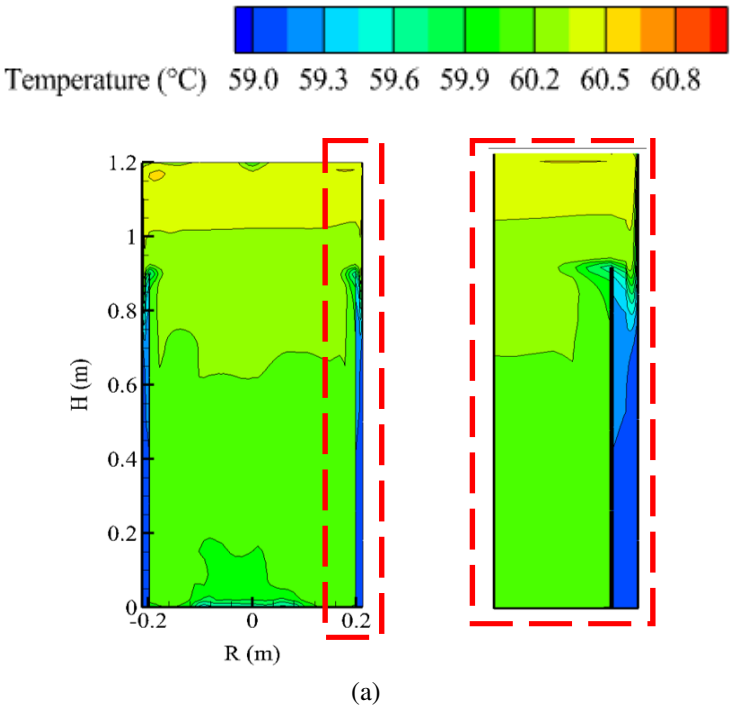

Figure 35: Temperature contour for tank model (V=169L, AR=2.8) at the center plane with baffle at ((R-r_b)/R = 0.065, l_b/H = 0.75)

In Figure 37, it can be seen that the position of baffle jacket also plays an important role in limiting convective heat transfer inside the tank. Figure 38 shows the temperature contours of different baffle positions for a fixed medium baffle length (50% of tank height). As can be seen from the Figure 38, increasing the distance between the baffle and the side wall allows boundary layer flow (thermal plume) to sink further along the side wall. This results in an increase in convection heat transfer as indicated by the increase in the average Nusselt number in Figure 37.

Interestingly, the Nusselt number in the case with the shortest baffle length (25% of tank height), placed at 6.5% of tank radius from the side wall was higher than that of 13%. To explain this, velocity contours of both cases were shown in Figure 39. In Figure 39, it can be seen that placing a baffle close to the wall results in a recirculation cell in the vicinity of the top of the baffle, while this cell is absent when the baffle is placed further from the side wall (13% of tank radius). The presence of this recirculation

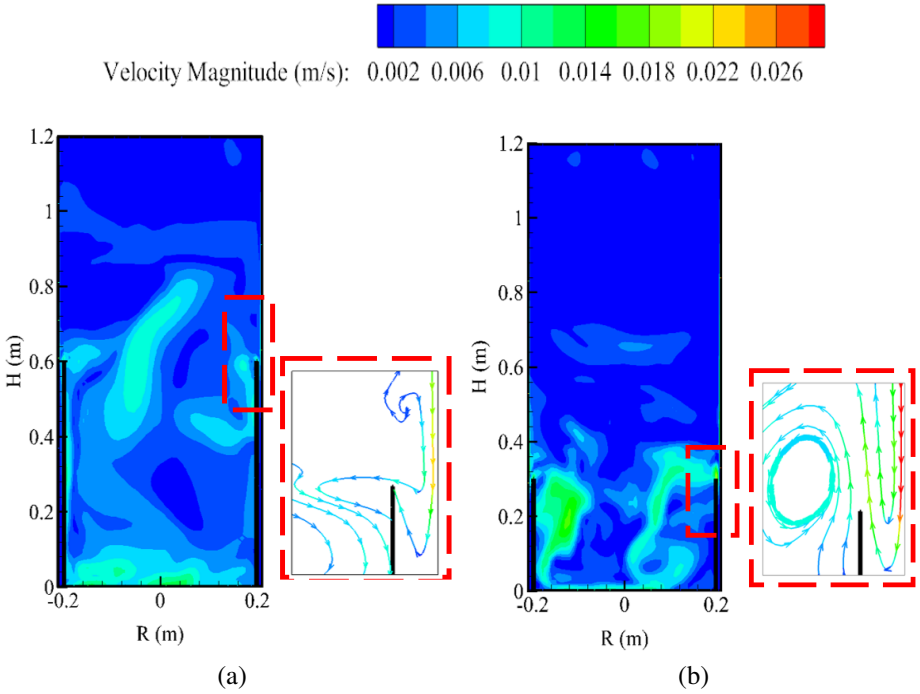

Figure 36: Velocity contours for tank model (V=169L, AR=2.8) at the center plane with baffles at (a) ((R-r_b)/R=0.065, l_b/H=0.5) and (b) ((R-r_b)/R=0.065, l_b/H=0.25)

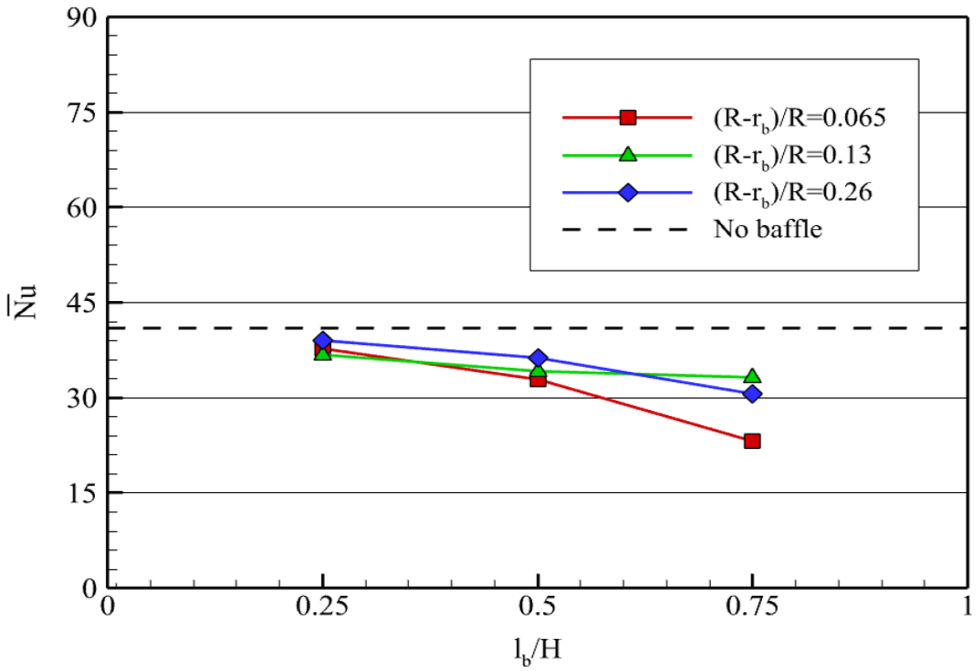

Figure 37: Variation of overall Nusselt number with different baffle lengths and positions

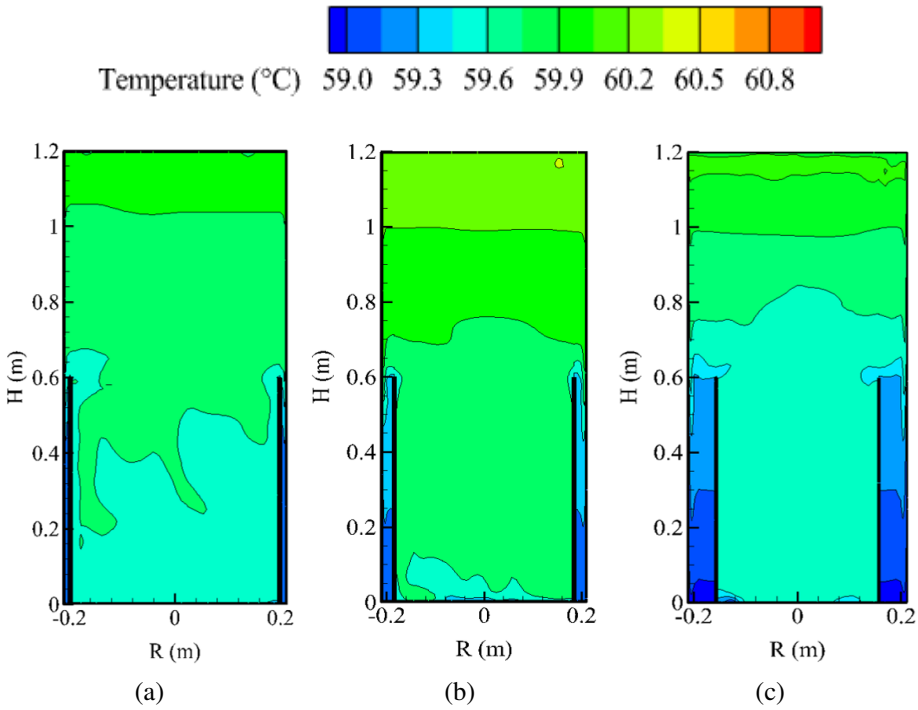

Figure 38: Temperature contours of tank models with baffles (a) (R-r_b)/R=0.065, (b) (R-r_b)/R=0.13 and (c) (R-r_b)/R=0.26 for a fixed baffle length of l_b/H=0.5

flow marginally increases convection heat transfer on the side wall while the other tank walls remain unaffected, as indicated by the Nusselt number for each wall in Figure 40. The formation of this recirculation cell could be associated with the perturbation of the boundary layer flow when it meets the baffle, due to the small gap between the baffle and the side wall relative to the boundary layer thickness.

From Figure 37, it was also worth noting that the Nusselt number in the case with longest baffle length (75% of tank height), placed at 13% of tank radius from the side wall was higher than that of 26%. To explain this, velocity contours of both cases are shown in Figure 41.

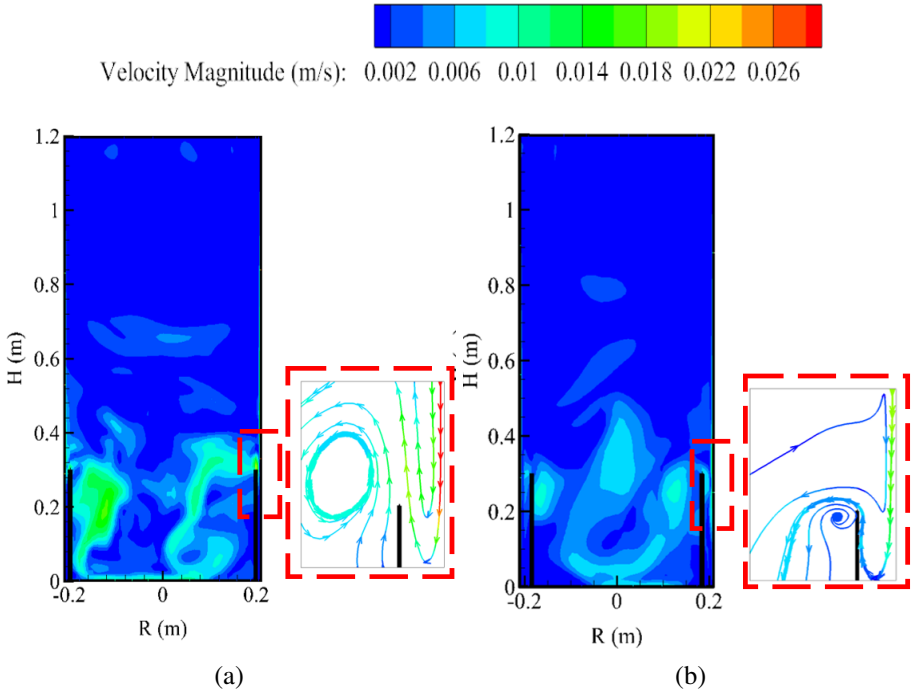

Figure 39: Velocity contours of tank models with baffles (a) (R-r_b)/R=0.065 and (b) (R-r_b)/R=0.13 for a fixed baffle length of l_b/H=0.25

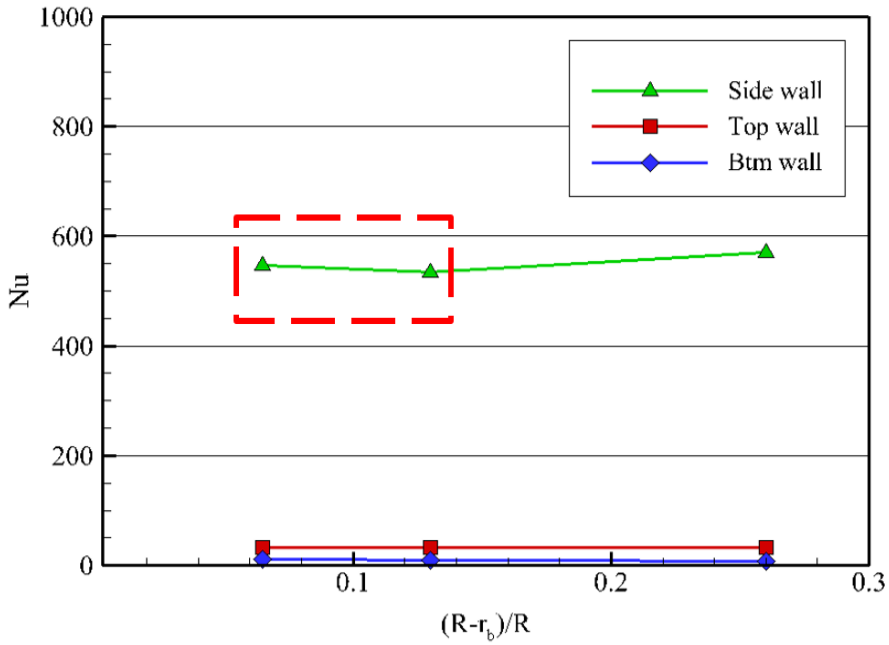

Figure 40: Variation of Nusselt numbers on each wall for different baffle positions for a fixed baffle length (l_b/H=0.25)

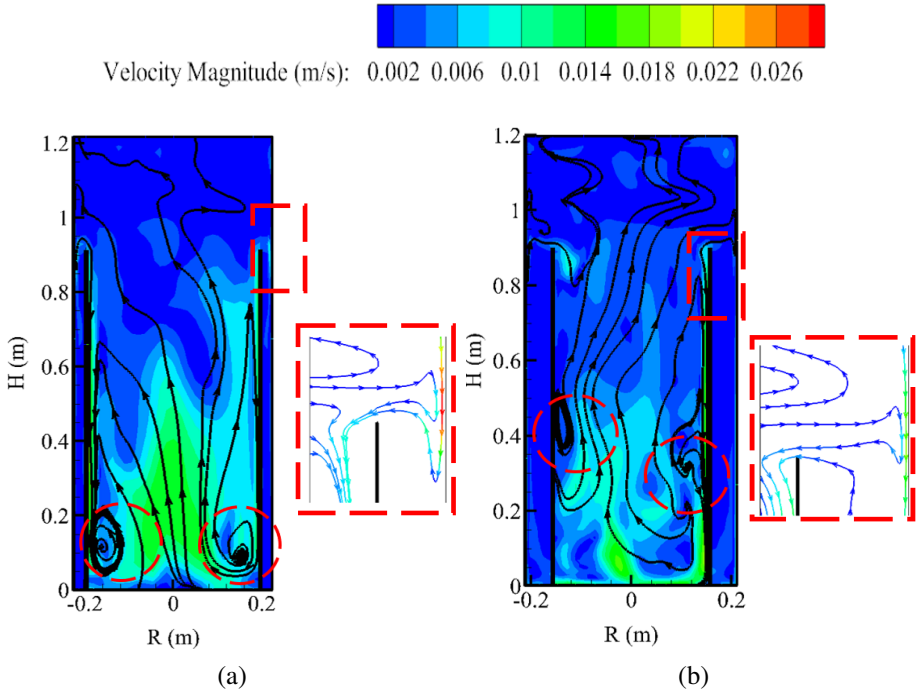

Figure 41: Velocity contours of tank models with baffles at (a) (R-r_b)/R=0.013 and (b) (R-r_b)/R=0.26 for a fixed baffle length of l_b/H=0.75

In Figure 41, it is apparent that the majority of the boundary layer flow is redirected along the inner baffle wall without getting cooled by the exterior wall, leading to the formation of recirculation cells at the bottom. Because of this, a portion of existing hot water rises and meets with the falling boundary layer near the top end of the baffle. This increases the temperature of water inside the boundary layer which leads to an increase in its velocity. However, the increase in the velocity of the boundary layer is more pronounced when the baffle is placed at 13% of tank radius from the side wall compared to that of 26% (see Figure 41). This is because placing the baffle further away from the wall (26% of tank radius) allows part of the boundary layer flow to continue sinking along the side wall instead of getting diverted into the baffle jacket, resulting in weak recirculation cells compared to when baffle is placed nearer to the wall (13% of tank radius). This phenomenon affects convection heat transfer on the side wall while other tank walls remain unaffected, as represented by Nusselt number for each wall in

Figure 42.

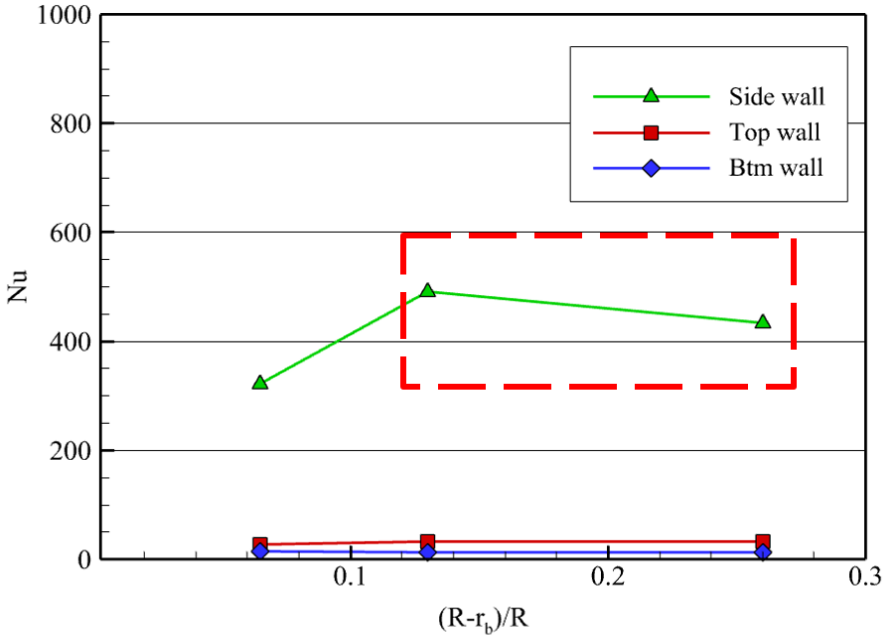

Figure 42: Variation of Nusselt numbers on each wall for different baffle positions for a fixed baffle length (l_b/H=0.75)

After analyzing the effect of baffle configuration on natural convection inside the storage tanks, it was decided to examine the influence of aspect ratio on natural convection heat transfer inside these tanks. From Figure 43, it can be observed that increasing the aspect ratio decreases natural convection heat transfer inside the tank as indicated by the reduction in Nusselt number.

To explain this, velocity contours of the tank model with baffle length (25% of tank height) placed at a distance of 13% of tank radius from the side wall were shown in Figure 44. As can be seen from the Figure 44, the portion of buoyancy driven boundary layer flow on the side wall that was redirected towards the core of the tank away from the side wall increases with increasing aspect ratio. In aspect ratios of 1 and 2.3, recirculation cell was observed on the inner side of the baffle owing to small portion of boundary layer flow that is redirected by the baffle. However, this recirculation flow

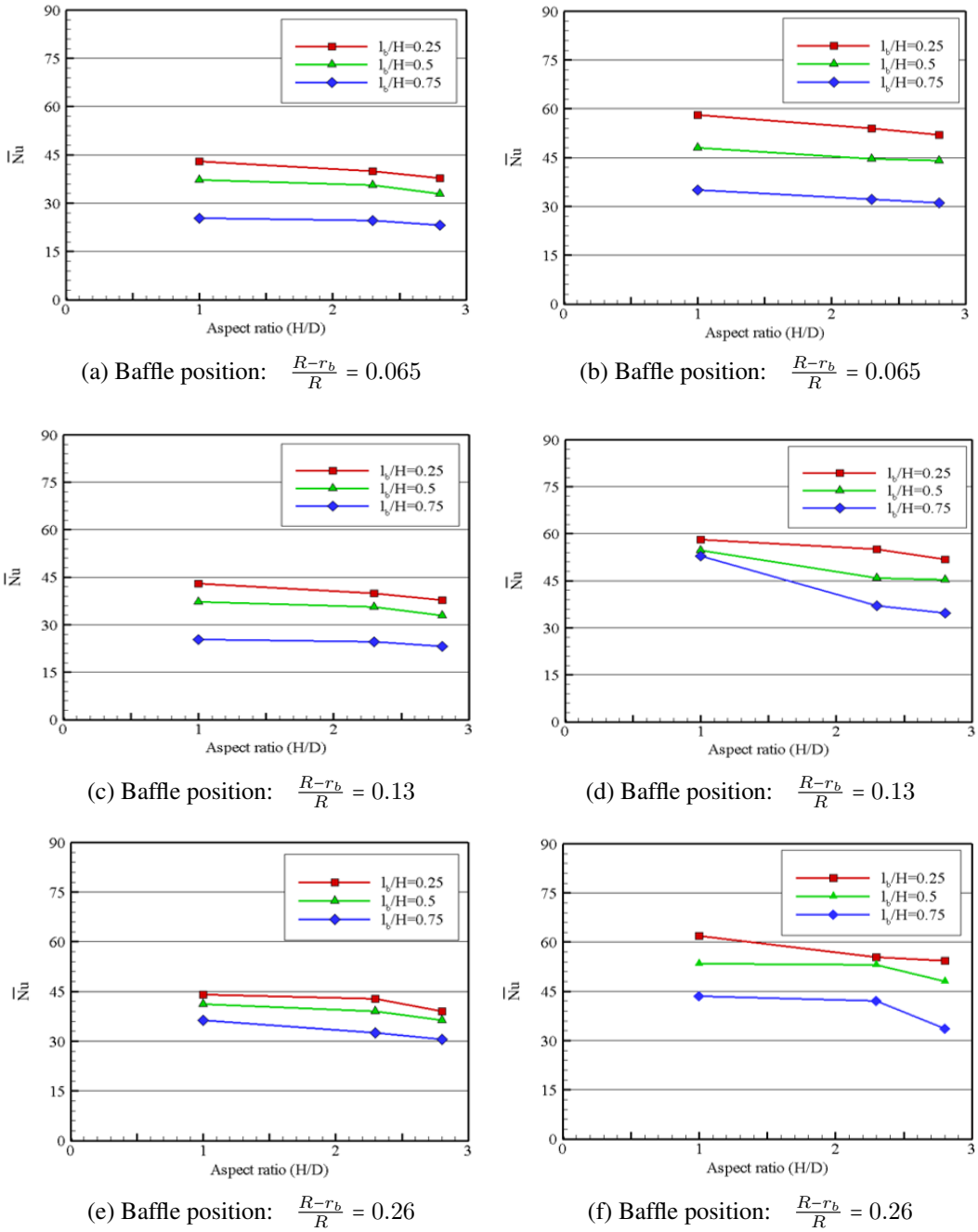

(a) Baffle position: $\frac{R-r_b}{R}$ = 0.065 (b) Baffle position: $\frac{R-r_b}{R}$ = 0.065

(c) Baffle position: $\frac{R-r_b}{R}$ = 0.13 (d) Baffle position: $\frac{R-r_b}{R}$ = 0.13

(e) Baffle position: $\frac{R-r_b}{R}$ = 0.26 (f) Baffle position: $\frac{R-r_b}{R}$ = 0.26

Figure 43: Effect of aspect ratio on natural convection heat transfer for different baffle configurations for tank volumes of V = 169L (left) and V = 402L (right)

disappears as an increasing portion of boundary layer flow is redirected away from the side wall inside the tank with aspect ratio of 2.8. This is due to an increase in the momentum of boundary layer flow with aspect ratio which gets disturbed by the

presence of the baffle and forced to enter the inner side of the baffle. This results in a decrease in convection heat transfer on the side wall, as shown in Figure 45 (a).

On the other hand, thermal stratification inside the tank proportionally increases with aspect ratio, as indicated in Figure 45 (b). As a result, natural convection heat transfer on the top wall gets also restricted with increasing aspect ratio, leading to a decrease in convection heat transfer coefficient, as shown in Figure 45 (a). However, no notable natural convection on the bottom wall was observed. Similar changes flow behavior was observed in remaining tank models with different baffle configurations, thus leading to a decrease in Nusselt number with increasing aspect ratio.

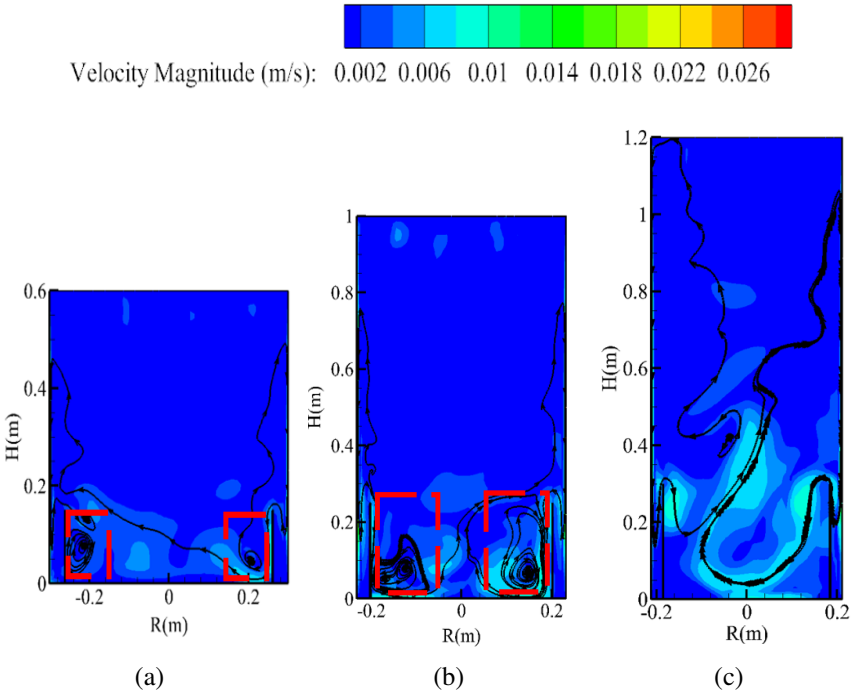

Figure 44: Velocity contours of tank models (V=169L) with (a) AR=1, (b) AR=2.3 and (c) AR=2.8 for a fixed baffle (l_b/H=0.25, (R-r_b)/R=0.013)

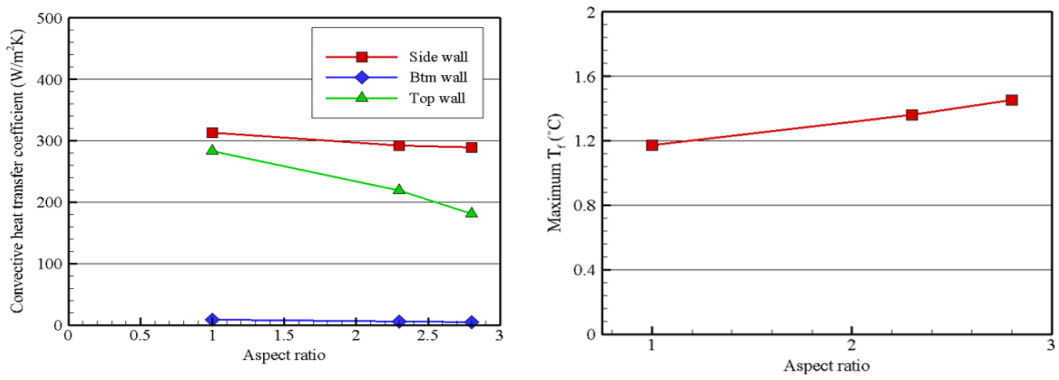

(a) (b)

Figure 45: . (a) Variation of local convective heat transfer coefficient on each tank wall and (b) Maximum temperature difference inside the tank for tank model (V=169L) with a baffle (l_b)/H=0.25, (R-r_b)/R=0.013)

4.4 Development of a correlation for convective heat transfer coefficient inside hot water tanks equipped with baffles

In the previous section, the effect of varying baffle lengths and jacket widths on convective heat transfer inside a representative tank were discussed. Having realized that jacket baffles can reduce the internal convective heat transfer coefficient, an equation to describe the convective heat transfer coefficient with baffle parameters (length and channel width) was developed in order to be able to predict heat loss which can be very useful for design purposes.

To obtain a correlation of convective heat transfer coefficient that is applicable to domestic hot water tanks of different configurations, the results of convective heat transfer coefficients obtained from the simulation are fitted through multiple nonlinear regression and correlated, as shown in Equation (17).

$$Nu = c\, Ra^{m} \left(\frac{H}{D}\right)^{n} \left(\frac{l_b}{H}\right)^{o} \left(\frac{R - r_b}{R}\right)^{p} \tag{17}$$

Where, c, m, n, o and p are constants.

Based on the results, the best fit coefficients were shown to be c = 0.354, m = 0.259, n = -0.035, o = - 0.291 and p = 0.054. The proposed Nusselt correlation is shown in Equation (18). Different coefficients of c, m, n, o and p may be needed for enclosures exceeding the limit of 2.89 × 10^7< Ra_T < 1.24 × 10^8 and 1 < AR < 2.83.

$$\bar{Nu} = 0.354\ Ra_T{}^{0.259}\ (\frac{H}{D})^{-0.035}\ (\frac{l_b}{H})^{-0.291}\ (\frac{R-r_b}{R})^{0.054} \tag{18}$$

In Figure 46, the fitted Nusselt number correlation using multiple non-linear regression is plotted against the simulated Nusselt number. As can be seen from Figure 46, the proposed Nusselt correlation shows a good agreement with all the simulated data set, with a goodness of fit of R^2 = 0.952.

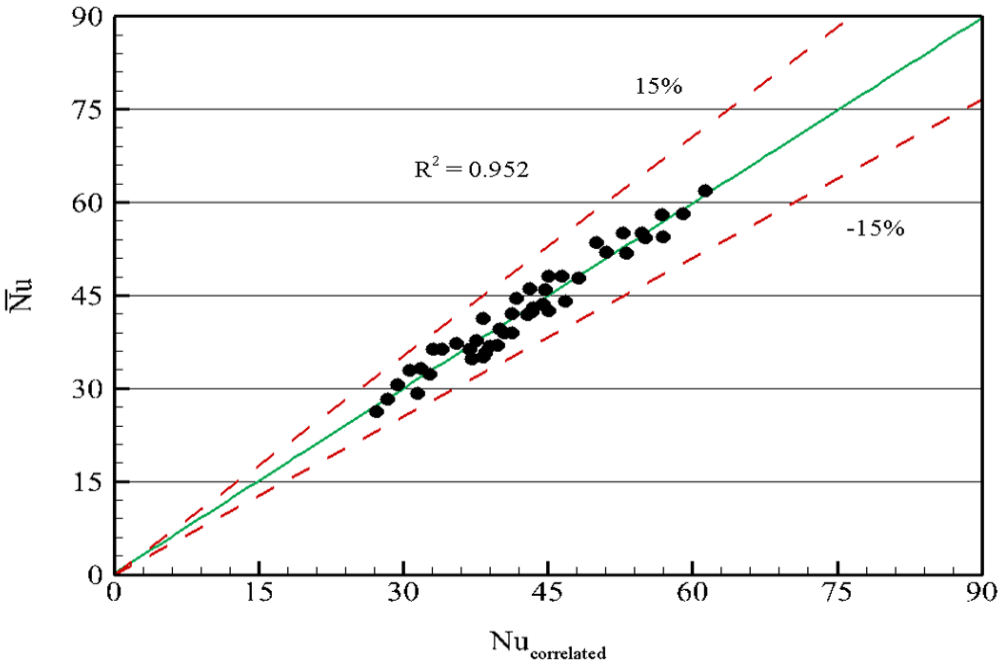

Figure 46: Correlation of convective heat transfer coefficient inside cylindrical tanks with baffles indicating the goodness of fit

Having developed the Nusselt number correlation for tanks equipped with baffle jackets, it was decided to examine the effectiveness of baffle in reducing convection

heat transfer inside solar storage tanks. To achieve this, longest baffle (75% of tank height) placed at 6.5% of tank radius from the wall that results in lowest convection heat transfer was chosen.

Figure 47 shows Nusselt numbers for a vertical hot water cylinder with 169 L for different aspect ratios. Here, it can be seen that a maximum of more than 40% reduction in Nusselt number could potentially be achieved by using a simple vertically mounted cylindrical baffle arrangement. As such, the use of baffle could serve as an additional way to reduce convection heat transfer inside the tank on top of convectional insulation.

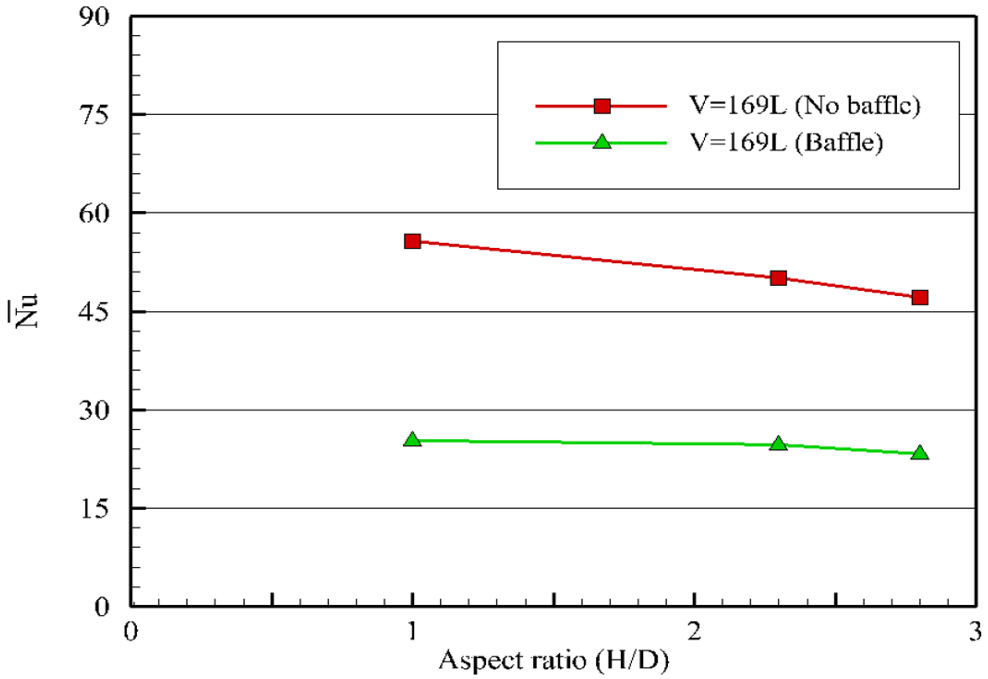

Figure 47: Effect of baffle jacket on convection heat transfer for tank model (V = 169L) with different aspect ratios

4.5 Conclusions

In this chapter, the effect of placing passive baffle geometry on natural convection heat transfer inside a vertical cylindrical storage tank was analyzed.

The results show that changing the length of a baffle jacket has a more pronounced effect on natural convection heat transfer inside the tank compared to varying baffle jacket position. Moreover, baffle jacket having the highest length and placed nearest to the side wall leads to lowest natural convection heat transfer inside the tank.

Based on the findings, a new generalized correlation that can predict natural convection heat transfer inside tanks with baffle jacket was developed. It is hoped that engineers that design these systems can take advantage of the obtained correlation to improve the thermal performance of these tanks with passive baffle in the future.

Chapter 5

Air gap insulation on heat loss from a solar hot water tank

5.1 Introduction

In Chapter 4, it was shown that natural convection heat loss from solar storage tanks can be reduced by using a simple vertically mounted cylindrical baffle jacket. The aim of this chapter was to find ways that could lower heat loss from the tank even further by attempting to bring improvements in the thermal resistance offered by an insulation, as shown in Figure 48.

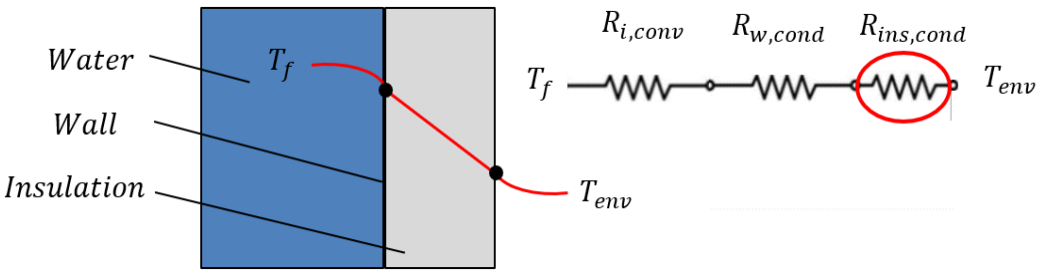

Figure 48: Thermal resistance network for static heat loss to the ambient

Shyu and Hsieh (1987)- attempted to improve the performance of a tank by exploring the effect of insulation placement on heat loss. It was shown that the conventional method of insulating the wall on the outside, while being able to reduce heat loss to the ambient, resulted in downward heat conduction through the wall. This leads to an increase in natural convection heat transfer inside the tank due to mixing of stratified water layers. However, it was shown that this can be rectified by insulating the wall on the inside while maintaining the same reduction in heat loss as the outer insulation. Given this advantage, Gasque et al. (2015) numerically investigated the influence of the inner tank lining material on heat loss. Their results indicated that the thermal conductivity of the lining material was one of the main factors that affects the thermal performance and should be kept low to minimize heat loss from stored hot water.

With regards to insulation materials, solar storage tanks are often insulated with convectional building insulation materials such as Polyurethane (PU), expanded polystyrene (EPS), Polyisocyanurate (PIR) and mineral wool. However, it is a challenge to obtain a good insulation quality (high thermal resistance to heat loss) using convectional insulation. This is because an insulation thickness considerably larger than the diameter of the tank would be required to achieve a good insulation performance due to their limitation in thermal conductivity, which is often impractical (Fantucci et al., 2015).

In an attempt to achieve quality insulation performance with practical insulation thickness, Omer et al. (2007) reviewed and evaluated different insulation materials used in solar hot water cylinders including organic and inorganic foams, composite insulations and vacuum insulation panels. Their findings indicate that vacuum insulation panels (VIP) offer the best performance in terms of heat loss. However, there is a need to maintain the desired vacuum level during the operation, which could impose a considerable amount of additional maintenance cost throughout their lifetime.

Having said that, it is worth noting that even if a perfect vacuum cannot be achieved a layer of trapped air (or other gas) can have an extremely low conductivity. And

thus, with good design, may be an alternative form of insulation. In line with this, natural convection heat transfer across the air space between two vertical boundaries at different temperatures has been extensively studied in the literature, especially in buildings (Billington, 1952, Batchelor, 1954). Billington (1952) showed that a narrow unventilated air gap in the interior of a wall can impede the heat loss significantly, compared to the case without the air gap, for the same temperature difference between the two outer surfaces of the wall.

The earliest study on free convection across a closed rectangular cavity with differentially heated vertical walls was conducted by Batchelor (1954). Referring to air cavities used for insulation of buildings, the aspect ratios of 5 to 200 and Rayleigh number of up to 106 were used. Different flow regimes were identified, and the authors suggested criteria for laminar flow in terms of Rayleigh numbers and aspect ratios along with expressions for Nusselt number. They also shown that the effect of convection can be neglected for gap sizes less than 1 cm since the gap is too small for a notable convection to take place and conduction is the dominant mode of heat transfer. In addition, their findings suggest that as the gap size increasers, heat transfer coefficient decreases due to transition from conduction to convection heat transfer, but no further decrease in heat transfer coefficient takes place for gaps larger than 2.5 cm for any cavity height because beyond this gap size, laminar flow becomes impossible. Similar to rectangular air cavities, cylindrical annular cavities can also be used as thermal insulation in plenty of practical applications including cooling of fuel assemblies for different nuclear power plants, passive cooling of power transformers, and storage tanks of many varieties (Lin and Akins, 1986).

Natural convection heat transfer in annulus between two concentric cylinders with differentially heated isothermal walls have been studied extensively in the literature (Elder, 1965, Emery and Chu, 1965, Davis and Thomas, 1969, Rubel and Landis, 1969, Thomas and de Vahl Davis, 1970, Lee et al., 1982, Prasad and Kulacki, 1985, Kumar

and Kalam, 1991, Fishbaugher, 1988). Similarly, natural convection in enclosures between hot bottom plate and cold top plate has been investigated in the literature (Malkus and Veronis, 1958, Willis and Deardorff, 1965, Goldstein, 1969, Rossby, 1969, Krishnamurti, 1970, Chu and Goldstein, 1973, Garon and Goldstein, 1973, Hollands et al., 1975). However, the effectiveness of using 'trapped' air as an insulation for solar storage tanks has received little attention in the literature.

Sparrow and Charmchi (1983) investigated natural convection in the space between concentric vertical cylinders of different heights and diameters. However, the diameter ratios of inner cylinder to outer cylinder considered in their study were between 0.1 and 0.3, which is not applicable for insulation of solar storage tanks in which diameter ratios are within 0.75 and 0.98, in correspondence to typical tank insulation thickness between 1 cm and 10 cm. Nithiarasu et al. (n.d.) studied the natural convection in a flipped L-shaped enclosure for gap to length ratios of 0.6 and 0.8. However, the study is associated with rectangular cavity and is only applicable to laminar convection. Recently, Medebber (2020) studied transient laminar natural convection in a vertical cylindrical annulus but the diameter ratios of considered annular cavity was 2, which does not correspond to the range of tank insulation thickness.

Previous studies explored means to improve the performance of tank insulation and found that vacuum insulation panels offer the best performance. Given the high maintenance costs associated with vacuum panels, it is viable to achieve a portion of performance offered by vacuum insulation using trapped air space as a form of insulation, which has been extensively studied for use in buildings but not for solar storage tanks.

In light of this, it was decided to examine heat transfer inside the air gap encapsulating the solar hot water cylinder and assess its effectiveness as an insulation.

5.2 Problem Formulation and Numerical Method

In the case of vertical cylindrical solar storage tanks, insulation is typically wrapped around the entire tank but for an air gap, which minimizes heat transfer through weak natural convection instead of conduction, it may not be effective to insulate the bottom of the tank because air between the bottom wall of the tank and insulation is stratified. Because of this, strong natural convection is not likely to take place because for hot air adjacent to the tank bottom wall, it needs to travel laterally along the wall until it reaches the circumference of the tank before it can rise due to buoyancy. On the other hand, insulating the top of the tank can effectively reduce the rate of heat loss because the top section of the tank holds the hottest water. Similarly, the side of the tank is also worth insulating because majority of heat loss takes place through the sidewall since its surface area of heat transfer is higher compared to other walls.

Having said that, a simple air gap insulation around a solar storage tank would be an inverted U-shaped enclosure which insulates side and top walls of a tank (like an inverted 'Thermos' flask). This chapter examines the natural convection that takes place inside an inverted U-shaped air gap encapsulating a vertical cylindrical solar storage tank.

To do this, an axisymmetric CFD model was developed using ANSYS Fluent 19.4. This approach has been successfully used to investigate natural convection of air inside enclosure (Davis and Thomas, 1969, Sparrow and Charmchi, 1983). Considering the computational time, water inside the tank was not included as part of the computational domain but instead, the air gap was considered to be trapped between differentially heated cylinders with isothermal walls, which allows the problem to be solved at steady state conditions.

The computational domain consists of a fluid (air) domain and two solid (tank) walls. The inner tank wall is made of hot water cylindrical tank model that has an aspect ratio

of 1.6 with a height of 0.865 m and a diameter of 0.542 m, resulting in a storage capacity of 200 L. The whole flow domain was paved with a coarse mesh with a maximum grid size of 2 mm except the regions close to the tank wall where concentrated grid points were created by inflating the grid with 10 layers having a first-layer thickness of 0.05 mm and a growth rate of 1.2.

For the boundary conditions, the no slip condition was applied on both walls, while the symmetry condition was used at the center of the tank in the momentum equations. In the energy equation, the inner tank wall was held at a constant temperature (T_{w1}) while the outer wall was held at a lower constant temperature (T_{w2}). It was also assumed that the bottom end wall was adiabatic. The hot wall was fixed at $60°$C and the isothermal outer wall was assumed to be at $20°$C, as shown in Figure 49.

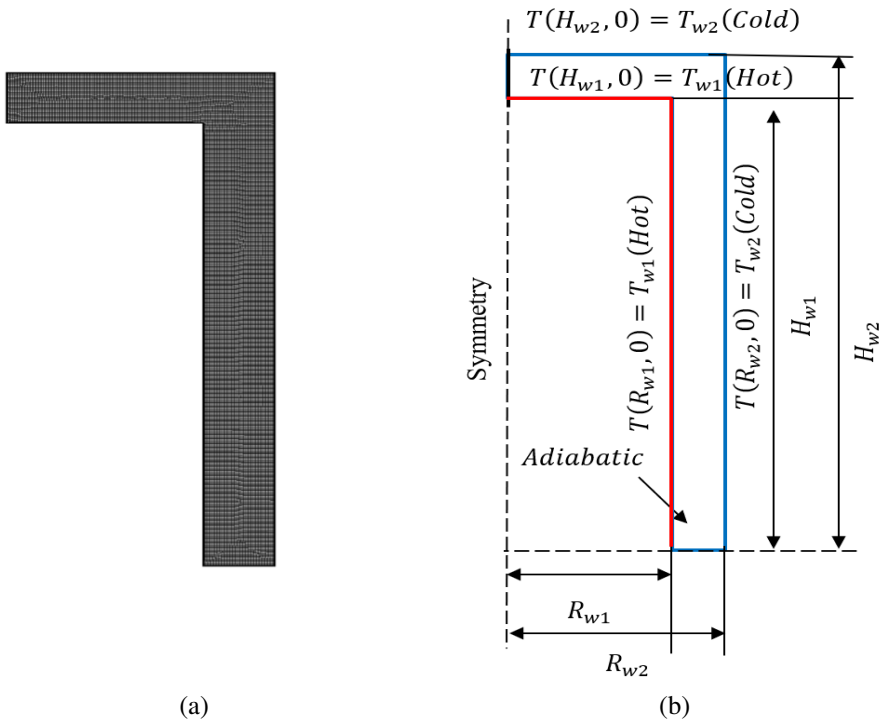

Figure 49: Developed CFD model of air gap (a) mesh and (b) boundary conditions

The distance between the two walls was varied in the range of 1 to 10 cm, following the typical range of insulation thickness used in storage tanks. Both uniform and non-uniform variation of air gap sizes were considered, as shown in Figure 50. In addition, the aspect ratio of the inner wall, (H_{w1}/R_{w1}) was varied between 1.5 and 6. This was done to examine how changes in geometry influenced both the heat transfer and flow within the enclosure.

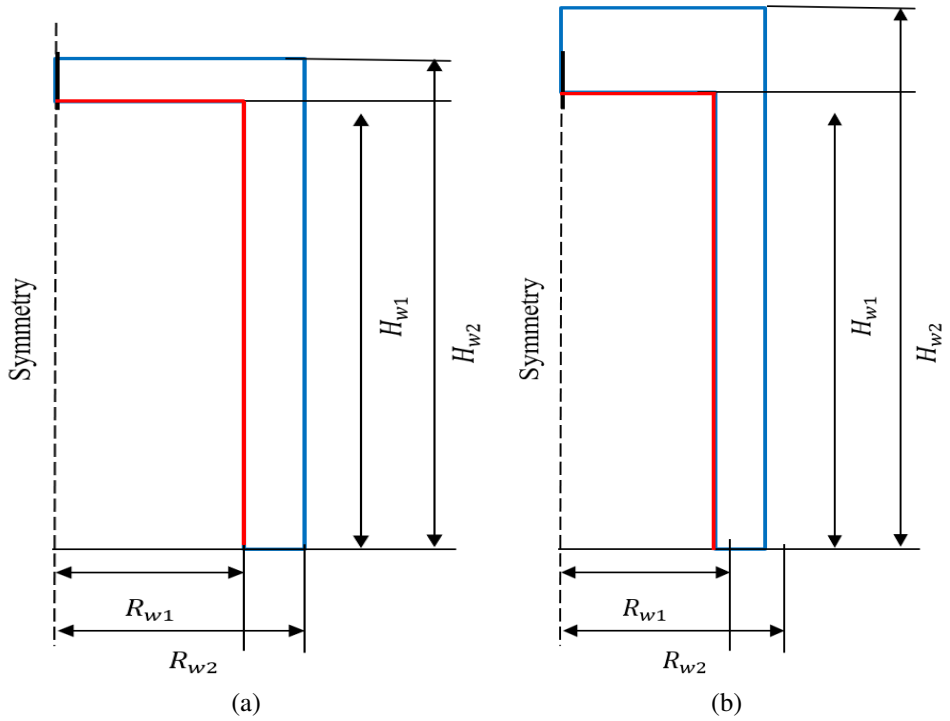

Figure 50: Different air gap geometries considered (a) Uniform and (b) Non-uniform

Before the CFD model can be solved, it was necessary to determine the flow regime of natural convection that takes place in the cavity. The Rayleigh number for natural convection between differentially heated walls of an annular or coaxial cavity, Ra_T can be defined as in Equation (19) with the characteristic length being the size of an annular cavity.

$$Ra_T = \frac{g\beta_f(\bar{T}_f - \bar{T}_w){L_c}^3}{\upsilon_f \alpha_f} \tag{19}$$

Davis and Thomas (1969) reported that laminar regime can be obtained for $Ra_T < 2 \times 10^5$ for natural convection of air inside annular cavity. On the other hand, Hollands et al., (1975) discussed about the flow regime inside a coaxial cavity and concluded that a transition to turbulence is expected around Rayleigh number of 4.8×10^3 as observed by Krishnamurti (1970) and 6.3 x $10^3 < Ra < 10^4$ by Willis and Deardorff (1965). Calculation of Rayleigh number for current study results in the range between 10^4 and 10^7 for both annular and coaxial gap in a U-shaped air cavity, and thus it was decided to model turbulence with the realizable k-epsilon model which has proven to be suitable for simulating natural convection inside cavities (Rincón-Casado, 2017, Altaç and Uğurlubilek, 2016).

For the given temperature range between the inner cylindrical wall temperature of $60°$Cand the outer cold cylindrical wall temperature of $20°$C the change in density of air inside the cavity can be assumed to be a linear function of temperature. As such, the Boussinesq approximation was used with the thermal expansion coefficient of air evaluated at the reference temperature of $40°$C the average temperature of the two walls.

A mesh sensitivity analysis was performed using the Grid Convergence Index (GCI) proposed by Roache (1998) with two different grids having maximum cell sizes of 1 mm and 2 mm. Since the order of the solver method (p_m) and the mesh refinement ratio (r_m) are equal to 2 in this study, the GCI with the safety coefficient (f_s) of 3 directly reflects the relative error of the solutions obtained from two different meshes. The GCI observed based on heat flux of the inner hot wall was only 0.57% between the finer and coarse grid sizes, indicating that a mesh with 2 mm cell size was adequate.

Pressure-velocity coupling was solved with Coupled algorithm instead of SIMPLE algorithm since it can accelerate the convergence for steady-state problems (Tsukaguchi et al., 2007). The remaining solution parameters used were the same as those in previous chapters.

5.3 Experimental Validation

To validate the CFD method used, it was necessary to construct a suitable experimental apparatus. To achieve this, it was decided to use a custom designed rotationally molded polypropylene tank. Given the nature of the rotational molding method, there was 2° draft for the inner cylindrical wall tank which was not considered in the computational model, though it was assumed the effect of this would be relatively minor. As such, the inner cylinder of the experimental tank had the top and bottom diameters of 482 mm and 542 mm, and the vertical height of 860 mm with the capacity of 195.2 L. The dimensions of the outer cylinder were 610 mm x 1020 mm, resulting in an annular gap of 34 mm and a top coaxial gap of 160 mm. The bounding surfaces of the tank were made of 6 mm thick polypropylene material.

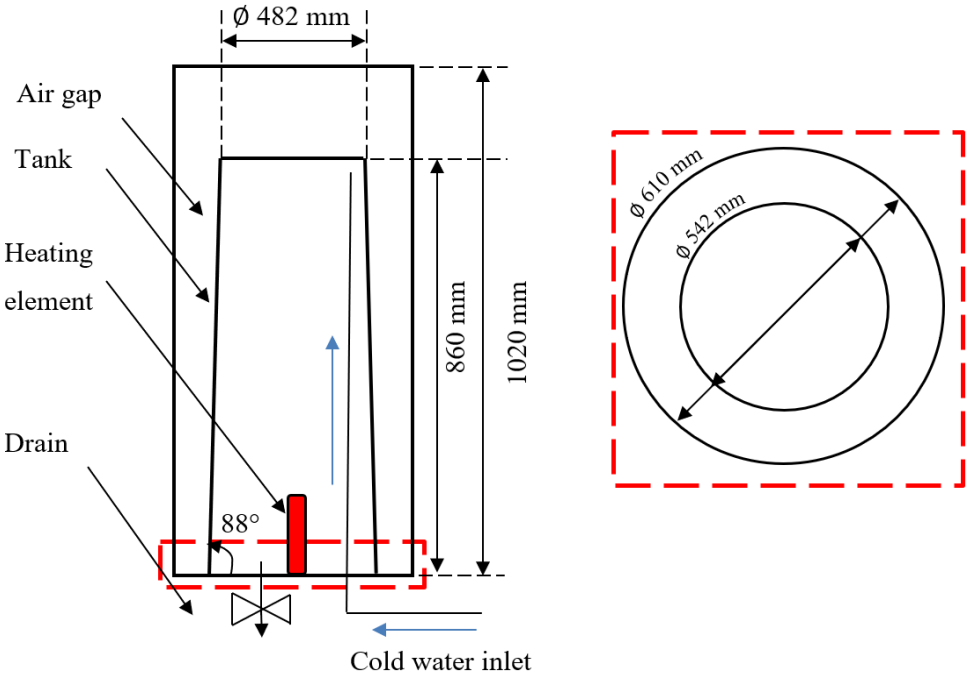

Figure 51: Layout of the experimental apparatus

To study the thermal processes of water under natural convection, the tank was initially filled with cold water. The tank was also equipped with an internal heating element to heat the water to the desired uniform temperature of 60°C. This condition is

within the range of hot water temperature a typical fully charged SDHW system on a sunny day after the entire volume of water gets heated. The tank was then allowed to lose heat to the surroundings to imitate the process of standby operation of solar water tanks during which static heat loss to the ambient takes place. The apparatus used in this study is illustrated in Figure 51.

To determine the temperature profile inside the tank, a series of thirteen copper-constantan (Type-T) thermocouples that were distributed along the height of the tank was used while a fourteenth thermocouple was used to measure the ambient temperature, as shown in Figure 52. The thermocouples were connected to two Picolog TC-08 data acquisition systems and temperature readings were recorded by a computer via USB interface.

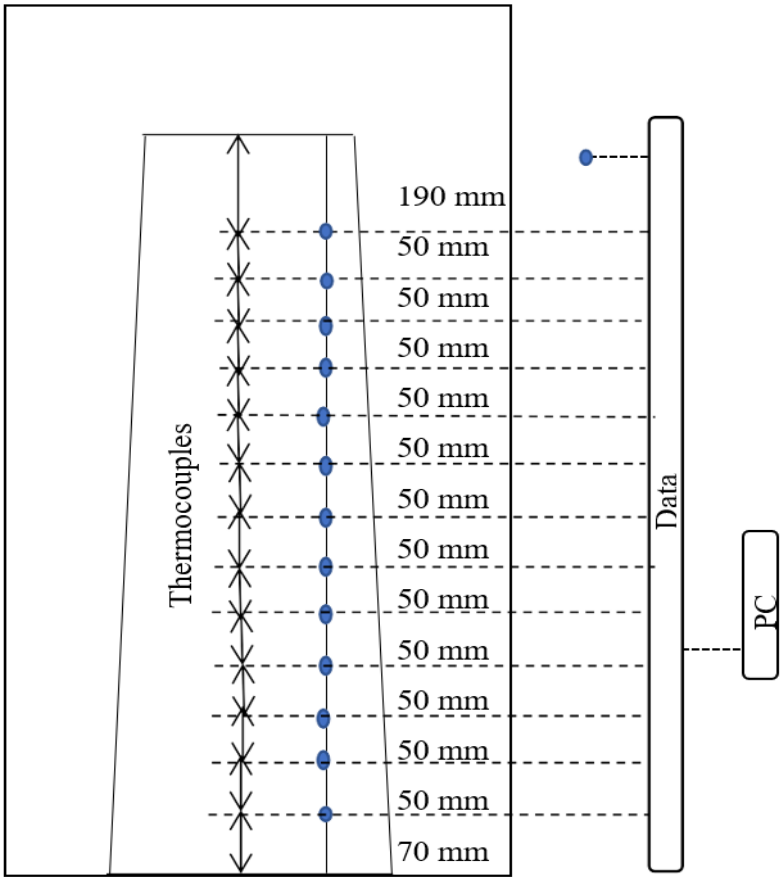

Figure 52: Schematic of experimental temperature measurement system

5.4 Results and Discussion

A CFD model with the same configuration and boundary conditions as that of the experimental tank was developed to validate the computation method used. Mesh and time sensitivity analysis related to the developed CFD model was provided in Appendix E.

Figure 53 shows the measured, and CFD predicted, temperatures in the tank over a 24-hour period. The measured temperatures show that after 1 hour, there has been a gradual decrease in temperature from 62°C to 57°C at the bottom of the tank. As the tank continues to cool down, the water temperature at the bottom decreases at a faster rate than the top. The maximum temperature difference between the top and bottom of the tank reaches 6°C, 24 h after the start of the experiment. This is because of the progressive development of thermal stratification at the bottom formed by the downward flow of cold water along the tank wall.

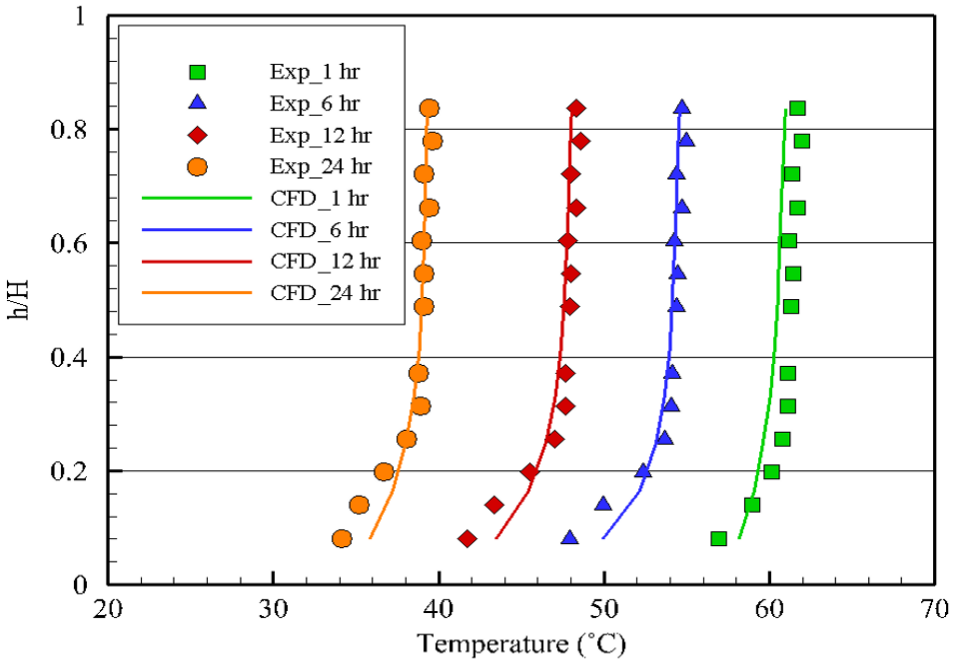

Figure 53: Temperature validation of air insulated CFD model for cool-down test

From these results, it is apparent that the temperature profile predicted by the CFD model is like that of the experiment. The same temperature trend has been observed between the two data sets (experiment and CFD) after 1 h to 24 h of cooling, with deviations up to 2°C between the CFD prediction and the experimental data near the bottom of the tank. The validation results were considered to be acceptable if the agreement between the experimental data and CFD data or empirical correlations is less than 15%. The minor differences are likely due to the thermal stratification of the air trapped inside the insulation while heating up the water before the experiment. This possible variation of air temperature with height inside the insulation is not considered in the CFD model. Another possible cause is due to the thermal stratification of the surrounding ambient air during the experiment, which was not taken into consideration in the CFD model.Knowing that a combination of convection and radiation heat transfer takes place inside the air gap, it was decided to examine the contribution of each heat transfer mechanism to overall rate of heat transfer across the air gap.

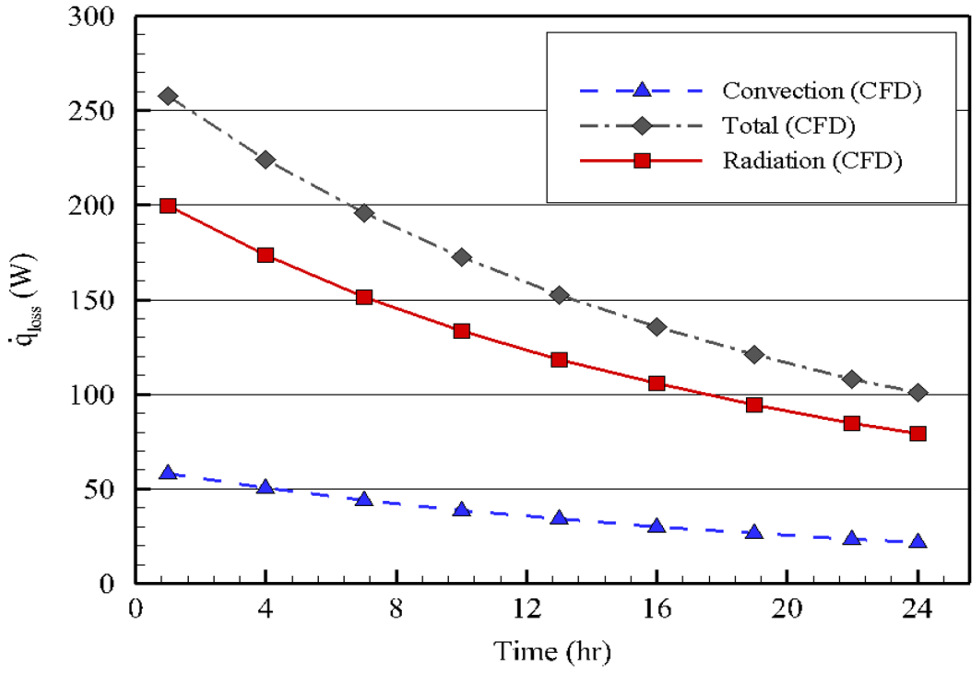

Figure 54: Contribution of convection and radiation heat transfer across the air gap

In Figure 54, it can be seen that radiation is the dominant mode of heat transfer and accounts for about 79% of the total heat loss through the air insulation while the remaining 21% of heat loss takes place via convection heat transfer.

Having observed this, it was decided to assess the suitability of using view factor-based method in predicting radiation heat transfer across the air gap. Figure 55 shows radiation heat loss through the air insulation predicted by CFD and radiation view factor-based calculation with an assumption of annular gap between infinitely long concentric cylinders, adopted from (Cengel, 2004), as shown in Equation (20) over the period of 24 hour cool down test.

$$\dot{q}_{rad} = \frac{A_{i,total}\sigma({T_{w1}}^4 - {T_{w2}}^4)}{\frac{1}{\epsilon_{w1}} + \frac{1-\epsilon_{w2}}{\epsilon_{w2}}\left(\frac{r_{w1}}{r_{w2}}\right)} \tag{20}$$

Where, total internal surface area of the inner wall, $A_{w1,total}$ can be defined, as shown in Equation (21).

$$A_{w1,total} = A_{w1,t} + A_{w1,s} \tag{21}$$

In Figure 55, it can be seen that radiation view factor-based method was able to satisfactorily predict the CFD results of radiation heat transfer rate within 5% error over the period of 24 hours cool down test. On the other hand, convection heat transfer, needs to be investigated in detail since it significantly varies with geometrical factors, such as aspect ratio and size of the air gap.

Therefore, the validated CFD model will be used to investigate the effect of aspect ratio, uniform gap sizes, and nonuniform gap sizes on convection heat transfer inside the air cavity was examined in detail. For uniform gaps, the size of the gap is uniform throughout the enclosure whereas for non-uniform gaps, top and side gaps are varied independently from each other.

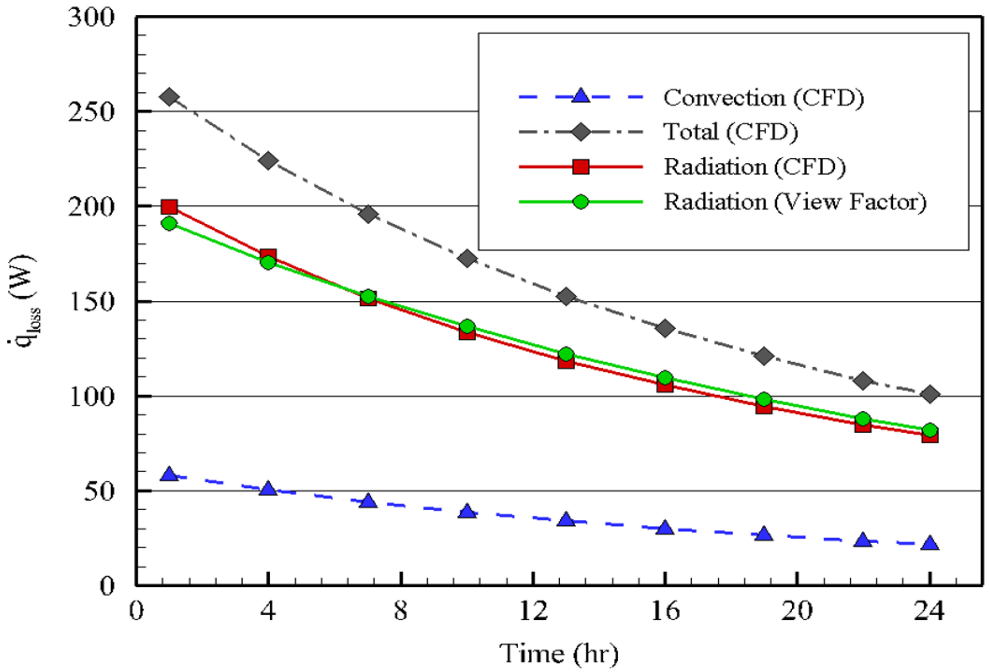

Figure 55: Rate of radiation heat transfer inside air insulation predicted by CFD model and radiation view factor-based calculation

5.4.1 Effect of gap size on heat loss

To understand the effect of uniform gaps on heat transfer inside the enclosure, various uniform gaps for a fixed aspect ratio of 3 were examined. Figure 56 shows streamline and temperature contour inside 10 mm air gap. Given the small space inside 10 mm gap, conduction-dominated heat transfer with constant heat flux for the most part of the side wall is seen with noticeably high thermal gradients at both ends of the wall, as indicated by symmetrical streamlines together with vertically aligned isotherms. On the other hand, most part of the top wall of the inner cylinder loses heat through conduction with weak convection near the right end, as evident from the presence of convective cells. In line with this, corresponding temperature contour also indicates the presence of horizontally aligned isotherms which characterizes the dominance of conduction heat transfer. The presence of these convective cells could be the result of convection induced by the flow in the adjacent side annular cavity near that region.

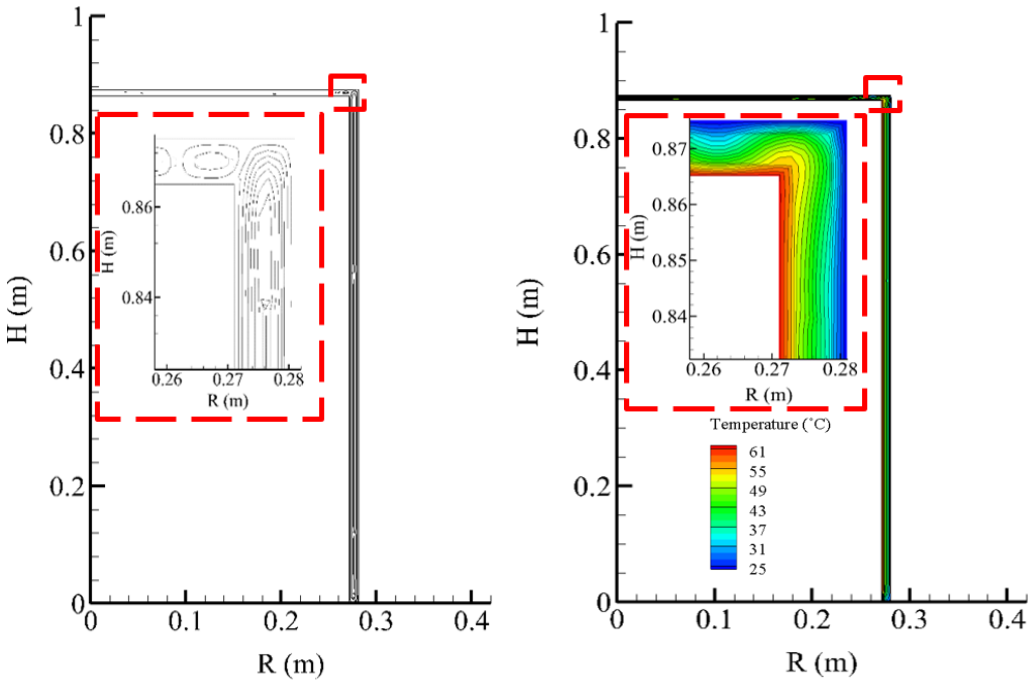

Figure 56: (a) Streamlines and (b) Temperature contour inside uniform air gap of 0.01 m

As the gap becomes wider to 30 mm, a marked increase in convection heat transfer inside the side annular cavity was noted, as reflected by the asymmetrical streamlines in the cavity in Figure 57. This is because the recirculation flow inside the side annular cavity became stronger, leading to more efficient rejection of heat from hot to cold wall. The increase in convection in the side annular gap can also be witnessed from isotherms, which become vertically misaligned, and turn sharply into opposing thermal boundary layers on each side wall. Increasing the top coaxial gap allows heat to be carried from the hot to cold wall through weak convection heat transfer governed by multiple convective (Bénard) cells. Despite this, heat flux on the top wall decreases compared to 10 mm gap because this phenomenon is still weak compared to the more dominant conduction heat transfer.

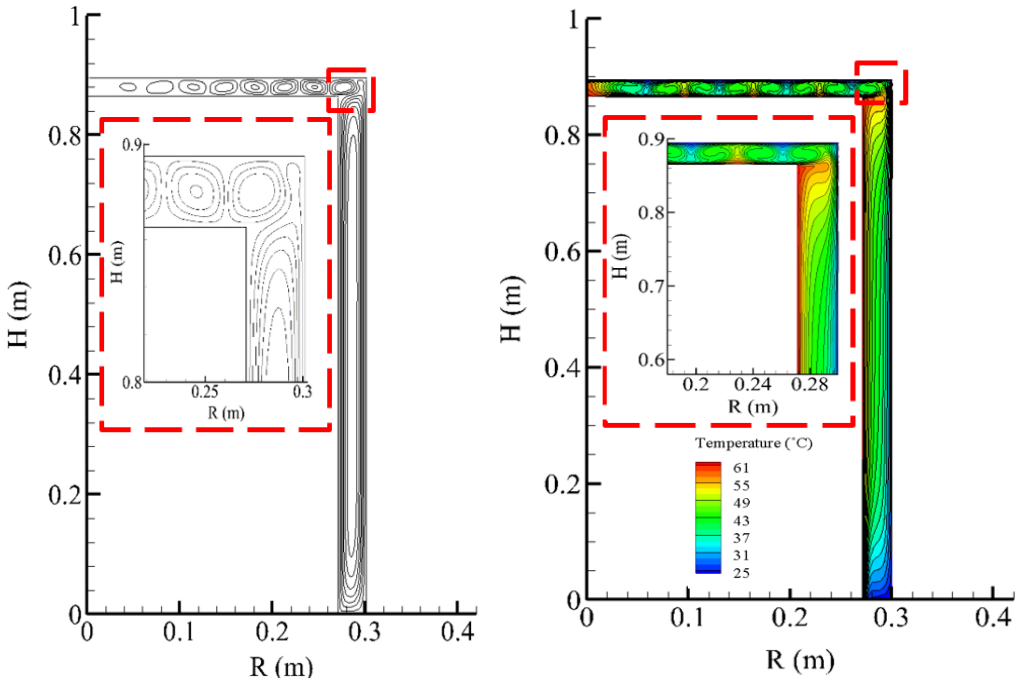

(a) (b)

Figure 57: (a) Streamlines and (b) Temperature contour inside uniform air gap of 0.03 m

With a 100 mm air gap, convection heat transfer becomes more pronounced, as reflected by crowded streamlines near the region of the walls which represents high flow velocities in Figure 58. This recirculation flow inside the side annular cavity became significantly stronger, as can be seen from nearly horizontal isotherms. This is due to an increase in intensity of the opposing boundary layer flows on both side walls. It is also worth noting that air in the region, where top and side wall of the inner cylinder meets, was trapped between the flows in each cavity and remained quiescent. This could potentially retain heat near that region.

A further increase in top coaxial gap 100 mm results in higher convection heat transfer through the formation of a single convective cell at higher velocity than 30 mm gap. However, heat flux on the top wall decreases due to the disappearance of multiple convective cells, which are more efficient at transferring heat from the hot to cold wall

bounding the top cavity.

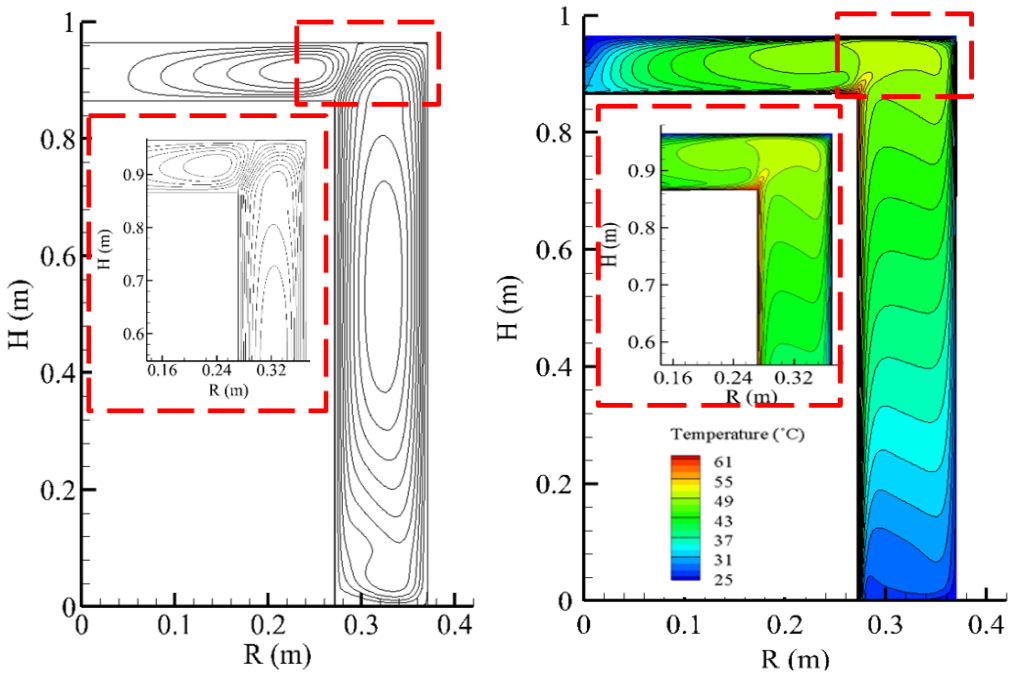

Figure 58: (a) Streamlines and (b) Temperature contour inside uniform air gap of 0.1 m

Having observed the flow behavior of different uniform air gaps, it was decided to examine average heat flux on top and side walls of the inner cylinder, as shown in Figure 59. From Figure 59(a), it can be seen that heat flux on the side wall decreases from 10 mm to 30 mm due to shifting of conduction to weak convection heat transfer inside the side annular gap. However, widening the gap further to 100 mm markedly increases convection heat transfer, resulting in higher heat flux compared to 30 mm gap.

A further increase to 100 mm gap reduces heat flux due to the disappearance of rotating cells. This is associated with persistent horizontal movement of fluid from left to right along the bottom hot wall, which becomes intensified with increasing cavity height and leads to the destruction of multicellular flow, as shown in Figure 59(b). Similar flow patterns were reported in the experimental work of Goldstein (1969) on turbulent convection in horizontal layer of air heated from below. This horizontal

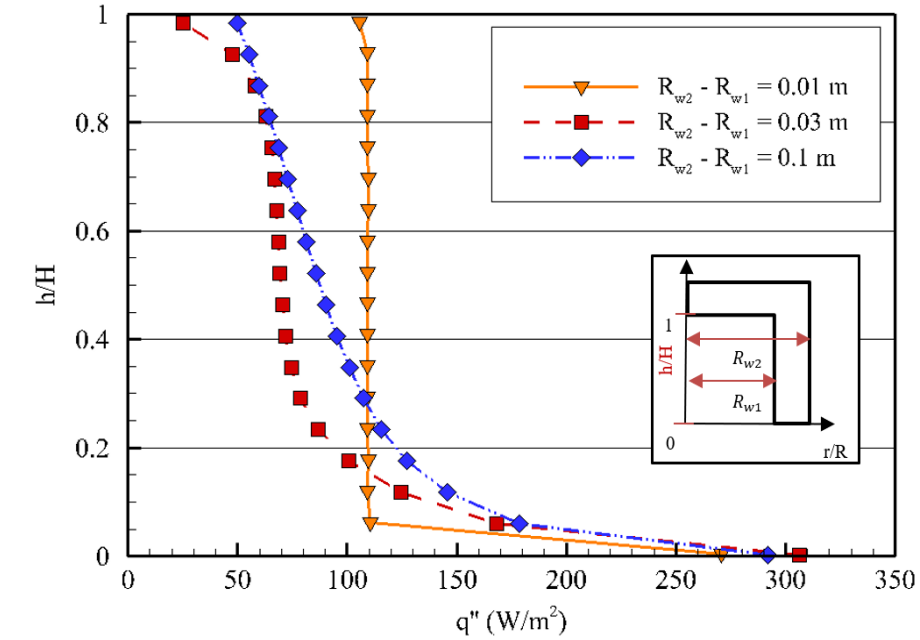

(a)

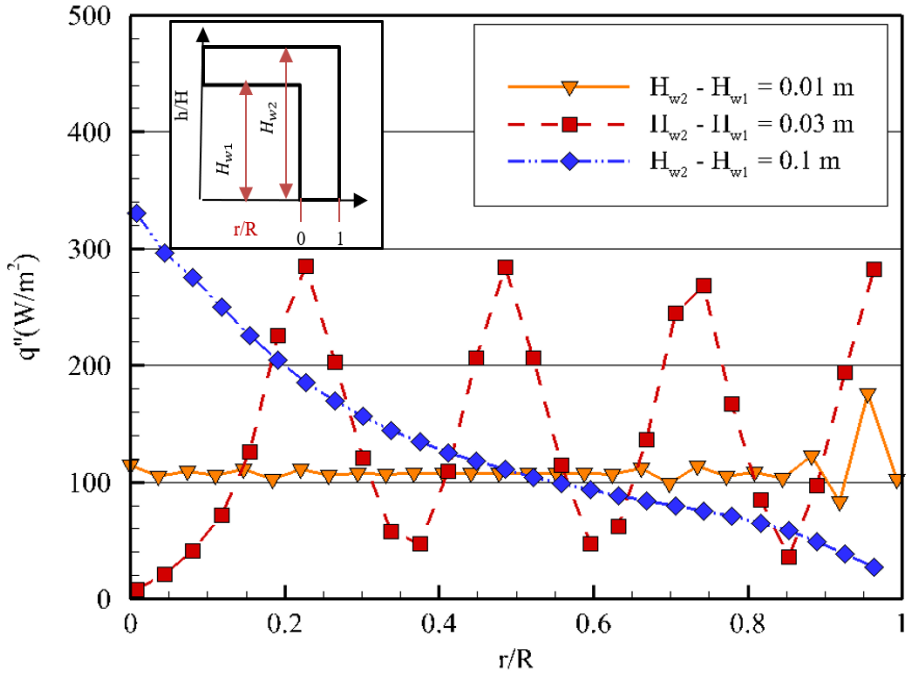

(b)

Figure 59: Local heat flux at (a) side wall and (b) top wall of the inner hot cylinder

movement of air results in a decrease in heat flux as the air carries the heat away from the wall and progresses towards the right end. It is also worth noting that heat flux on

the right end of the top wall was unusually low due to the air trapped between the flows inside each cavity.

As the heat transfer mechanism changes from conduction to convection with increasing uniform air gap sizes, 30 mm gap exhibits lowest overall heat flux which translates to the lowest rate of heat loss since the total surface area of the inner cylinder is kept constant in all the cases considered, as indicated in Figure 60. This observation is similar to the findings of Batchelor (1954) who reported that there is an optimum distance between differentially heat walls of any rectangular cavity with minimum heat transfer coefficient or heat flux due to transition from conduction to convection heat transfer.

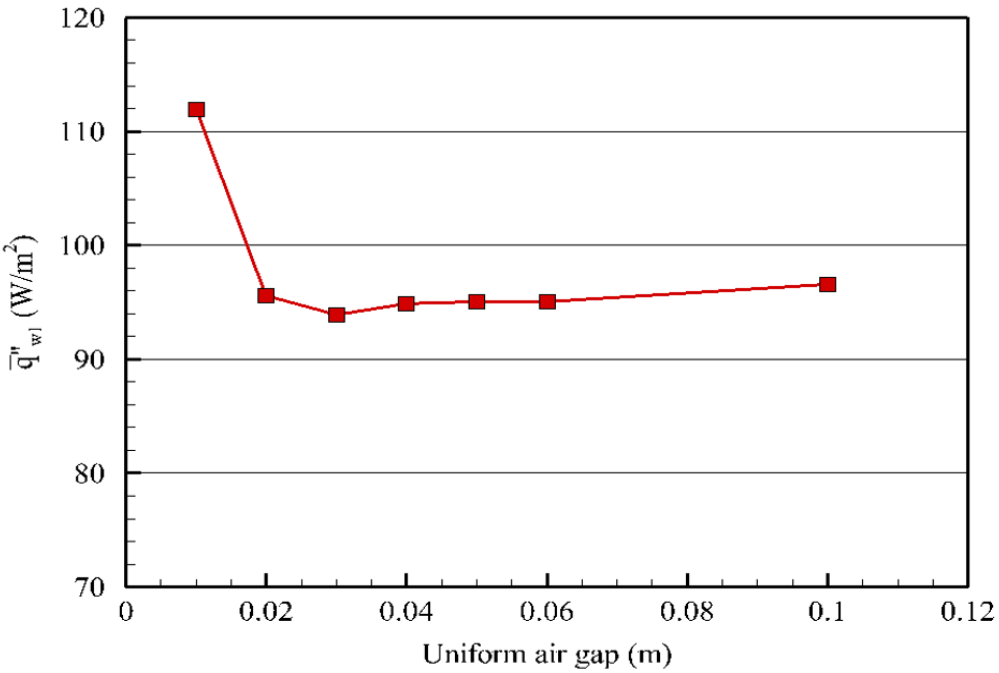

Figure 60: Change of overall heat flux of the inner hot cylinder with uniform gap sizes

Figure 61 shows the effect of varying sizes of top gaps on heat flux for fixed side gaps of 30 mm, 60 mm and 100 mm. It is observed that heat flux decreases as the size of the top cavity increases. In view of understanding changes in overall heat flux for different non-uniform gaps, local heat flux distributions on side and top walls of the

inner hot cylinder are discussed below.

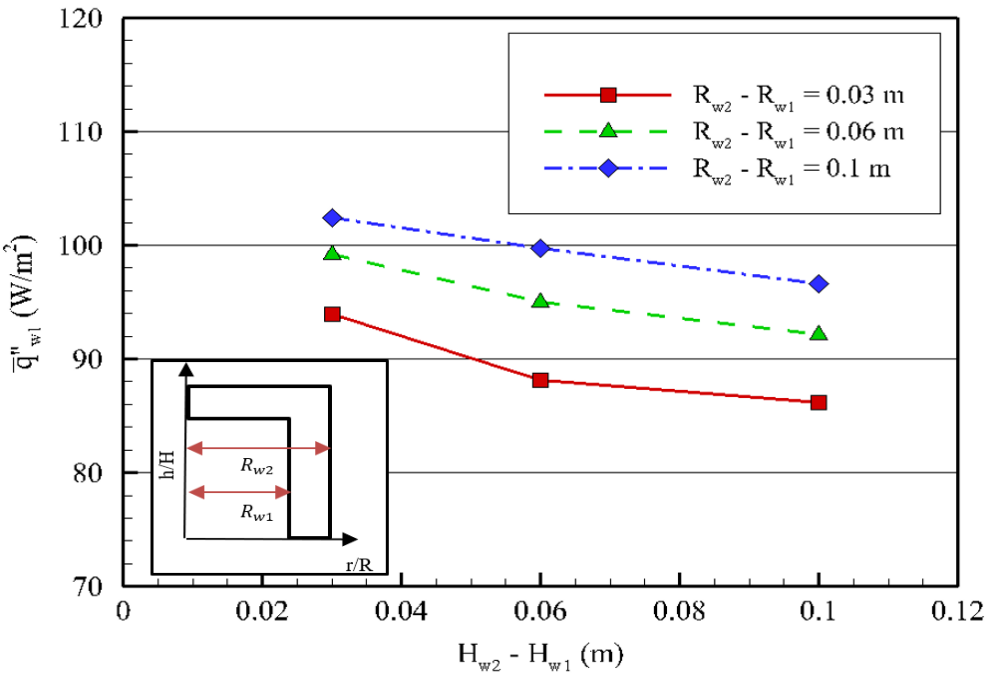

Figure 61: The effect of various top gaps on heat flux of the inner cylinder

5.4.2 Effect of aspect ratio on heat loss

To analyze the effect of aspect ratio on heat loss from inner cylinder, CFD cases were simulated different aspect ratios of the inner cylinder varying from 1.7 to 5.9 for fixed uniform gaps of 30 mm, 60 mm and 100 mm.

Figure 62 shows temperature contour inside 30 mm air gap for different aspect ratios. From the figure 62, it is evident that changing the aspect ratios alters the flow behavior in the region intersecting the side and top cavities. Hot air near the top of the side wall is carried away towards the outer wall of the top cavity in addition to adjacent side wall by convective cell that occupies that region. This convective cell becomes stronger with increasing aspect ratio, leading to a sharp increase in heat flux near the right end of the inner top wall, as shown in Figure 63 (b). As a result, the ability of hot air to reach the cold side wall is reduced. This results in less cold air impinging on the

bottom of the hot side wall. This leads to a reduction in heat flux near the bottom of the hot side wall, as indicated in Figure 63 (a).

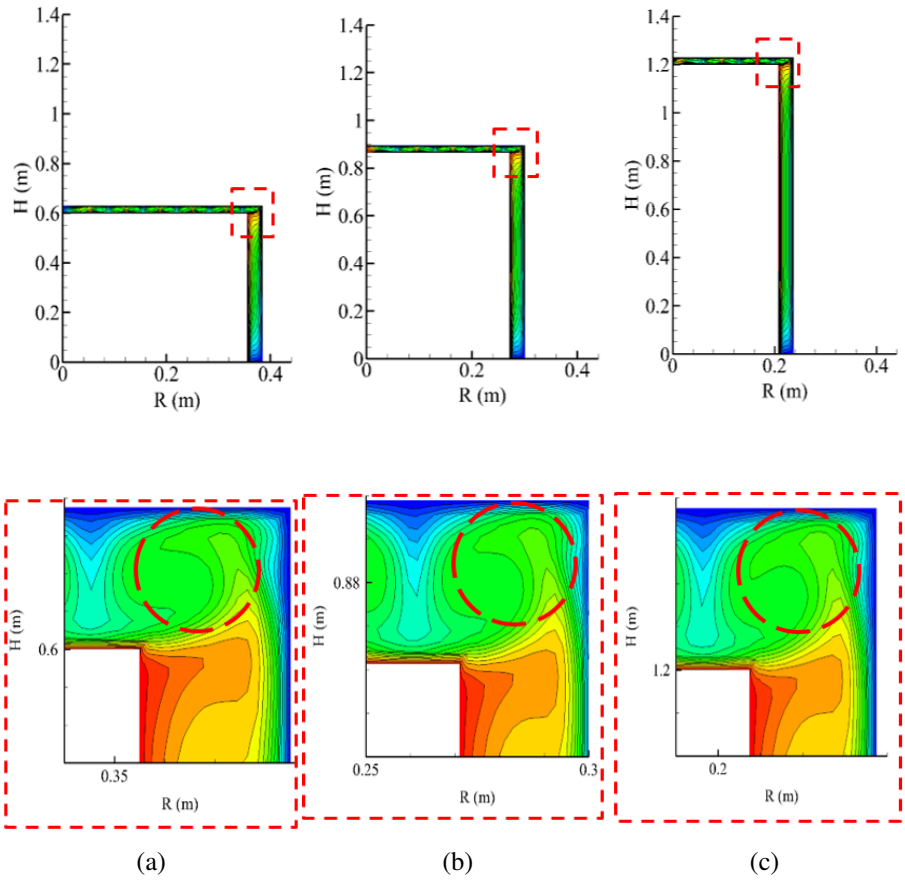

Figure 62: Isotherms of uniform enclosure with 30 mm gap for aspect ratios of (a) AR = 1.7, (b) AR = 3 and (c) AR = 5.9

However, this phenomenon becomes less pronounced with increasing air gap sizes, as indicated by disappearance of convective cell due to the dominance of flow in the side cavity, which progressively occupies the region of intersection between the two cavities, as shown in Figure 64 and 65.

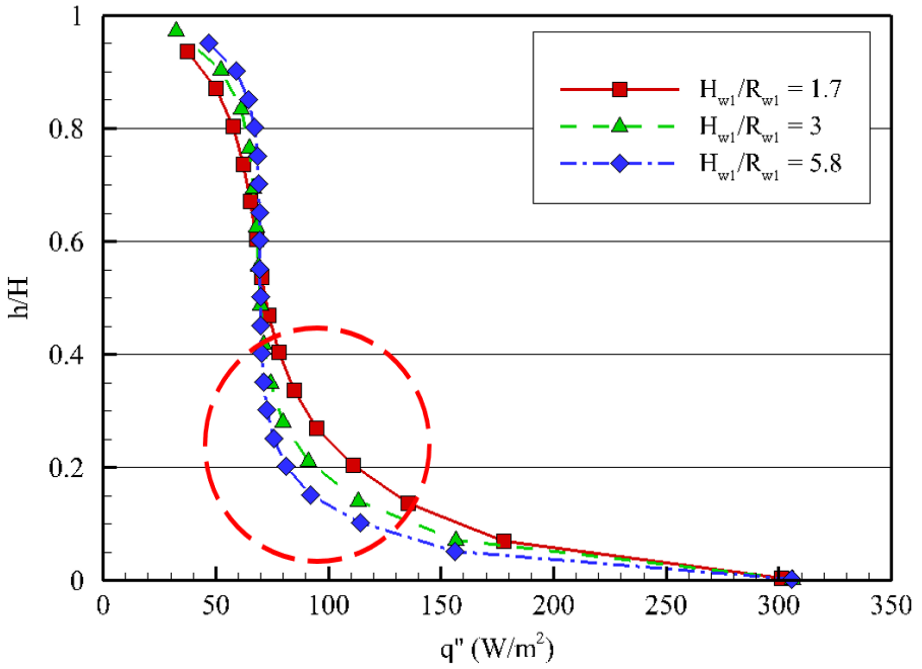

(a)

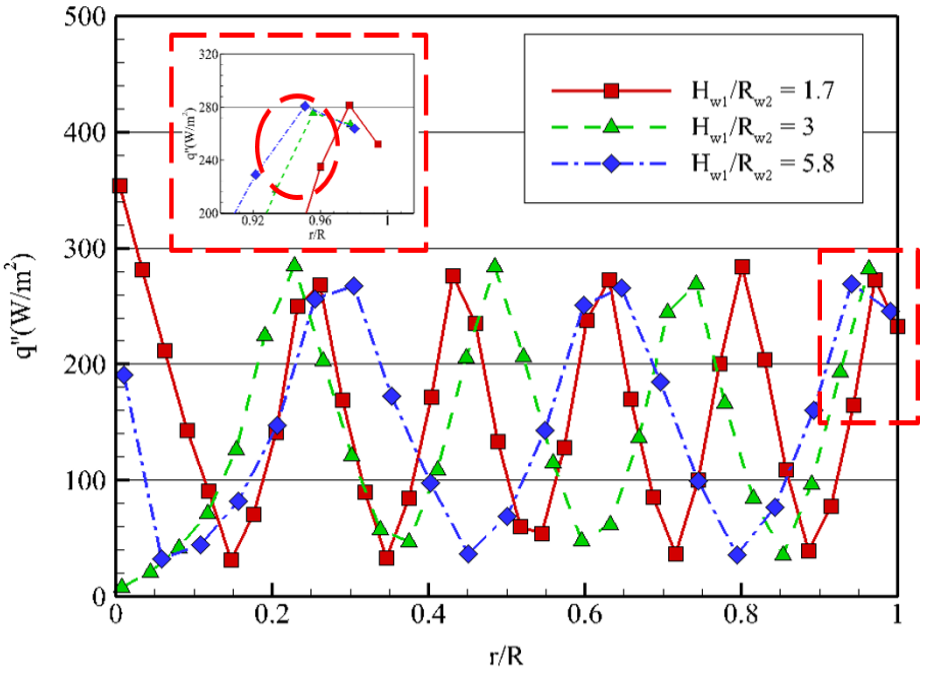

(b)

Figure 63: Distribution of heat flux on the inner hot (a) side wall and (b) top wall of cavity with gap size of 30 mm for various aspect ratios

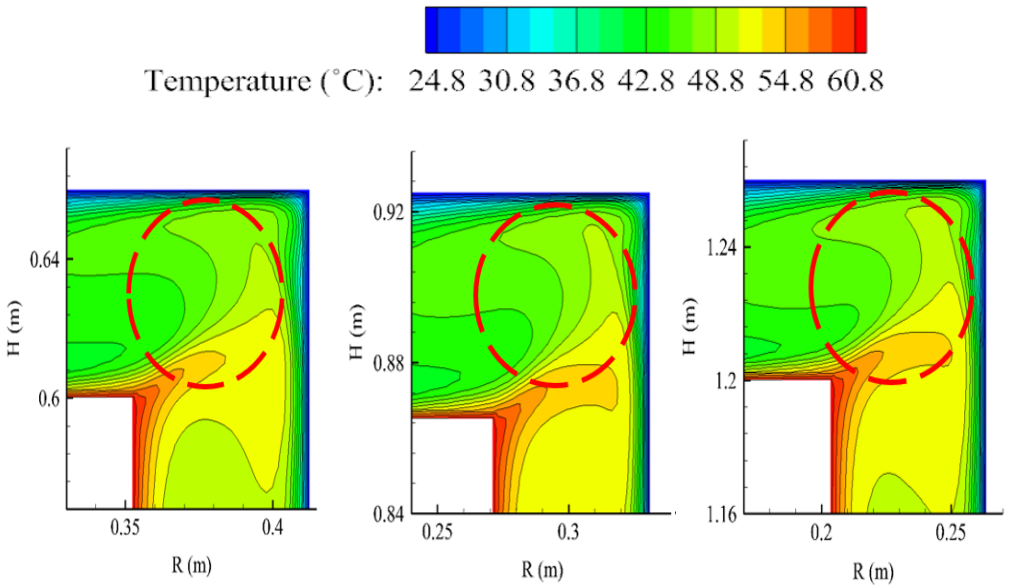

(a) (b) (c)

Figure 64: Isotherms of uniform enclosure with 60 mm gap for aspect ratios of (a) AR = 1.7, (b) AR = 3 and (c) AR = 5.9

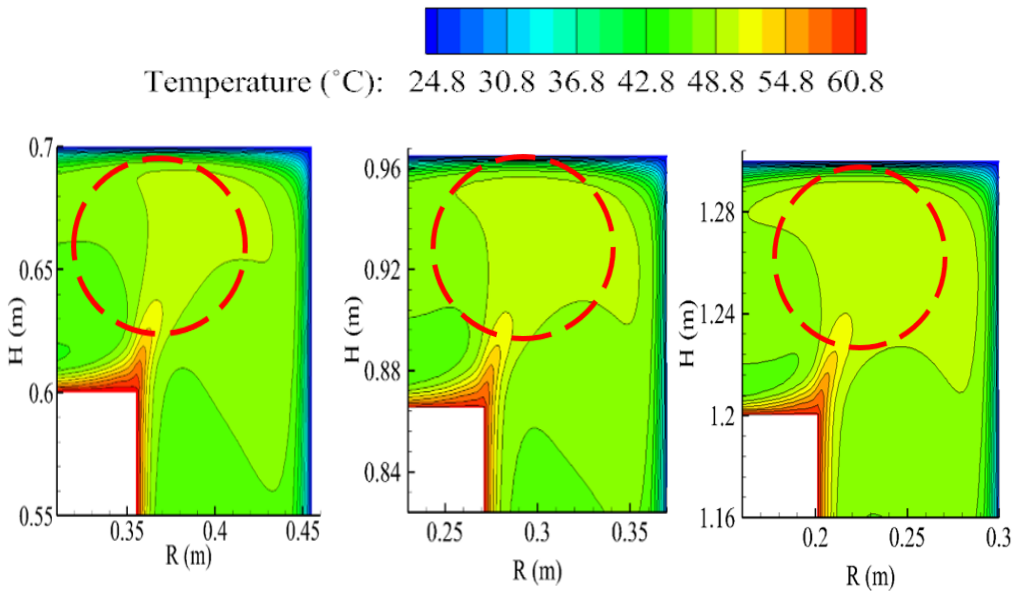

(a) (b) (c)

Figure 65: Isotherms of uniform enclosure with 100 mm gap for aspect ratios of (a) AR = 1.7, (b) AR = 3 and (c) AR = 5.9

Having observed the flow behavior of uniform air gaps with different aspect ratios, it was decided to examine the overall heat flux on the inner cylinder, as shown in Figure 66.

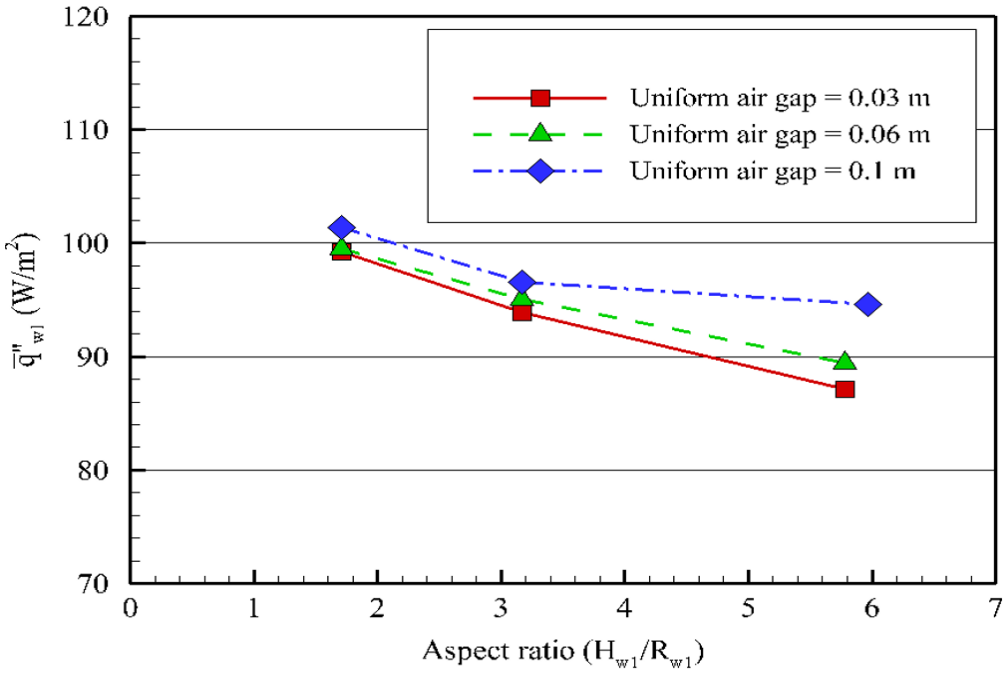

Figure 66: Total change in overall heat flux on the inner cylinder for varying aspect ratios with gap sizes of 30mm, 60mm and 100 mm

From Figure 66, it is evident that the heat flux on the inner cylinder decreases with increasing aspect ratios. For the same aspect ratio, widening the gap increases the overall heat flux due to the increasing strength of convection in the side cavity. The rate at which the heat fluxes reduce becomes lower with increasing gap sizes. This is associated with flow behavior in the region intersecting the side and top cavities with changing aspect ratios, as discussed in the previous section. This observation is similar to the findings of Davis and Thomas (1969) who reported that convection heat transfer decreases with increasing aspect ratios of a stand-alone annular cavity for a fixed gap size.

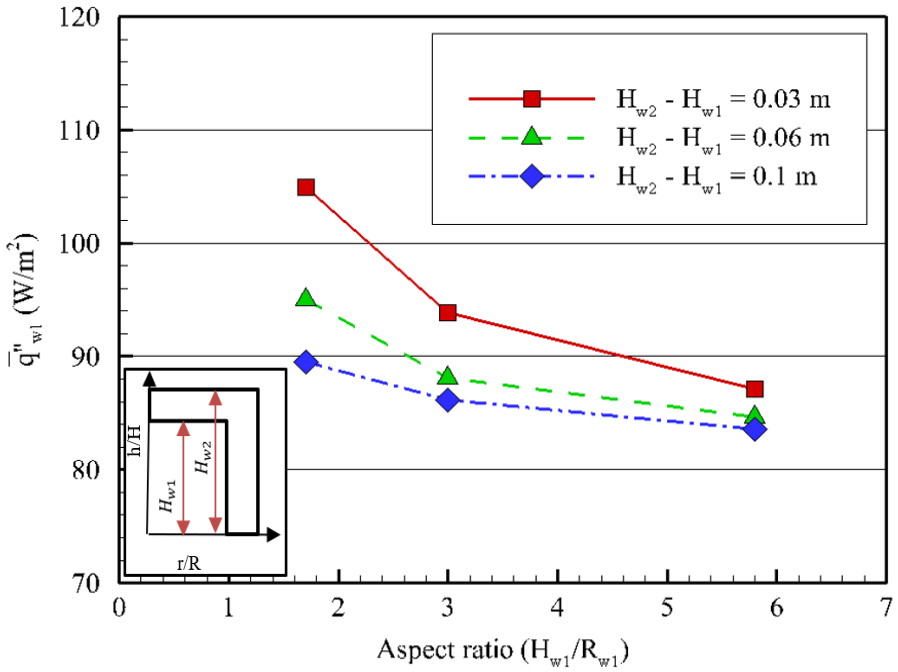

(a)

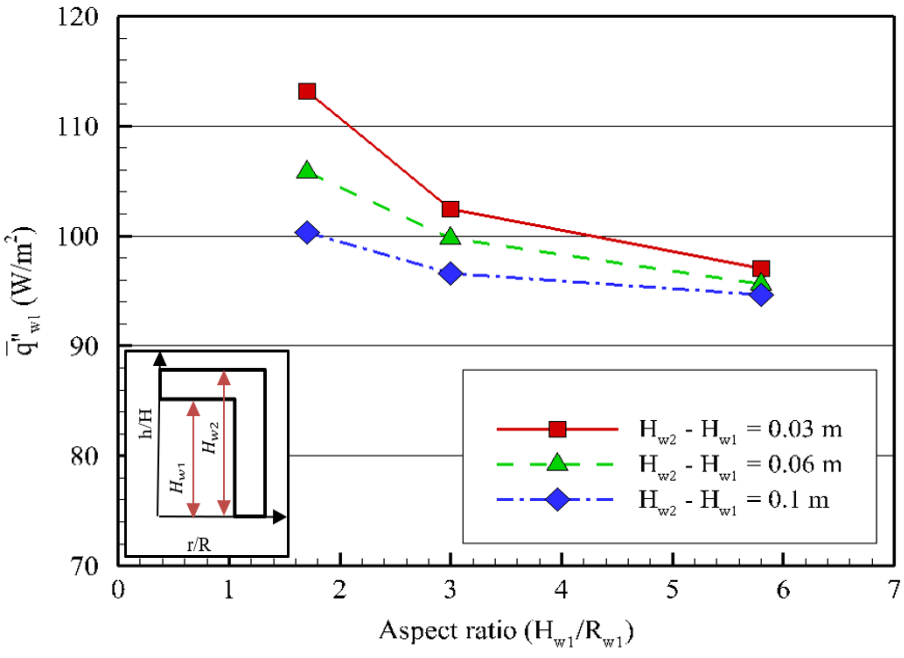

(b)

Figure 67: The effect of different aspect ratios on heat flux of the inner cylinder inside non-uniform enclosures having various top gaps with fixed side gaps of (a) 30 mm, (b) 100 mm

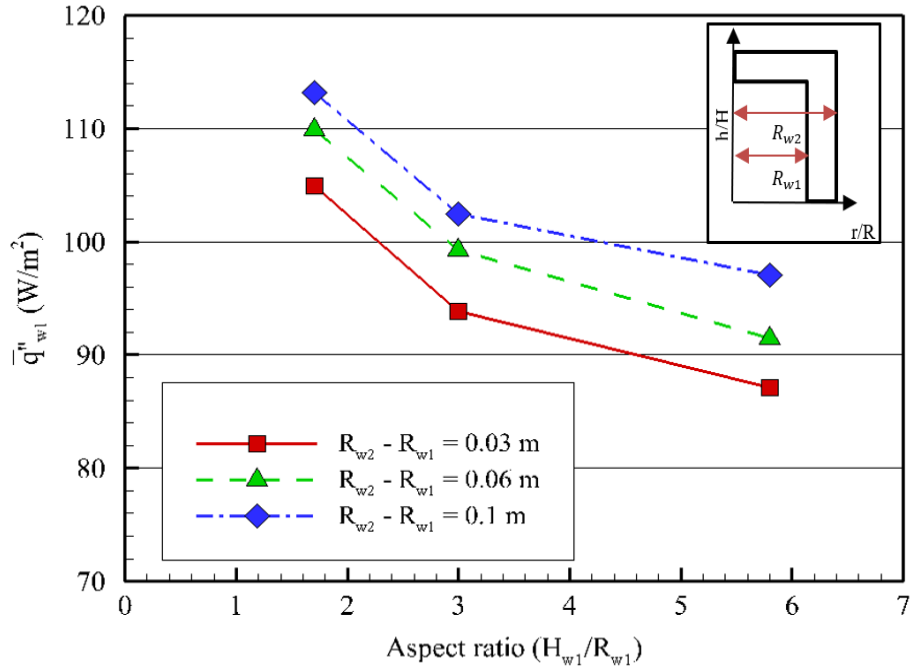

(a)

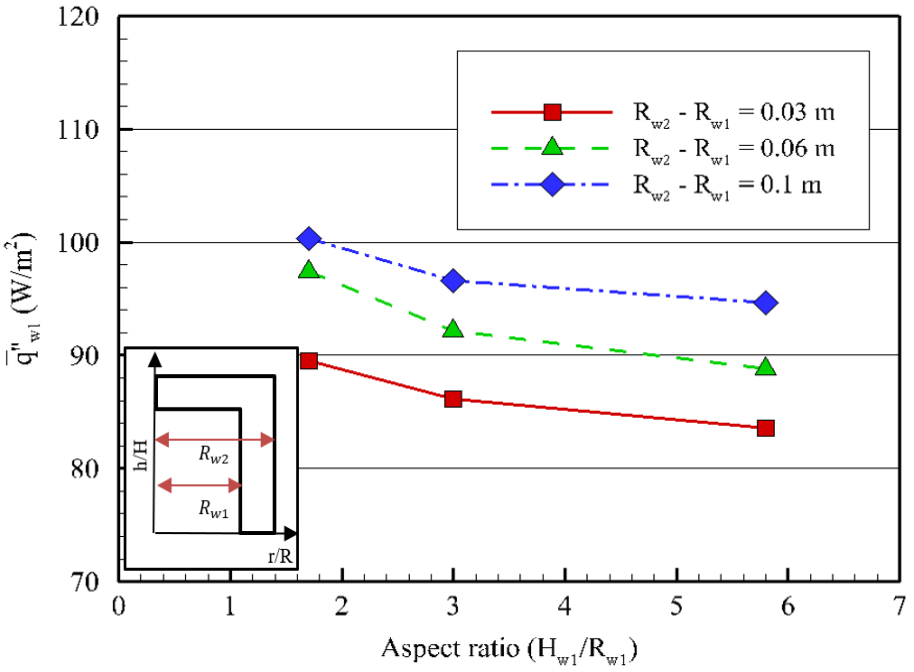

(b)

Figure 68: The effect of different aspect ratios on heat flux of the inner cylinder inside non-uniform enclosures having various side gaps with fixed top gaps of (a) 30 mm, (b) 60 mm and (c) 100 mm

To analyze the effect of aspect ratio on heat loss from inner cylinder, CFD cases were simulated different aspect ratios of the inner cylinder varying from 1.7 to 5.9 for non-uniform gap sizes of 30 mm and 100 mm. Figure 67 shows the effect of different aspect ratios on heat transfer inside enclosures with fixed side gaps of 30 mm and 100 mm for varying top gaps. Similar to the case of uniform enclosures, increasing the aspect ratio of the inner cylinder decreases heat loss inside the enclosure. This decrease in heat flux with increasing top gaps can be attributed to the disappearance of multiple convective cells.

Figure 68 shows the effect of different aspect ratios on heat transfer in enclosures with fixed top gaps of 30 mm and 100 mm for varying side gaps. Increasing the aspect ratio of the inner cylinder decreases heat loss inside the enclosure although the increase becomes less pronounced as the size of the top gap widens from 30 to 100 mm.

5.5 Development of correlation for convective heat transfer coefficient inside air gap insulation

In the previous section, the effect of varying air gap sizes and aspect ratio on convective heat transfer and subsequently, the rate of heat loss per unit area from the inner wall has been discussed. Knowing that the ability to predict heat loss through the current air insulation geometry is extremely important for design purposes, it was decided to develop an equation for convective heat transfer coefficient so that the rate of heat loss can be predicted.

To obtain a correlation of convective heat transfer coefficient that can be readily translated to enclosures of a different size, the following non-dimensional parameters that governs the natural convective heat transfer in the space between two concentric cylinders or two coaxial disks need to be introduced.

Given that the rate of heat loss from the inner cylindrical wall of the air gap is equal to the rate of heat gain by the outer cylindrical wall of the air gap, it was decided to define Nusselt number based on the convective heat transfer coefficient on the inner cylindrical wall, h_{w1} as shown in Equation (22).

$$\bar{Nu} = \frac{\bar{h}_{w1} L_c}{k_{air}} \tag{22}$$

The Rayleigh number for natural convection inside the air gap was defined based on the temperature difference between the two walls bounding the air gap, as indicated in Equation (23).

$$Ra_A = \frac{g\beta_{air}(\bar{T}_{w1} - \bar{T}_{w2}){L_c}^3}{\upsilon_{air}\alpha_{air}} \tag{23}$$

Based on the current insulation geometry, the characteristic length, L_c is defined in Equation (24).

$$L_c = \frac{H_{w1}}{H_{w2}}(R_{w2} - R_{w1}) + \frac{R_{w1}}{R_{w2}}(H_{w2} - H_{w1}) \tag{24}$$

This characteristic length was chosen because it takes variation of gaps in both top circular and side annular cavities into account. Both Rayleigh number and aspect ratio are included in the correlation to account for changes in the geometry of the air insulation cavity.

After defining the non-dimensional parameters, the results of convective heat transfer coefficients obtained from the simulation are fitted through multiple nonlinear regression and correlated, as shown in Equation (25).

$$\bar{Nu} = c\, Ra^m\, (\frac{H_{w1}}{R_{w1}})^n \tag{25}$$

Based on the results, the fitted coefficients were shown to be c = 0.066, m = 0.343 and n = -0.082. The proposed Nusselt correlation is shown in Equation (26). Different coefficients of c, n and m may be needed for enclosures exceeding the limit of 1.52 × 10^4< Ra_A < 8.97× 10^6 and 1.7 < AR < 5.8.

$$\bar{Nu} = 0.066\, {Ra_A}^{0.343}\, (\frac{H_{w1}}{R_{w1}})^{-0.082} \tag{26}$$

The goodness of fit for the proposed correlation is illustrated in Figure 69. As can be seen from Figure 69, the proposed Nusselt correlation shows a good agreement with all the simulated data set, with a goodness of fit of R^2 = 0.998.

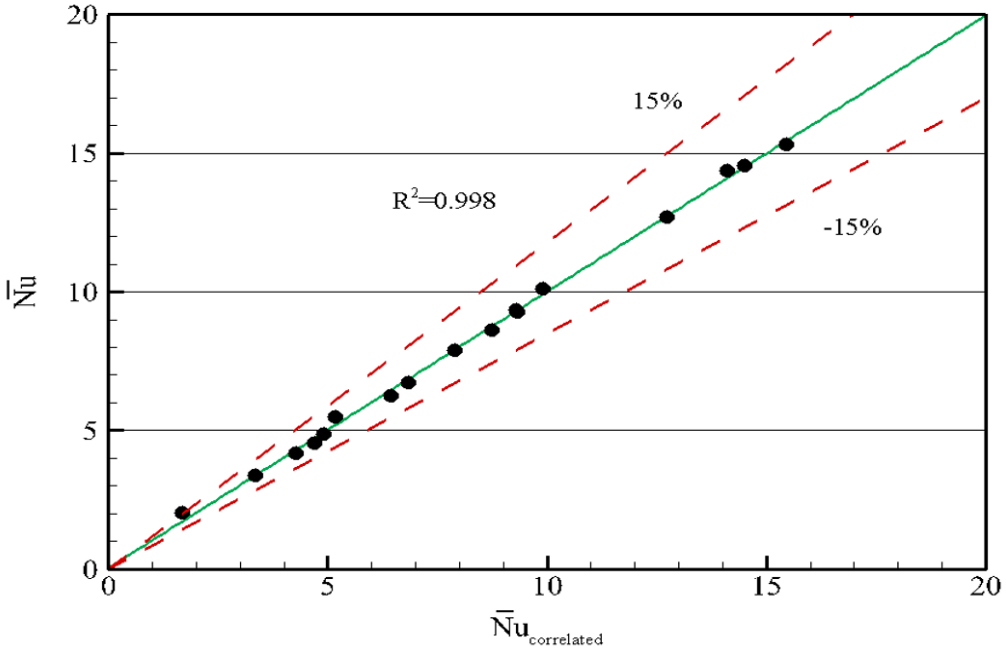

Figure 69: Correlation of convective heat transfer coefficient inside the inverted U-shaped air insulation cavity indicating simulated data against fitted correlation of Nusselt number

5.6 Conclusions

This chapter examines a simple inverted U-shaped air insulation that can provide a similar insulation performance to that of ordinarily used insulation materials.

The analysis on effect of geometrical factors of air cavity on the rate of convective heat transfer shows that as the air gap increases, the dominant heat transfer mechanism also transitions from conduction to convection heat transfer. As a result, the optimum air gap with minimum heat flux was shown to be 3 cm within the range of investigated gap sizes between 1 and 10 cm. It was also shown that increasing the aspect ratio of inner cylinder (i.e. storage tank) alters the flow behavior in the region intersecting the side and top cavities. Because of this, convective heat transfer decreases as the aspect ratio increases.

Based on the findings, a generalized correlation that fully describes the variation of convective heat transfer coefficient with geometrical factors inside the investigated air gap insulation. The proposed Nusselt number correlation will be useful in designing such cylindrical solar storage tanks encapsulated inside an inverted U-shaped air insulation that can provide similar thermal performance to that of ordinarily insulated tanks.

Chapter 6

Long term thermal performance of a solar storage tank

6.1 Introduction

In the preceding chapters, it was shown that passive baffle inside the tank and air gap insulation around the tank can reduce heat loss from storage tanks to a certain extent. However, the improvements in thermal performance provided by baffle jacket and air gap insulation were only seen for the limited boundary conditions of numerical simulations. Similarly, the influence of tank aspect ratio on heat loss for storage tanks with and without baffle jacket, and tanks additionally insulated with air gap was only investigated for the standby period of solar water heater.

Considering this, this chapter aims to understand the long-term performance of solar water storage tanks as a function of geometric variables using the correlations developed in this thesis.

6.2 Mathematical model of a solar water heating system

This section details the development of mathematical modeling of solar water heating system to conduct simulations for the full cycle of solar water heater operation (charging, discharging and standby periods) using the new correlations developed from this work. The solar thermal storage system considered in this chapter consists of a solar collector and a storage tank as shown in Figure 70.

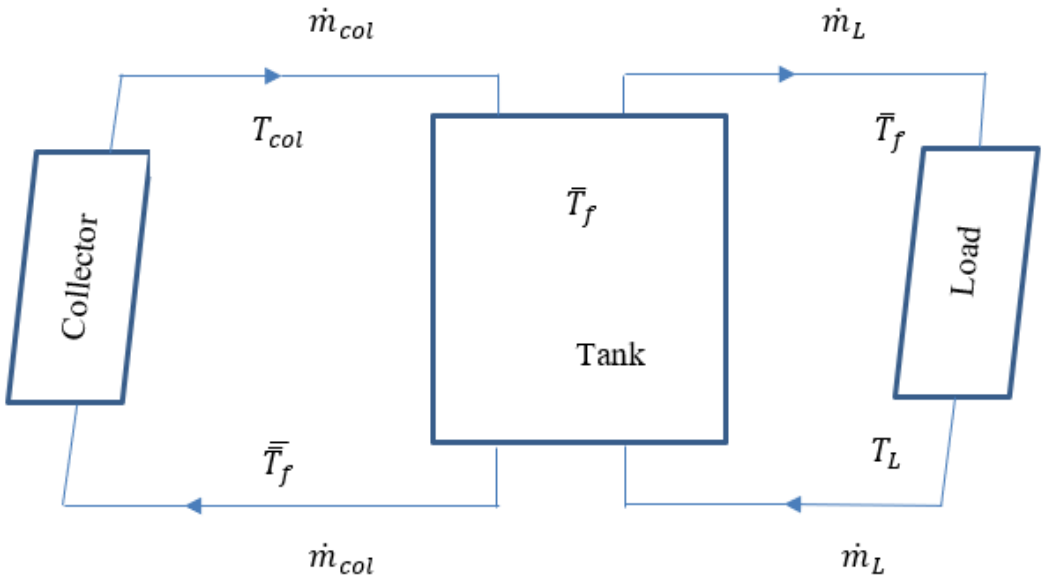

Figure 70: A typical solar thermal energy storage system

Mathematical modelling of this solar water heating system was developed using MATLAB and for the simulation, it was decided to examine a small-scale solar water heating system suitable for a single residence. As a result, a single-glazed flat plate collector of 4 m^2 mounted at 30° was selected to provide energy for 200 L storage tank. The resulting model was solved using Runge-Kutta 4th order method and the solver time step was chosen to be 10s by considering the computational effort since using a smaller time step did not lead to significant variation of results.

Typical meteorological year (TMY) data for Auckland was obtained from METEONORM software and consists of solar radiation, wind velocity and ambient temperature. Furthermore, a typical water use profile of Australian or New Zealand residence based on AS 4234:1994 was chosen to model the discharge operation, as shown in Figure 71 . The solar collector was modelled as a theoretical flat plate collector which is based on the modified Hottel-Whillier equations. A mixed hot water storage tank is considered instead of stratified tank with nodes because the aim of the study is to assess the long-term storage tank efficiency rather than analyzing the varying degree of thermal stratification inside the tank.

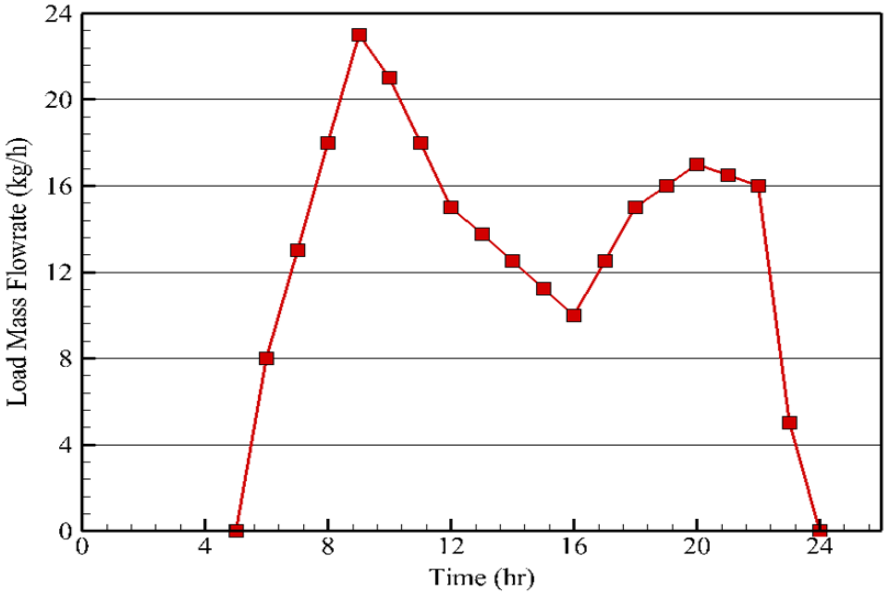

Figure 71: A typical hot water use profile (AS 4234:1994)

6.2.1 Solar collector model

It is evident from Figure 70 that the solar collector needs to be modelled as part of the solar water heating system to assess the long-term performance of the system. For this study, it was assumed that the collector could be represented as a flat plate thermal collector. As such, a one-dimensional steady state model based on the Hottel-Whillier-Bliss equations adopted from Duffie et al. (2020) was used, as shown in Equation (27).

$$\dot{q}_{useful} = A_{col} F_R [(\tau\alpha)_T G - U_L (T_{in} - T_{env})] \tag{27}$$

In this equation, the useful heat gain ($\dot{q}_{useful}$) is the function of the collector area A_{col}, the heat removal efficiency factor (F_R), the transmittance-absorptance product of thermal solar collector $(\tau\alpha)_T$, the solar radiation (G), the collector heat loss coefficient (U_L) and the temperature difference between the inlet water temperature (T_{in}) and the ambient temperature (T_{env}).

Given that transmittance-absorptance product of thermal solar collector $(\tau\alpha)_T$ are dependent on the collector design, it was assumed to be constant values of 0.8 to simplify the solar collector model.

The heat removal efficiency factor (F_R) was calculated using Equation (28) which also takes the collector mass flow rate ($\dot{m}_{col}$) and the specific heat capacity of water flowing through the collector ($c_{p,in}$).

$$F_R = \frac{\dot{m}_{col} c_{p,in}}{A_{col} U_L [1 - e^{-\frac{A_{col} U_L F'}{\dot{m}_{col} c_{p,in}}}]} \tag{28}$$

Although the collector fin efficiency (F') is a function of the collector heat loss is a function of the collector heat loss coefficient (U_L) and convective heat transfer coefficient inside collector tubes, it was assumed to be a constant value of 0.7 because

both parameters exhibits some temperature dependence but is a weak function of temperature, as discussed in Duffie et al. (2020). The collector mass flow rate ($\dot{m}_{col}$) was assumed to be 0.0278 kg/s which is within a typical range of solar water heating system. The specific heat capacity of water flowing through the collector ($c_{p,in}$) was determined using the temperature average between the collector and the tank at a given time step.

The overall heat loss coefficient U_L of the collector is the sum of the collector's edge, top and rear surface heat losses. Heat loss coefficients on the edge U_{edge} and rear U_{rear} surface of the collector can be calculated using Equation 29 and 30.

$$U_{edge} = \frac{k_{ins,col} P_{col} L_{abs}}{L_{ins,col} A} \tag{29}$$

$$U_b = \frac{k_{ins,col}}{L_{ins,col,b}} \tag{30}$$

Given that the glazed collector is exposed to the ambient, it is largely influenced by the velocity of the wind and thus, the top loss coefficient could be calculated using Klein's empirical as cited in Duffie et al. (2020) (see Equation 31).

$$U_{top} = \left[\frac{N}{\frac{c}{T_p}\left(\frac{T_p - T_a}{N-f}\right)^e} + \frac{1}{h_w}\right]^{-1} + \frac{\sigma(T_p + T_a)({T_p}^2 + {T_a}^2)}{(\epsilon_p + 0.00591 N h_w) + \frac{2N+f-1+0.133\epsilon_p}{\epsilon_g} - N} \tag{31}$$

Where

$$c = (520 - 0.000051\theta^2)$$

$$f = (1 + 0.089 h_w - 0.1166 h_w \epsilon_p)(1 + 0.07866 N)$$

$$e = 0.43\left(1 - \frac{100}{T_p}\right)$$

$$T_p = T_{in} + \frac{\frac{\dot{q}_{useful}}{A_c ol}}{(F_R U_L)(1 - F_R)}$$

Heat loss due to forced convection (h_w) was calculated using the correlation of Watmuff et al., (1977) which takes wind velocity (v) into consideration, as shown in Equation (32).

$$h_w = 2.8 + 3.0v \tag{32}$$

The collector outlet water temperature (T_{col}) can then be calculated using Equation (33) based on the assumption that all the useful heat gain ($\dot{q}_{useful}$) is added to water entering the collector. The parameters for the considered solar collector are shown in Table 7.

$$T_{col} = \frac{\dot{q}_{useful}}{\dot{m}_{col} c_{p,in}} + T_{in} \tag{33}$$

Table 7: Considered parameters for solar collector model

Parameter	**Notation**	**Value**	**Unit**
Number of covers	N	1	-
Emittance of plate	ϵ_p	0.95	-
Emittance of cover	ϵ_g	0.9	-
Perimeter	P_{col}	7.4	m
Area of collector	A_{col}	4	m^2
Transmittance-Absorptance product	$(\tau\alpha)_T$	0.8	-
Collector fin efficiency	F'	0.7	-
Collector mass flow rate	$\dot{m}_{col}$	0.0278	kg/s
Insulation conductivity (PIR board)	$k_{ins,col}$	0.021	W/mK
Absorber thickness	L_{abs}	0.5	mm
Edge insulation thickness	$L_{ins,col,e}$	0.025	m
Back insulation thickness	$L_{ins,col,b}$	0.1	m
Mounting angle	θ	30	$degrees$

6.2.2 Storage tank model

Given that the objective of this study is to determine the long-term thermal performance of a solar water storage tank and not the degree of thermal stratification inside the tank, a fully mixed storage tank model was used instead of a commonly used tank model with nodes to reduce the computational time. This assumption might influence the validity of the conclusions drawn from the simulation results, which will be discussed at the end of **Section 6.3**. In this study, three tank configurations are considered, as shown in Figure 72. All storage tank models are insulated with 50 mm glass wool insulation (k_{ins} = $0.0402\ W/mK$) and meet AS/NZS 4234:2008 standard of permitted rate of heat loss for temperature difference of 60°C between the water and the ambient.

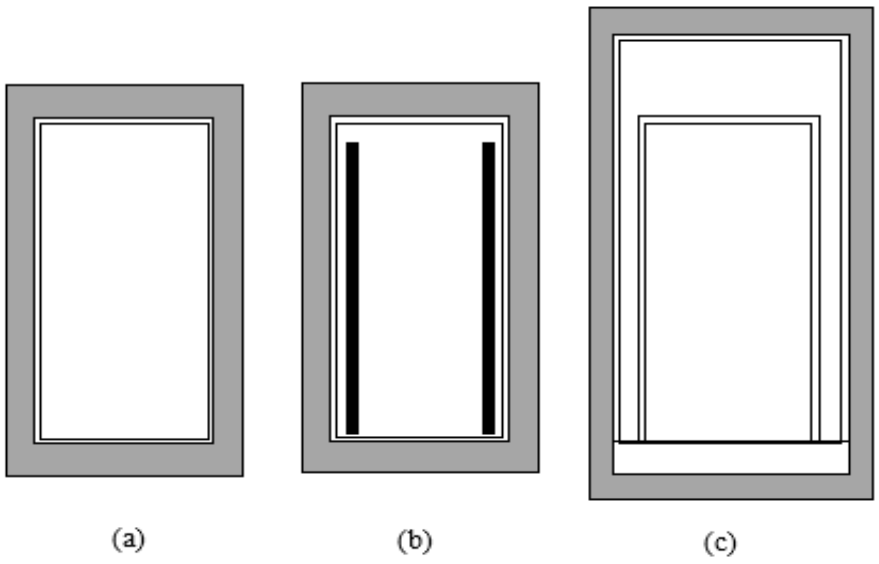

Figure 72: Three tank models considered in this study (a) Configuration A, (b) Configuration B and (c) Configuration C

Configuration A is an ordinary cylindrical storage tank insulated with 50 mm glass wool insulation, which is included as a benchmark case to compare the performance with other configurations. In configuration B, a baffle jacket having the dimensionless baffle length (l/H) of 0.75 and dimensionless baffle channel width (r_b/R) of 0.065

were chosen since this arrangement leads to lowest convection heat transfer inside the tank. For the same reason, air gap insulation having the side gap of 30 mm and top gap of 100 mm was selected. Given that majority of the existing storage tanks are made of stainless-steel, both configuration A and B were assumed to be made of stainless steel while configuration C was assumed to be made of polypropylene. The tank wall thickness of all configurations was assumed to be 3 mm.

Typically, the energy balance of water undergoing static heat loss to the ambient can be modelled as per Equation (34)-(38), according to thermal resistance network shown in Figure 72.

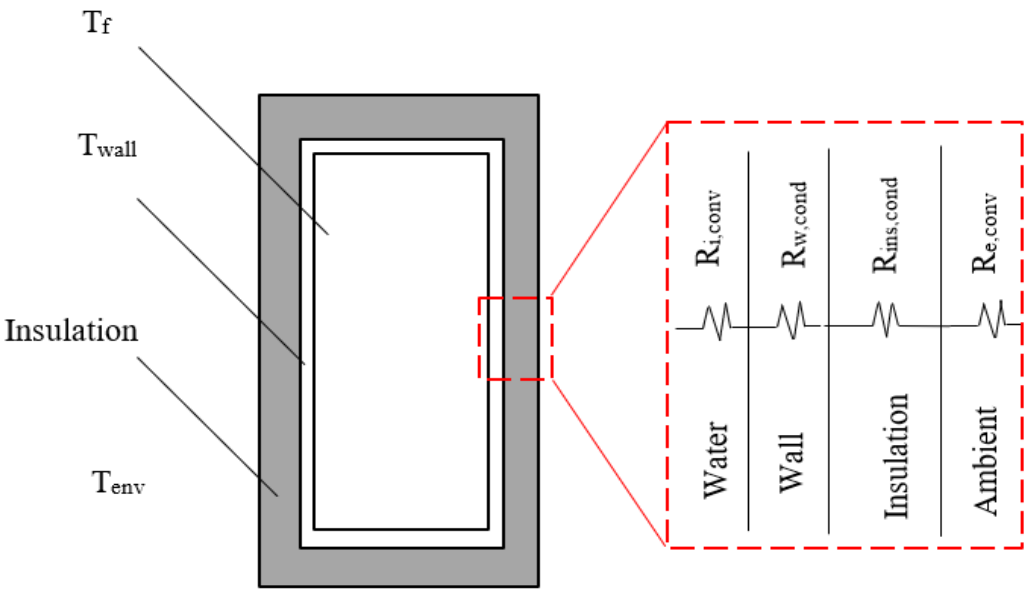

Figure 73: Thermal resistance network of tank configuration A

The rate of change of the temperature of the water can be calculated, as shown in Equation (34).

$$\frac{d\bar{T}_f}{dt} = \frac{\left[-\frac{A_{total}(\bar{T}_f - \bar{T}_w)}{R_{i,conv}}\right]}{\rho_f V_f c_{p,f}} \tag{34}$$

Where, the internal convection resistance, $R_{i,conv}$ can be represented, as shown in Equation (35).

$$R_{i,conv} = \frac{1}{\bar{h}_{i,conv}} \tag{35}$$

and the internal convective heat transfer coefficient, $\bar{h}_{i,conv}$ can be represented, as shown in Equation (36).

$$\bar{h}_{i,conv} = \bar{Nu}\frac{k_f}{L_c} \tag{36}$$

Where, $\bar{Nu}$ is the Nusselt number which can be calculated, as shown in Equation (37).

$$\bar{Nu} = 0.312\, {Ra_T}^{0.285}(\frac{H}{D})^{-0.0424} \tag{37}$$

while the associated characteristic length, L_c can be determined from Equation (13).

The rate of heat loss from the tank to the ambient can be represented as shown in Equation (38).

$$\dot{q}_{loss} = -\frac{A_{total}(\bar{T}_f - \bar{T}_w)}{R_{i,conv}} \tag{38}$$

Given that this chapter examines the change in water temperature for long term operation of a solar water heating system the rate of change of temperature of water can be calculated using Equation (39) that incorporates useful energy gain from the collector and energy loss due to the hot water usage as per the load profile (see Figure 71).

$$\frac{d\bar{T}_f}{dt} = \frac{\dot{m}_{col}c_p(T_{col} - \bar{T}_f) - \frac{A_{total}(\bar{T}_f - \bar{T}_w)}{R_{i,conv}} - \dot{m}_L c_p(\bar{T}_f - T_L)}{\rho_f V_f c_{p,f}} \tag{39}$$

Where, T_L is the makeup cold water temperature, which is assumed to be following the ambient temperature, T_{env}.

On the other hand, energy balance of tank wall can be modelled as per Equation (40)-(44).

$$\frac{d\bar{T}_w}{dt} = \left[\frac{\frac{A_{total}(\bar{T}_f - \bar{T}_w)}{R_{i,conv}} - \frac{A_{total,ins}(\bar{T}_w - T_{env})}{R_{w,cond}+R_{ins,cond}+R_{e,conv}}}{\rho_w V_w c_{p,w}}\right] \tag{40}$$

Conduction resistance due to the wall, $R_{w,cond}$ can be represented, as shown in Equation (41).

$$R_{w,cond} = \frac{L_w}{k_w} \tag{41}$$

Conduction resistance due to the wall, $R_{ins,cond}$ and external convection resistance, $R_{e,conv}$ can be represented, as shown in Equation (42) and (43).

$$R_{ins,cond} = \frac{L_{ins}}{k_{ins}} \tag{42}$$

$$R_{e,conv} = \frac{1}{h_{e,conv}} \tag{43}$$

Configuration B was modelled in the same manner as configuration A apart from the Nusselt number correlation to determine the internal convection heat transfer coefficient h_{i_conv} as shown in Equation (44). It should be noted that the investigated baffle configuration has the dimensionless baffle length of 0.75 and channel width of 0.065 since this arrangement leads to the lowest convection heat transfer inside the tank among all the studied cases.

$$\bar{Nu} = 0.354\, {Ra_T}^{0.259} \left(\frac{H}{D}\right)^{-0.035} \left(\frac{l_b}{H}\right)^{-0.291} \left(\frac{r_b}{R}\right)^{0.054} \tag{44}$$

For configuration C, the thermal resistance network of the tank model is shown in Figure 74. Under these conditions, three domains namely water, inner wall, and outer wall were modelled with individual energy balances. The rate of change of temperature

of water can be calculated using Equation (45).

$$\frac{d\bar{T}_f}{dt} = \Big[\frac{\dot{m}_{col}c_{p,f}(T_{col}-\bar{T}_f) - \frac{(A_t+A_s)(\bar{T}_f-\bar{T}_{w1})}{R_{i,conv}} - \frac{A_b(\bar{T}_f-T_{env})}{R_{i,conv}+R_{w,cond}+R_{ins,cond}+R_{e,conv}}}{\rho V_f c_{p,f}}\Big]\ldots \\ -\Big[\frac{\dot{m}_L c_{p,f}(\bar{T}_f-T_L)}{\rho V_f c_{p,f}}\Big] \tag{45}$$

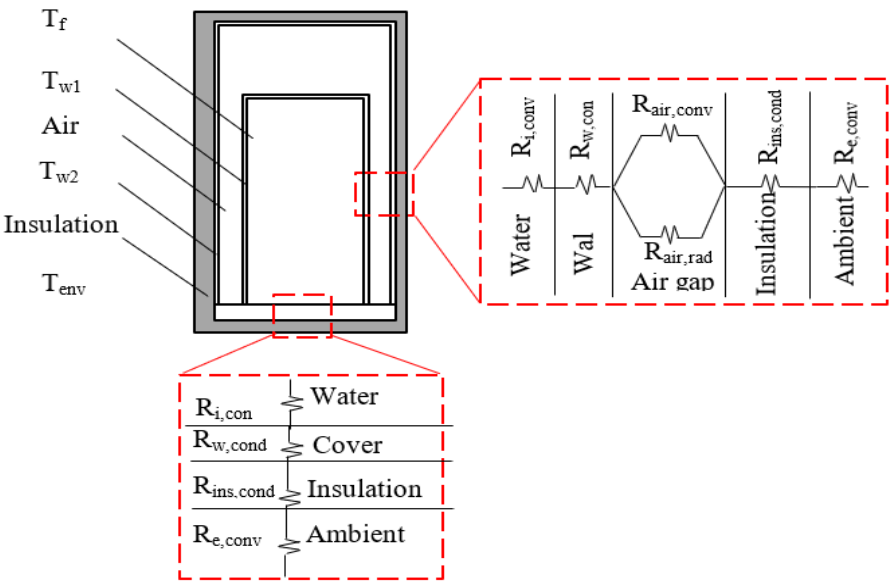

Figure 74: Thermal resistance network of tank configuration C

To determine the rate of change of inner wall temperature (T_{w1}), Equation (46) can be used.

$$\frac{d\bar{T}_{w1}}{dt} = \frac{\frac{(A_t+A_s)(\bar{T}_f-\bar{T}_{w1})}{R_{i,conv}} - \frac{A_{w1,total}(\bar{T}_{w1}-\bar{T}_{w2})}{R_{i,cond}+R_{air,total}}}{\rho_{w1}V_{w1}c_{p,w1}} \tag{46}$$

Where, $R_{air,total}$ and $R_{air,conv}$ can be calculated, as shown in Equation (47) and (48).

$$R_{air,total} = \frac{1}{\frac{1}{R_{air,conv}} + \frac{1}{R_{air,rad}}} \tag{47}$$

$$R_{air,conv} = \frac{1}{\bar{h}_{w1}} \tag{48}$$

Convective heat transfer coefficient inside the air gap $\bar{h}_{w1}$ can be calculated, as shown in Equation (49).

$$\bar{h}_{w1} = \frac{\bar{N}uk_{air}}{L_c} \tag{49}$$

Where $\bar{N}u$ is the Nusselt number, reflecting convection inside the air gap, and can be calculated from Equation (50), L_c is the characteristic length of air gap (see Equation (24)) and k_{air} is the thermal conductivity of water at the average temperature between the two tank walls.

$$\bar{N}u = 0.066\ {Ra_A}^{0.343} (\frac{H_{w1}}{R_{w1}})^{-0.082} \tag{50}$$

Where, $R_{air,rad}$ can be calculated, as shown in Equation (51).

$$R_{air,rad} = \frac{1}{h_{rad}} \tag{51}$$

Radiative heat transfer coefficient inside the air gap (h_{rad}) can be represented, as shown in Equation (52). In Equation (52), the emissivity of polypropylene tank wall was assumed to be 0.97.

$$h_{rad} = \epsilon_w \sigma (\bar{T}_{w1}^2 + \bar{T}_{w2}^2)(\bar{T}_{w1} + \bar{T}_{w2}) \tag{52}$$

To determine the rate of change of outer wall temperature T_{w2}, Equation (53) can be used.

$$\frac{d\bar{T}_{w2}}{dt} = [\frac{\frac{A_{w1,total}(\bar{T}_{w1}-\bar{T}_{w2})}{R_{w_cond}+R_{air,total}} - \frac{A_{w2,total}(\bar{T}_{w2}-T_{env})}{R_{w,cond}+R_{ins,cond}+R_{e,conv}}}{\rho_{w2}V_{w2}c_{p,w2}}] \tag{53}$$

The rate of heat loss from the tank can be represented using equation (54).

$$\dot{q}_{loss} = -\frac{A_{total}(\bar{T}_f - \bar{T}_w)}{R_{i,conv}} - \dot{m}_L c_{p,f}(\bar{T}_f - T_L) \tag{54}$$

The thermal efficiency of the tank (η) could be represented by the ratio of the energy collected inside the tank to the useful energy gain supplied from the collector, as shown in Equation (55). The parameters related to the considered storage tank models are shown in Table 8.

$$\eta = \frac{\sum_{t=0}^{u} \dot{q}_{useful} - \sum_{t=0}^{u} \dot{q}_{loss}}{\sum_{t=0}^{u} \dot{q}_{useful}} \tag{55}$$

Thermal efficiency of the solar collector can be determined by the ratio of useful energy gain over total energy available from incident solar radiation, as shown in Equation (56).

$$\text{Collector Efficiency} = \frac{\sum_{t=0}^{u} \dot{q}_{useful}}{A_{col} \sum_{t=0}^{u} G} \tag{56}$$

Where, u is the time frame of interest.

Table 8: Considered parameters for storage tank models

Parameter	Notation	Value	Unit
Configuration A and B			
Tank wall density	ρ_w	0.95	kg/m^3
Tank wall specific heat capacity	$c_{p,w}$	0.9	J/kgK
Tank wall conducitvity	k_w	7.4	W/mK
Configuration C			
Tank wall density	ρ_{w1}/ρ_{w2}	0.95	kg/m^3
Tank wall specific heat capacity	$c_{p,w1}/c_{p,w2}$	0.9	J/kgK
Tank wall conducitvity	k_{w1}/k_{w2}	7.4	W/mK
Bottom cover thickness	L_{cover}	0.05	m

6.3 Results and Discussion

To investigate the thermal performance of configuration A, B, and C with changing aspect ratios ranging from 1 to 3 for a fixed tank volume of 200 L, monthly averaged daily weather data of the hottest summer month and coldest winter month of the year in Auckland were chosen. The corresponding solar irradiation and ambient temperature profiles were plotted in Figure 75.

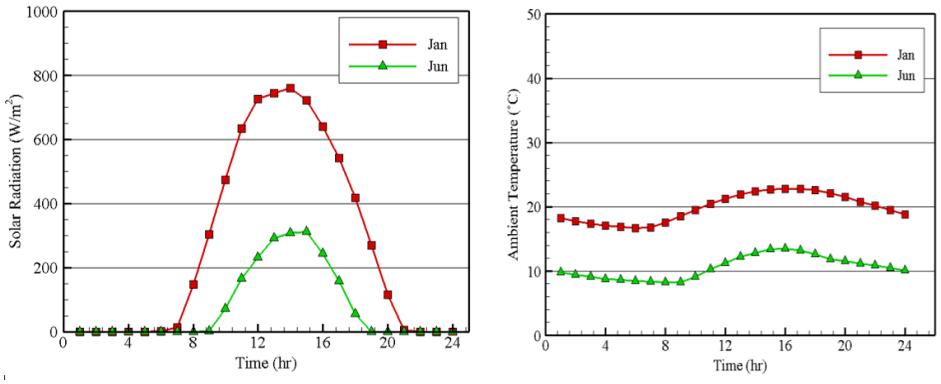

(a) (b)

Figure 75: Monthly averaged daily (a) Solar irradiation and (b) Ambient temperature for January and June

Figure 76 shows thermal efficiencies of different tank configurations with varying tank aspect ratios. The associated uncertainty analysis for predicted thermal efficiency can be found in Appendix A3. As expected, it can be observed that increasing the tank aspect ratio increases the tank thermal efficiency. This agrees with the findings from preceding chapters and this behavior is associated with decreasing natural convection heat transfer inside the tank with increasing tank aspect ratio. In addition, it can be seen that the tank thermal efficiencies in the winter (June) is much lower than the summer (January). The reason for this is the lower level of solar radiation and the lower ambient temperatures in the winter that results in increased heat loss from the storage tanks.

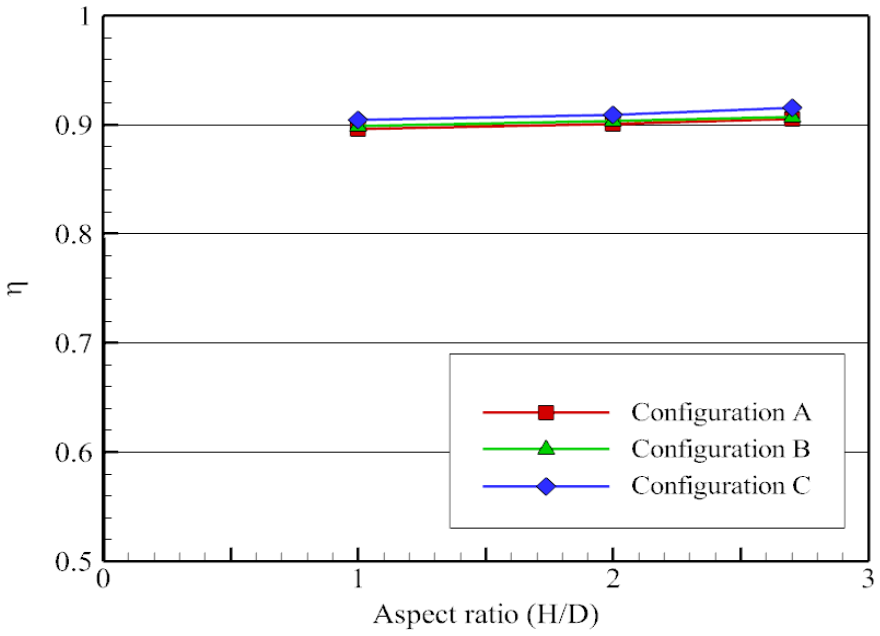

(a)

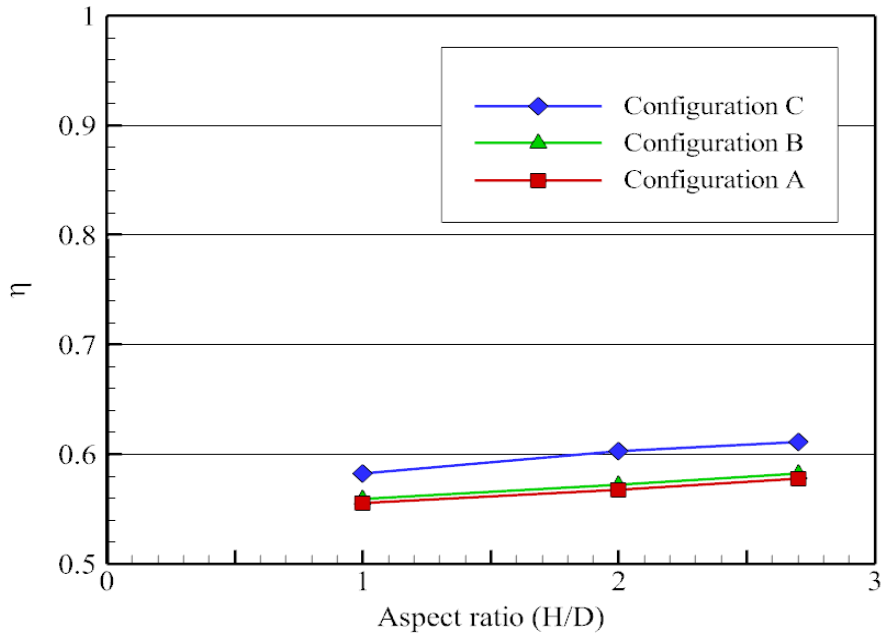

(b)

Figure 76: Monthly averaged daily tank thermal efficiency for tank configurations with different aspect ratio for (a) January and (b) June

To investigate the effectiveness of the baffle and air gap insulation, configuration A was selected as the benchmark case. Monthly averaged daily thermal efficiency of each month for configuration B and C with same thickness of insulation was obtained using the typical meteorological year (TMY) data for Auckland and compared with the benchmark case, as illustrated in Figure 77.

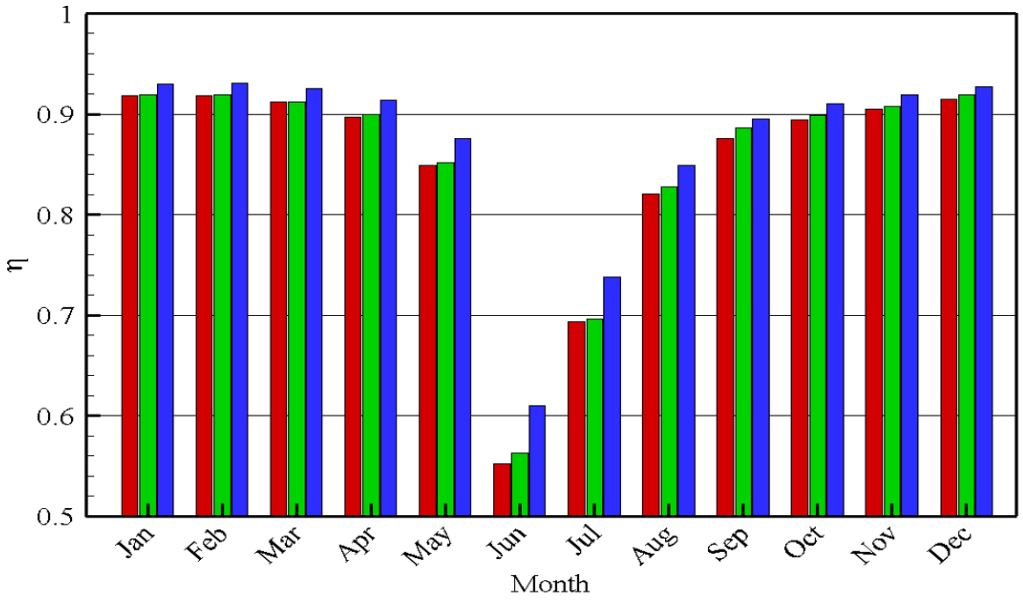

(a)

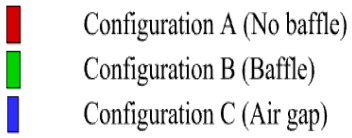

(b)

Figure 77: Monthly averaged daily tank thermal efficiency of a typical meteorological year in Auckland

From Figure 77, it can be observed that, there is only a small difference in the daily thermal efficiency of the tank between configuration B and the benchmark case. However, if we consider the whole solar water heating system and examine the daily cumulative amount of heat loss for the same solar irradiation received by the collector, we can see that the tank equipped with baffle loses slightly lesser heat to the ambient

relative to the benchmark case, as shown in Figure 78. On the other hand, significantly lower daily cumulative heat loss of up to 320 kJ, relative to the benchmark case are observed from configuration C.

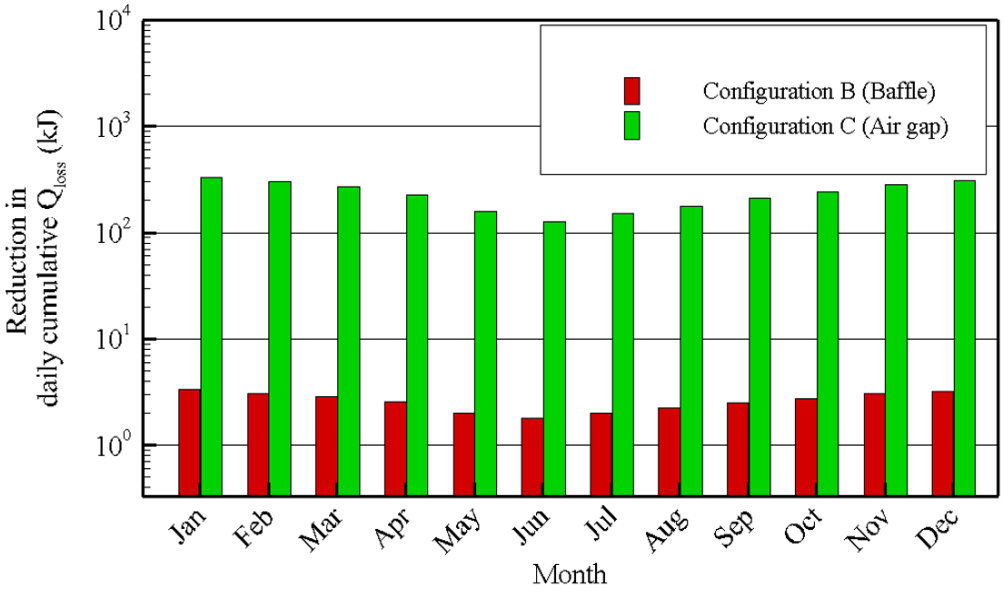

Figure 78: Reduction in monthly averaged daily cumulative heat loss relative to the benchmark case (Configuration A)

It is also interesting to see from Figure 76 that during summer months (December – February), there is only a small difference in the daily thermal efficiency of the tank between configuration C and the benchmark case but the difference becomes higher in the remaining months, especially during winter months (June – August). To explain this, we first need to examine the temperature difference between the average water and ambient temperatures for a representative day of every month throughout the entire year, as illustrated in Figure 79.

From Figure 79, it is apparent that the rate of heat loss is significantly lower during the winter months in comparison to the summer months due to lower temperature difference between the water and the ambient. This influences the temperature difference between the two walls that made up the air gap, resulting in lower temperature driving force for convection inside the air gap during the winter month, as shown in Figure 80.

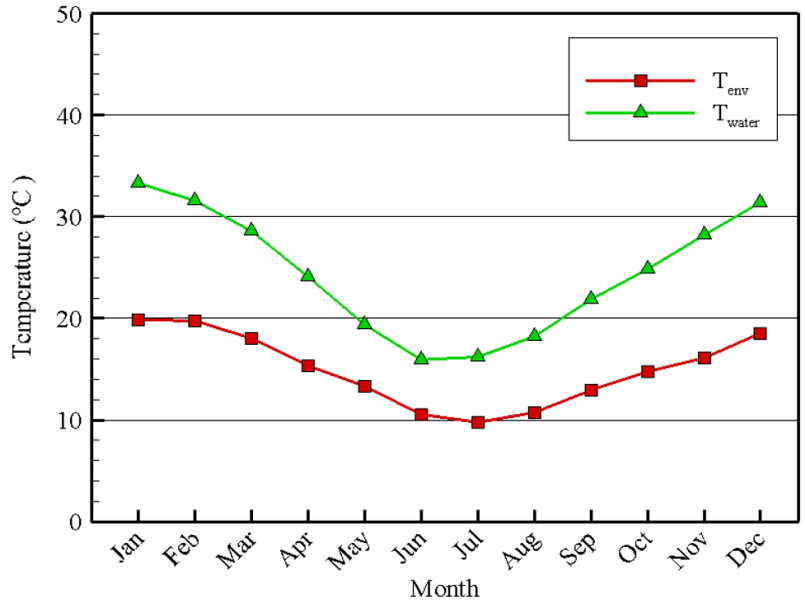

Figure 79: Variation of water and ambient temperatures during representative days of January and June

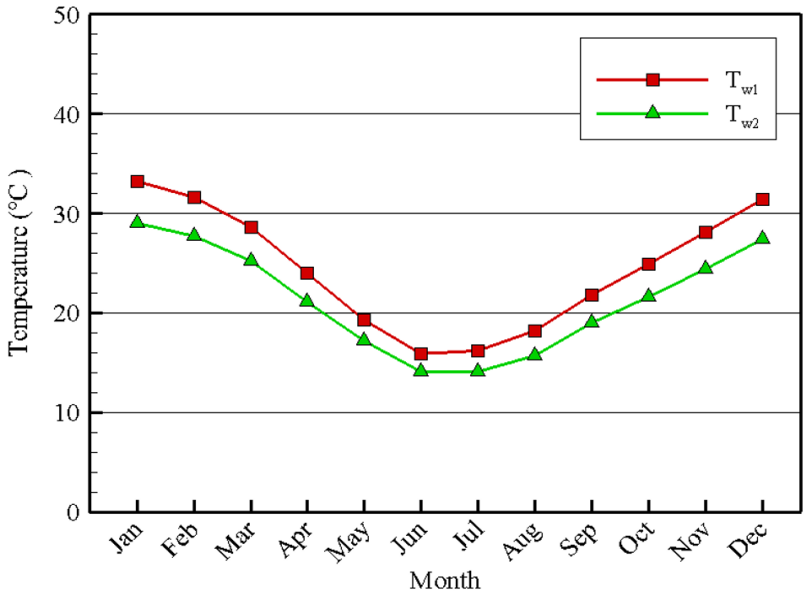

Figure 80: Variation of inner and outer wall temperatures across the air gap during representative days of January and June

Given that convection heat transfer across the air gap is largely dependent on the temperature difference across the air gap, lower temperature difference leads to lower convective heat transfer coefficient which provides more resistance to heat flow, as

indicated in Figure 81. As a result, air gap becomes more effective with higher resistance to heat flow during the winter month and thus, larger difference in thermal efficiency compared to the benchmark case was observed.

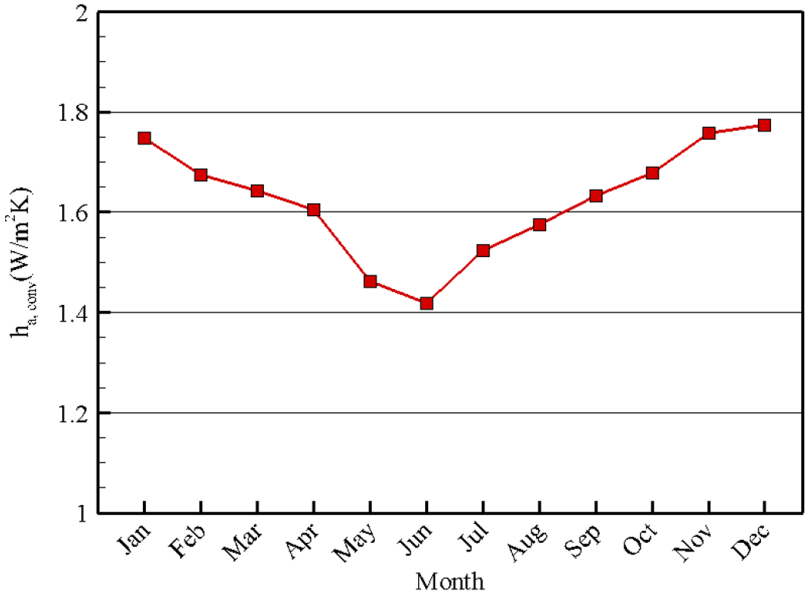

Figure 81: Variation of convective heat transfer coefficient inside the air gap during representative days of January and June

The obtained results suggest that utilizing an air gap as an addition insulation layer provides a noticeable increase in thermal efficiency of tanks with low cumulative heat loss. The results indicate that using air gap as an additional layer of insulation brings about an average of 2% improvement in thermal efficiency. In terms of daily cumulative energy loss, this improvement translates to retaining about 8400 kJ of thermal energy more than a tank without air gap insulation.

It is also important to note that since the thermal efficiency of the tank was calculated for a fully mixed tank model, the presence of various degrees of thermal stratification can lead to lower rate of heat loss from the tank, which in turn can result in higher predicted thermal storage efficiency than the one presented in this chapter. This is because any form of buoyancy-driven flow inside the tank is greatly suppressed by the presence of thermal stratification.

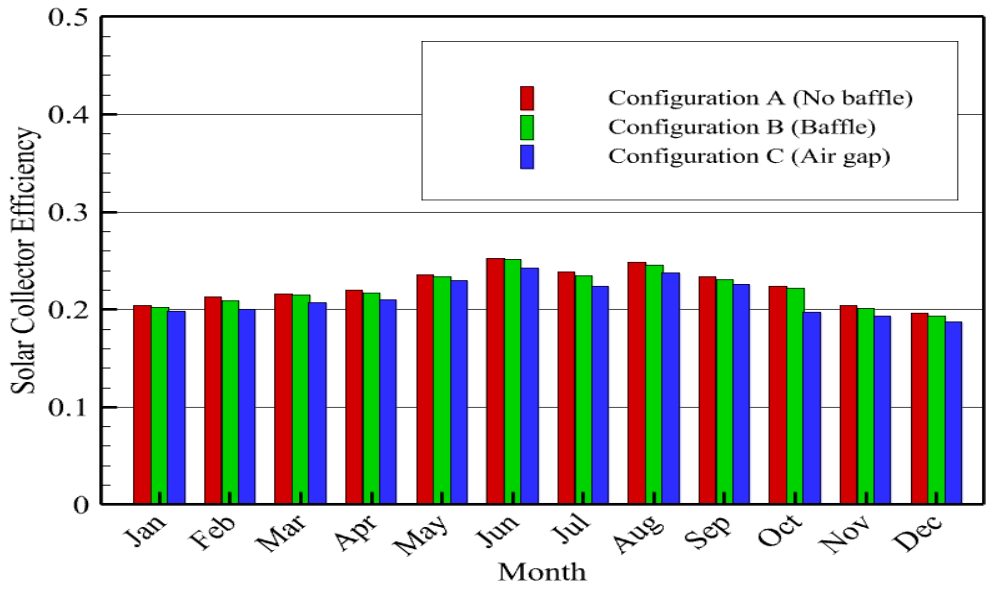

Figure 82: Monthly averaged daily solar collector thermal efficiency of a typical meteorological year in Auckland

Although it is not the main focus of this chapter, it was decided to examine the solar collector thermal efficiency, as shown in Figure 82. The collector efficiency is higher in the winter months (June - August) compared to summer months (December - February). This can be attributed to the fact that the temperature difference between tank water sent to the collector inlet and the ambient is higher in summer months compared to winter months, which results in an increased rate of heat loss and subsequently lowers the collector efficiency.

In addition, it can be seen that the solar collector efficiency between different tank configurations show a trend opposite to that of the tank efficiency. Given the assumption of a fully mixed tank model, improvement in thermal efficiency for Configuration B and C led to higher temperature of water at the collector inlet compared to Configuration A. This results in a decrease in useful heat gain, and subsequently a drop in collector efficiency.

These observations show that it is important to include thermal stratification in the tank model if accurate collector efficiency results are desired. This approach will lead

to improvement in collector efficiency since it was demonstrated that both baffle and air gap modifications reduce convection heat transfer inside the tank, which is one of the factors that degrades thermal stratification.

6.4 Conclusions

This chapter examines the improvements in long-term performance of solar water storage tanks with baffle jacket and air gap insulation in comparison to an ordinary storage tank.

The modelling results show that the use of a baffle inside the storage tank improves its thermal efficiency to some extent, as evident from the modelling results. Similarly, the use of the air gap as an insulation in solar storage tanks can improve the efficiency of a tank for the same degree of ordinary insulation. Therefore, the amount of ordinary insulation required can be reduced to lower capital costs without compromising the system's performance.

Moreover, this chapter also illustrates the ease of implementation of the new correlations into a typical mathematical model to determine the long-term performance of solar water storage tanks.

Chapter 7

Conclusions and Recommendations for Future Work

7.1 Conclusions

Despite the fact that solar water heaters present a viable alternative to traditional water heating methods in fulfilling domestic hot water demand, the overall efficiency of a solar water heating system is still poor due to limitations imposed by storage tanks in losing heat to the ambient. Considering this, some key contributions to the research area of solar hot water storage tanks were made in this study.

Firstly, a transient analysis of natural convection flow inside initially unstratified vertical cylindrical storage tank shows that thermal boundary layer flow on the tank sidewall governs the natural convective heat transfer coefficient inside the tank, which varies with time elapsed since the initial unstratified state. As a result, it is difficult to estimate this coefficient without having the prior knowledge of initial unstratified temperature profile inside the tank, which is difficult to keep track of during the full operation cycle of a solar water storage tank.

To uncouple the natural convective heat transfer coefficient from time elapsed since the initial unstratified state, a steady state analysis of constant temperature difference between the water and the tank wall was conducted. This approach has led to the development of a generalized correlation that can predict the natural convection heat transfer coefficient inside the tank independent of initial temperature profile. This ability of the proposed correlation could become an important tool in effectively optimizing the performance of solar storage tanks.

Secondly, it was shown that the rate of natural convection heat transfer can be reduced up to a maximum of more than 40% in Nusselt number can be achieved by mounting a thin adiabatic cylindrical baffle jacket inside the tank close to the side wall. To aid the engineers in designing storage tanks with such passive baffle to reduce the rate of heat loss in the future, a generalized correlation that can predict the natural convection heat transfer coefficient inside the tank with baffle jacket was developed.

Finally, numerical analysis of insulation performance of a simple U-shaped trapped air space encapsulating a storage tank shows that the optimum air gap with minimum heat flux was shown to be 30 mm annular gap and 100 mm coaxial gap, within the range of investigated gap sizes between 10 and 100 mm. This led to the development of a heat transfer correlation that describes the variation of natural convective heat transfer coefficient with geometrical configurations of the air gap, which will be essential in designing storage tanks encapsulated within an air gap to reduce the rate of heat loss in the future.

Long-term performance simulations of solar storage tanks for the full operation cycle of a solar water heat system indicate that using a baffle inside the storage tank also improves its thermal efficiency up to 3% while the level of insulation provided by natural convection inside the air gap enhances the thermal efficiency up to 8%. Based on this, the air gap is capable of replacing the required ordinary insulation to some extent, which could lower capital costs without compromising the system's performance.

7.2 Recommendations for Future Work

Besides the findings presented in this study regarding the effect of heat loss on performance of solar storage tanks, there are a number of avenues that could be investigated in the future.

Firstly, it is worthwhile to investigate heat loss from storage tanks during charging and discharging process when a mixed convection takes place inside the tanks since the current study only examined standing heat loss. This could improve the obtained correlations by incorporating operating parameters such as charging or discharging flow rate that may have an influence on the rate of heat loss.

Secondly, it was recommended to investigate steady state heat loss from storage tanks using the same approach but with the degree of stratification higher than the ones examined in this study in the order of 40-60°C, since this reflects the typical temperature difference of water layers within the actual tank and likely to improve the accuracy of the developed correlation.

Although this study showed the potential benefits of using air gap as an insulation in terms of thermal performance, further economic analysis is necessary before the actual design process can take place. Thus, it is recommended to use the obtained heat transfer correlation for estimating the rate of heat loss through the air gap as part of economic analysis to fully realize the benefits of air gap insulation. It would also be beneficial to explore means to reduce radiation heat transfer across the air gap such as coating the tank walls with low emissivity paint to improve the performance of air gap insulation.

Finally, it is worth exploring the effect of thermal conductivity of baffle jacket material on natural convection heat transfer inside the tank since this study only considered a non-conducting (adiabatic) baffle jacket. The changes in thermal conductivity of baffle jacket can affect heat conduction across the baffle, which could vary the natural convection flow inside the tank different from the one reported in this study.

References

Adhikari, R., Kumar, A. & Sootha, G. (1995). Simulation studies on a multi-stage stacked tray solar still. *Solar Energy*, *54*(5), 317–325.

Adrian, R. (1997). Dynamic ranges of velocity and spatial resolution of particle image velocimetry. *Measurement Science and Technology*, *8*(12), 1393.

Al-Najem, N. (1993). Degradation of a stratified thermocline in a solar storage tank. *International journal of energy research*, *17*(3), 183–191.

Altaç, Z. & Uğurlubilek, N. (2016). Assessment of turbulence models in natural convection from two-and three-dimensional rectangular enclosures. *International Journal of Thermal Sciences*, *107*, 237–246.

Altuntop, N., Arslan, M., Ozceyhan, V. & Kanoglu, M. (2005). Effect of obstacles on thermal stratification in hot water storage tanks. *Applied thermal engineering*, *25*(14-15), 2285–2298.

Andersen, E., Furbo, S. & Fan, J. (2007). Multilayer fabric stratification pipes for solar tanks. *Solar Energy*, *81*(10), 1219–1226.

Andersen, E., Furbo, S., Hampel, M., Heidemann, W. & Müller-Steinhagen, H. (2008). Investigations on stratification devices for hot water heat stores. *International Journal of Energy Research*, *32*(3), 255–263.

Basu, D. N., Bhattacharyya, S. & Das, P. (2013). Development of a unified model for the steady-state operation of single-phase natural circulation loops. *International Journal of Heat and Mass Transfer*, *62*, 452–462.

Batchelor, G. (1954). Heat transfer by free convection across a closed cavity between vertical boundaries at different temperatures. *Quarterly of Applied Mathematics*, *12*(3), 209–233.

Bejan, A. (2013). *Convection heat transfer*. John wiley & sons.

Billington, N. (1952). *Unsteady natural convection in enclosures with stratified medium*. Cleaver-Hume Press.

Bouhal, T., Fertahi, S., Agrouaz, Y., El Rhafiki, T., Kousksou, T. & Jamil, A. (2017). Numerical modeling and optimization of thermal stratification in solar hot water storage tanks for domestic applications: Cfd study. *Solar Energy*, *157*, 441–455.

Brown, N. & Lai, F. (2011). Enhanced thermal stratification in a liquid storage tank with a porous manifold. *Solar energy*, *85*(7), 1409–1417.

Budihardjo, I. (2005). *Evacuated tubular solar water heaters* . University of New South Wales. (PhD thesis)

Cengel, Y. A., Pérez, H. et al. (2004). *Heat transfer: a practical approach. transferencia de calor*. Boston: WBC McGraw-Hill.

Chaney, S., Humphrey, J., Month, L. & Shah, A. (1984). Flow and heat transfer of a stably stratified fluid through an enclosure. *Journal of Solar Energy Engineering*, *106*(3), 261-270.

Chu, T. & Goldstein, R. J. (1973). Turbulent convection in a horizontal layer of water. *Journal of Fluid Mechanics*, *60*(1), 141–159.

Cotter, M. A. & Charles, M. E. (1993). Transient cooling of petroleum by natural convection in cylindrical storage tanks—ii. effect of heat transfer coefficient, aspect ratio and temperature-dependent viscosity. *International Journal of Heat and Mass Transfer*, *36*(8), 2175–2185.

Davis, G. D. V. & Thomas, R. (1969). Natural convection between concentric vertical cylinders. *The Physics of Fluids*, *12*(12), II–198.

Dinh, T. & Nourgaliev, R. (1997). Turbulence modelling for large volumetrically heated liquid pools. *Nuclear Engineering and Design*, *169*(1-3), 131–150.

Duffie, J. A., Beckman, W. A. & Blair, N. (2020). *Solar engineering of thermal processes, photovoltaics and wind*. John Wiley & Sons.

Elder, J. (1965). Turbulent free convection in a vertical slot. *Journal of fluid mechanics*, *23*(1), 99–111.

Emery, A. & Chu, N. (1965). Heat transfer across vertical layers. *Journal of Heat Transfer*, *87*(1), 110-114.

Fan, J. & Furbo, S. (2012a). Thermal stratification in a hot water tank established by heat loss from the tank. *Solar Energy*, *86*(11), 3460–3469.

Fan, J. & Furbo, S. (2012b). Buoyancy driven flow in a hot water tank due to standby heat loss. *Solar Energy*, *86*(11), 3438–3449.

Fantucci, S., Lorenzati, A., Kazas, G., Levchenko, D. & Serale, G. (2015). Thermal energy storage with super insulating materials: a parametrical analysis. *Energy Procedia*, *78*, 441–446.

Fischer, L., Dijkmans, A. & van Koppen, C. (1978). Stratification effects in the short and long term storage of solar heat. In *Sun: mankind's future source of energy: proceedings of the international solar energy society congress, new delhi, january 1978* (pp. 554–558).

Fishbaugher, M. J. (1988). *Natural convection and conduction in a vertical annulus with a concentric baffle: a numerical study* (Unpublished master's thesis). Oregon State University.

García-Marí, E., Gasque, M., Gutiérrez-Colomer, R. P., Ibáñez, F. & González-Altozano, P. (2013). A new inlet device that enhances thermal stratification during charging in a hot water storage tank. *Applied thermal engineering*, *61*(2), 663–669.

Garon, A. & Goldstein, R. (1973). Velocity and heat transfer measurements in thermal convection. *The physics of Fluids*, *16*(11), 1818–1825.

Gasque, M., González-Altozano, P., Maurer, D., Moncho-Esteve, I. J., Gutiérrez-Colomer, R. P., Palau-Salvador, G. & García-Marí, E. (2015). Study of the influence of inner lining material on thermal stratification in a hot water storage tank. *Applied Thermal Engineering*, *75*, 344–356.

Ghaddar, N. (1994). Stratified storage tank influence on performance of solar water heating system tested in beirut. *Renewable energy*, *4*(8), 911–925.

Goetzberger, A. & Rommel, M. (1987). Prospects for integrated storage collector systems in central europe. *Solar Energy*, *39*(3), 211–219.

Goldstein, R. (1969). Thermal convection in a horizontal layer of air. *Prog. Heat Mass Transfer*, *2*, 55–57.

Gutierrez, G., Hincapie, F., Duffie, J. & Beckman, W. (1974). Simulation of forced circulation water heaters; effects of auxiliary energy supply, load type and storage capacity. *Solar Energy*, *15*(4), 287–298.

Han, S., Wu, S. & Christensen, D. (1978). *Effects of thermal stratification in water storage tank for the performance of a solar hot water system* (Tech. Rep.). Alabama Univ., Huntsville (USA).

Hollands, K., Raithby, G. & Konicek, L. (1975). Correlation equations for free convection heat transfer in horizontal layers of air and water. *International Journal of Heat and Mass Transfer*, *18*(7-8), 879–884.

Hutchinson, B. & Raithby, G. (1986). A multigrid method based on the additive correction strategy. *Numerical Heat Transfer, Part A: Applications*, *9*(5), 511–537.

Hyun, J. M. (1984). Transient process of thermally stratifying an initially homogeneous fluid in an enclosure. *International Journal of Heat and Mass Transfer*, *27*(10), 1936–1938.

Jaluria, Y. & Gupta, S. (1982). Decay of thermal stratification in a water body for solar energy storage. *Solar energy*, *28*(2), 137–143.

Jamar, A., Majid, Z., Azmi, W., Norhafana, M. & Razak, A. (2016). A review of water heating system for solar energy applications. *International Communications in Heat and Mass Transfer*, *76*, 178–187.

Jordan, U. & Furbo, S. (2005). Thermal stratification in small solar domestic storage tanks caused by draw-offs. *Solar energy*, *78*(2), 291–300.

Kalogirou, S. A. (2004). Solar thermal collectors and applications. *Progress in energy and combustion science*, *30*(3), 231–295.

Kemp, C. (1891). Us patents no 451384, april 28, 1891. *Patent Records*.

Khalifa, A.-J. N. (1998). Forced versus natural circulation solar water heaters: A comparative performance study. *Renewable energy*, *14*(1-4), 77–82.

Khurana, H., Tiwari, S., Majumdar, R. & Saha, S. K. (2021). Comparative evaluation of circular truncated-cone and paraboloid shapes for thermal energy storage tank based on thermal stratification performance. *Journal of Energy Storage*, *34*, 102-191.

Knudsen, S. (2004). *Investigation and optimisation of heat storage tanks for low-flow sdhw systems* . (PhD thesis)

Knudsen, S., Morrison, G., Behnia, M. & Furbo, S. (2005). Analysis of the flow structure and heat transfer in a vertical mantle heat exchanger. *Solar energy*, *78*(2), 281–289.

Kober, T., Schiffer, H.-W., Densing, M. & Panos, E. (2020). Global energy perspectives to 2060–wec's world energy scenarios 2019. *Energy Strategy Reviews*, *31*, 100523.

Krishnamurti, R. (1970). On the transition to turbulent convection. part 2. the transition to time-dependent flow. *Journal of Fluid Mechanics*, *42*(2), 309–320.

Kumar, R. & Kalam, M. (1991). Laminar thermal convection between vertical coaxial isothermal cylinders. *International journal of heat and mass transfer*, *34*(2), 513–524.

Kwak, H. S., Kuwahara, K. & Hyun, J. M. (1998). Convective cool-down of a contained fluid through its maximum density temperature. *International journal of heat and mass transfer*, *41*(2), 323–333.

Lam, C. & Bremhorst, K. (1981). A modified form of the k-ε model for predicting wall turbulence. *Journal of Fluids Engineering*, *103*(3), 456-460.

Lavan, Z. & Thompson, J. (1977). Experimental study of thermally stratified hot water storage tanks. *Solar energy*, *19*(5), 519–524.

Lee, Y., Korpela, S. A. & Horne, R. N. (1982). Structure of multicellular natural convection in a tall vertical annulus. In *International heat transfer conference digital library.*

Le Quéré, P. (1990). Transition to unsteady natural convection in a tall water-filled cavity. *Physics of Fluids A: Fluid Dynamics*, *2*(4), 503–515.

Li, A., Cao, F., Zhang, W., Shi, B. & Li, H. (2018). Effects of different thermal storage tank structures on temperature stratification and thermal efficiency during charging. *Solar Energy*, *173*, 882–892.

Li, G. (2016). Sensible heat thermal storage energy and exergy performance evaluations. *Renewable and Sustainable Energy Reviews*, *53*, 897–923.

Lin, W. & Armfield, S. (1999). Direct simulation of natural convection cooling in a vertical circular cylinder. *International Journal of Heat and Mass Transfer*, *42*(22), 4117–4130.

Lin, W. & Armfield, S. (2001). Natural convection cooling of rectangular and cylindrical containers. *International Journal of Heat and Fluid Flow*, *22*(1), 72–81.

Lin, W. & Armfield, S. (2005). Long-term behavior of cooling fluid in a vertical cylinder. *International Journal of Heat and Mass Transfer*, *48*(1), 53–66.

Lin, Y. & Akins, R. (1986). Thermal description of pseudosteady-state natural convection inside a vertical cylinder. *International journal of heat and mass transfer*, *29*(2), 301–307.

Malkus, W. & Veronis, G. (1958). Finite amplitude cellular convection. *Journal of Fluid Mechanics*, *4*(3), 225–260.

Mawire, A. & Taole, S. (2013). Heat loss estimation in a small vertical cylindrical stratified oil storage tank. In *2013 proceedings of the 21st domestic use of energy conference* (pp. 1–7).

Medebber, M. A., Retiel, N., Aissa, A., El Ganaoui, M. et al. (2020). Transient numerical analysis of free convection in cylindrical enclosure. In *Matec web of conferences* (Vol. 307, p. 01029).

Mekhilef, S., Saidur, R. & Safari, A. (2011). A review on solar energy use in industries. *Renewable and sustainable energy reviews*, *15*(4), 1777–1790.

Mohamad, A. (1997). Integrated solar collector–storage tank system with thermal diode. *Solar energy*, *61*(3), 211–218.

Moncho-Esteve, I. J., Gasque, M., González-Altozano, P. & Palau-Salvador, G. (2017). Simple inlet devices and their influence on thermal stratification in a hot water storage tank. *Energy and Buildings*, *150*, 625–638.

Murthy, S. S., Nelson, J. & Rao, T. S. (1992). Effect of wall conductivity on thermal stratification. *Solar Energy*, *49*(4), 273–277.

Nahar, N. (2002). Capital cost and economic viability of thermosyphonic solar water heaters manufactured from alternate materials in india. *Renewable Energy*, *26*(4), 623–635.

Nithiarasu, P., Sundararajan, T. & Seetharamu, K. (n.d.). Finite element analysis of transient natural convection in an odd-shaped enclosure. *International Journal of Numerical Methods for Heat & Fluid Flow*, *8*(2), 199-216.

Njoku, H., Ekechukwu, O. & Onyegegbu, S. (2014). Analysis of stratified thermal storage systems: An overview. *Heat and mass transfer*, *50*(7), 1017–1030.

Oliveski, R. D. C. (2000). *Análise numérica e experimental dos campos de temperatura e velocidade em armazenadores térmicos* . (PhD thesis)

Oliveski, R. D. C., Krenzinger, A. & Vielmo, H. A. (2003). Cooling of cylindrical vertical tanks submitted to natural internal convection. *International journal of heat and mass transfer*, *46*(11), 2015–2026.

Omer, S., Riffat, S. & Qiu, G. (2007). Thermal insulations for hot water cylinders: a review and a conceptual evaluation. *Building Services Engineering Research and Technology*, *28*(3), 275–293.

Otis, D. & Roessler, J. (1987). Development of stratification in a cylindrical enclosure. *International journal of heat and mass transfer*, *30*(8), 1633–1636.

Prasad, V. & Kulacki, F. (1985). Free convective heat transfer in a liquid-filled vertical annulus. *Journal of Heat Transfer*, *107*(3), 596-602.

Pushpa, B., Sankar, M. & Makinde, O. D. (2020). Optimization of thermosolutal convection in vertical porous annulus with a circular baffle. *Thermal Science and Engineering Progress*, *20*, 100735.

Raffel, M., Willert, C. E., Kompenhans, J. et al. (1998). *Particle image velocimetry: a practical guide* (Vol. 2). Springer.

Rehim, A. & Sayed, Z. (1998). A new design of solar water heater. In *Proceedings of the indian academy of sciences-chemical sciences* (Vol. 110, pp. 373–384).

Rincón-Casado, A., Sánchez de la Flor, F., Chacón Vera, E. & Sánchez Ramos, J. (2017). New natural convection heat transfer correlations in enclosures for building performance simulation. *Engineering applications of computational fluid mechanics*, *11*(1), 340–356.

Roache, P. J. (1998). *Verification and validation in computational science and engineering* (Vol. 895). Hermosa Albuquerque, NM.

Rodriguez, I., Castro, J., Perez-Segarra, C. & Oliva, A. (2009). Unsteady numerical simulation of the cooling process of vertical storage tanks under laminar natural convection. *International Journal of Thermal Sciences*, *48*(4), 708–721.

Rossby, H. (1969). A study of bénard convection with and without rotation. *Journal of Fluid Mechanics*, *36*(2), 309–335.

Rubel, A. & Landis, F. (1969). Numerical study of natural convection in a vertical rectangular enclosure. *The Physics of Fluids*, *12*(12), II–208.

Sadhishkumar, S. & Balusamy, T. (2014). Performance improvement in solar water heating systems—a review. *Renewable and Sustainable Energy Reviews*, *37*, 191–198.

Shah, L. J., Andersen, E. & Furbo, S. (2005). Theoretical and experimental investigations of inlet stratifiers for solar storage tanks. *Applied Thermal Engineering*, *25*(14-15), 2086–2099.

Shah, L. J. & Furbo, S. (2003). Entrance effects in solar storage tanks. *Solar energy*, *75*(4), 337–348.

Sharp, M. & Loehrke, R. (1979). Stratified thermal storage in residential solar energy applications. *Journal of Energy*, *3*(2), 106–113.

Sheridan, N., Bullock, K. & Duffie, J. (1967). Study of solar processes by analog computer. *Solar Energy*, *11*(2), 69–77.

Shukla, R., Sumathy, K., Erickson, P. & Gong, J. (2013). Recent advances in the solar water heating systems: A review. *Renewable and Sustainable Energy Reviews*, *19*, 173–190.

Shyu, R. & Hsieh, C. (1987). Unsteady natural convection in enclosures with stratified medium. *Journal of Solar Energy Engineering*, *109*(2), 127-133.

(SIA), S. I. A. (2004). *Code of practice for manufacture and installation of solar water heating systems in new zealand* (Tech. Rep.).

Sparrow, E. & Charmchi, M. (1983). Natural convection experiments in an enclosure between eccentric or concentric vertical cylinders of different height and diameter. *International Journal of Heat and Mass Transfer*, *26*(1), 133–143.

Steinberner, U. & Reineke, H.-H. (1978). Turbulent buoyancy convection heat transfer with internal heat sources. In *International heat transfer conference digital library.* Begel House Inc.

Thomas, R. & de Vahl Davis, G. (1970). *Natural convection in annular and rectangular cavities. a numerical study.* (Tech. Rep.). University of New South Wales.

Tsukaguchi, Y., Nakamura, O., Jonsson, P., Yokoya, S., Tanaka, T. & HARA, S. (2007). Fluent 6.0 user's guide fluent 6.0 user's guide, 2001. *ISIJ international*, *47*(10), 1436–1443.

Tu, J., Yeoh, G. H. & Liu, C. (2018). *Computational fluid dynamics: a practical approach*. Butterworth-Heinemann.

Wagner, W. & Kretzschmar, H.-J. (2008). Iapws industrial formulation 1997 for the thermodynamic properties of water and steam. *International steam tables: properties of water and steam based on the industrial formulation IAPWS-IF97*, 7–150.

Wang, S. & Davidson, J. H. (2015). Selection of permeability for optimum performance of a porous tube thermal stratification manifold. *Solar Energy*, *122*, 472–485.

Wang, S. & Davidson, J. H. (2017). Performance of a rigid porous-tube stratification manifold in comparison to an inlet pipe. *Solar Energy*, *146*, 298–308.

Watmuff, J., Charters, W. & Proctor, D. (1977). Solar and wind induced external coefficients-solar collectors. *Cooperation Mediterraneenne pour l'Energie Solaire*, 56.

Weiss, W. & Spörk-Dür, M. (2020). Solar heat worldwide, global market development and trends in 2019. *IEA Solar Heating and Cooling Programme*.

Willis, G. & Deardorff, J. (1965). Measurements on the development of thermal turbulence in air between horizontal plates. *The Physics of Fluids*, *8*(12), 2225–2229.

Yang, J., Li, J. & Feng, R. (2019). Heat loss analysis and optimization of household solar heating system. *Heat Transfer Research*, *50*(7).

Yu, Y. (2020). *An energy balance based analysis of solar domestic hot water systems* . (PhD thesis)

Zachar, A., Farkas, I. & Szlivka, F. (2003). Numerical analyses of the impact of plates for thermal stratification inside a storage tank with upper and lower inlet flows. *Solar Energy*, *74*(4), 287–302.

Zurigat, Y. H., Liche, P. R. & Ghajar, A. J. (1991). Influence of inlet geometry on mixing in thermocline thermal energy storage. *International Journal of Heat and Mass Transfer*, *34*(1), 115–125.

Appendix A

Uncertainty Analysis

A.1 Uncertainty in temperature measurement

All experimental results are subject to a certain variation due to errors in the measurement process. The presence of errors is imminent in experiments due to the limitations of the experimental apparatus such as thermocouple in temperature measurements or PIV system in velocity measurements.

The data acquisition system used to record temperature measurements is the PICO-LOG TC-08 that uses a 20-bit digital analogue converter with a resolution of 0.025°C. According to the specifications, the factory calibration results indicated that the accuracy of the equipment is compromised at 0.2% of readings plus 10 V. As discussed previously, the relative results are more important than the absolute ones in this study, which means that the precision of the measurement is determinant of errors and not the accuracy. The offset error of 10 V does not directly affect the results since all temperature points are measured with the same instrument and in the same way. Therefore, the uncertainty associated with the resolution of the data acquisition system can be taken as $\pm 0.025C$.

To determine the temperature profile along the height of the tank, a series of copper-constantan (Type-T) thermocouples were used. All thermocouples used were 3 mm

T-type thermocouples. The thermocouples were calibrated against a platinum resistance thermometer, having an accuracy of $\pm 0.02C$, using a temperature-controlled circulating water bath. For the calibration, five temperature points in the range of 30°C to 80°C were chosen. The standard deviation for the thermocouples was shown to be less than 1.2°C.

According to Moffat (1988), the mentioned uncertainties can be combined through Equation (57). This gives an overall value of the uncertainties of the temperature measurements, σ_T which includes uncertainties due to the data acquisition system (D) and the thermocouples (Th).

$$\sigma_T = \sqrt{(\sigma_{Th})^2 + (\sigma_D)^2} \tag{57}$$

Considering the accuracy of both platinum resistance thermometer and that of the thermocouples, the uncertainty of the temperature sensors was taken to be approximately $\pm 1.22C$.

Given that the thermocouples were small in size, fixed at the centre of the tank, and the flow inside the tank exhibits low velocity magnitudes, the true value of temperature is taken as the value of the fluid temperature at the junction of the thermocouple. It is important to note that in the absolute values of temperatures do not interfere with the results obtained from the experiment. This means that if the experimental apparatus had any systematic error, measured results would have little influence on the findings since all the measurements were made using the same apparatus and procedures.

A.2 Uncertainty in PIV measurements

The magnification of an image is used to convert the pixels on the image to actual physical distance along which the particles move. When the particles move on the centre of the plane which is calibrated, there is no magnification error. However, if particles are travelling on the far side of the laser sheet, the object distance from the lens is increased by half of the laser sheet thickness, as shown in Figure 83. This results in a magnification error, σ_M that is proportional to the laser sheet thickness, δ_{z_o} divided by the object distance, Z_o (see Equation 58).

$$\sigma_M = \delta z_o / Z_o \tag{58}$$

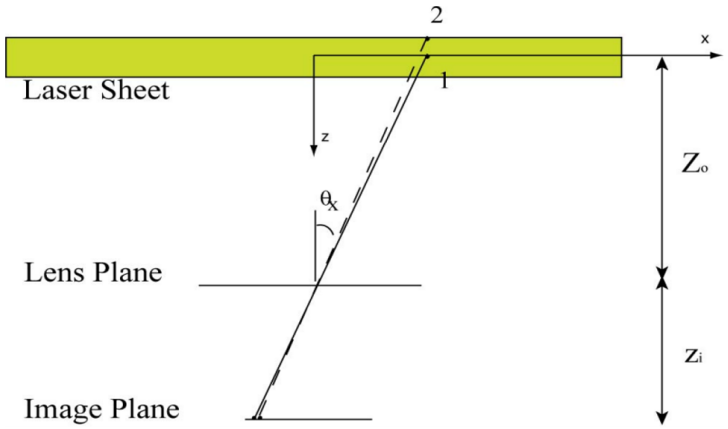

Figure 83: Visualization of magnification error (Raffel et al., 1998)

Given that the laser sheet thickness used in the experiment was 1 mm while the lens was positioned at 1.5 m away from the calibration plane (i.e. centre of laser sheet), the magnification error of particle on the back side of the laser sheet was determined to be 0.07 %. Adrian and Westerweel (2011) pointed out that the variation in magnification directly impacts the measured velocity and suggested that the its uncertainty can be taken as the uncertainty of measured velocities which is approximately $\pm 0.0007 m/s$.

A.3 Uncertainty in predicted thermal efficiency

Thermal efficiency of a storage tank is calculated using Equation (59).

$$\eta = \frac{\dot{q}_{useful} - \dot{q}_{loss}}{\dot{q}_{useful}} \tag{59}$$

Considering the sources of uncertainty in the mathematical modelling of a storage tank in Chapter 6, it is evident that the only source of error is from the rate of heat loss as it utilizes the developed Nusselt number correlations for Configuration A, B and C, as shown in Equation (60) and (61).

$$\dot{q}_{loss} = -\frac{A_{total}(\bar{T}_f - \bar{T}_w)}{R_{i,conv}} - \dot{m}_L c_{p,f}(\bar{T}_f - T_L) \tag{60}$$

$$\dot{q}_{loss} = -\frac{A_{total}(\bar{T}_f - \bar{T}_w)\bar{N}uk_f}{L_c} - \dot{m}_L c_{p,f}(\bar{T}_f - T_L) \tag{61}$$

Given that the margin of uncertainty for the developed Nusselt correlations is 15%, the uncertainty associated with the rate of heat loss was also considered to be 15%. The resulting uncertainty values for thermal efficiency of different tank configurations was tabulated in Table (9 - 11).

Table 9: Uncertainty of the predicted thermal efficiency for Configuration A

Month	**Uncertainty of η**
Jan	0.79%
Feb	0.84%
Mar	0.87%
Apr	0.88%
May	0.91%
Jun	0.86%
Jul	0.86%
Aug	0.85%
Sep	0.87%
Oct	0.88%
Nov	0.81%
Dec	0.82%

Table 10: Uncertainty of the predicted thermal efficiency for Configuration B

Month	**Uncertainty of η**
Jan	0.82%
Feb	0.84%
Mar	0.82%
Apr	0.82%
May	0.91%
Jun	0.86%
Jul	0.87%
Aug	0.81%
Sep	0.89%
Oct	0.92%
Nov	0.76%
Dec	0.83%

Table 11: Uncertainty of the predicted thermal efficiency for Configuration C

Month	**Uncertainty of η**
Jan	0.86%
Feb	1.07%
Mar	0.95%
Apr	1.04%
May	0.88%
Jun	1.12%
Jul	1.17%
Aug	1.42%
Sep	1.09%
Oct	0.79%
Nov	0.86%
Dec	1.03%

Appendix B

Transient heat loss from rectangular storage tank

B.1 Mesh and time independence analysis of CFD model

Given that experimental setup used for validation of transient heat loss was for rectangular tank, it was necessary to develop a CFD model with the same configuration. The whole flow domain was paved with a coarse mesh with a maximum grid size of 15 mm except the regions close to the tank wall where concentrated grid points were created by inflating the grid with 10 layers having a first-layer thickness of 0.05 mm and a growth rate of 1.2. Figure 84 shows the mesh used for the developed CFD model.

A grid convergence index (GCI) with a safety factor of 3 was applied for the grid independence analysis, as suggested by Roache (1998). Two grid sizes having maximum cell sizing of 15 mm and 7.5 mm were chosen for the GCI analysis. The calculated GCI between the coarsest and finest mesh with respect to average temperature of the tank showed a maximum error of 1.5%, indicating that a mesh with the maximum cell sizing of 15 mm, as shown in Figure 85, was satisfactory.

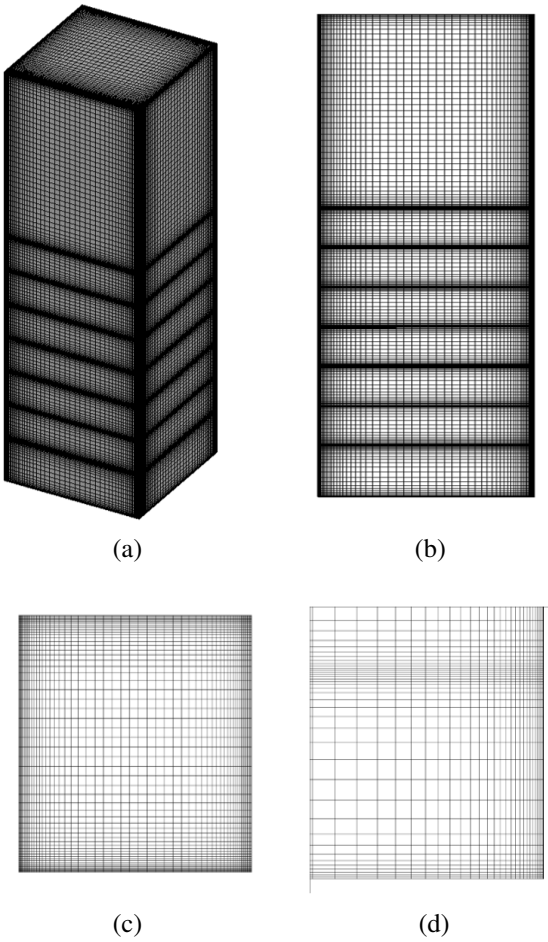

Figure 84: Mesh of developed vertical rectangular CFD tank model (a) isometric view, (b) side view, (c) top view and (d) enlarged view of the corner region

To ensure that the solution was independent of the time step size, solution time intervals in the order of 1-2 s were used as suggested in the study of (Bejan, 2013). From Figure 86, it can be observed that a time step of 1.25 s was shown to be adequate for this study.

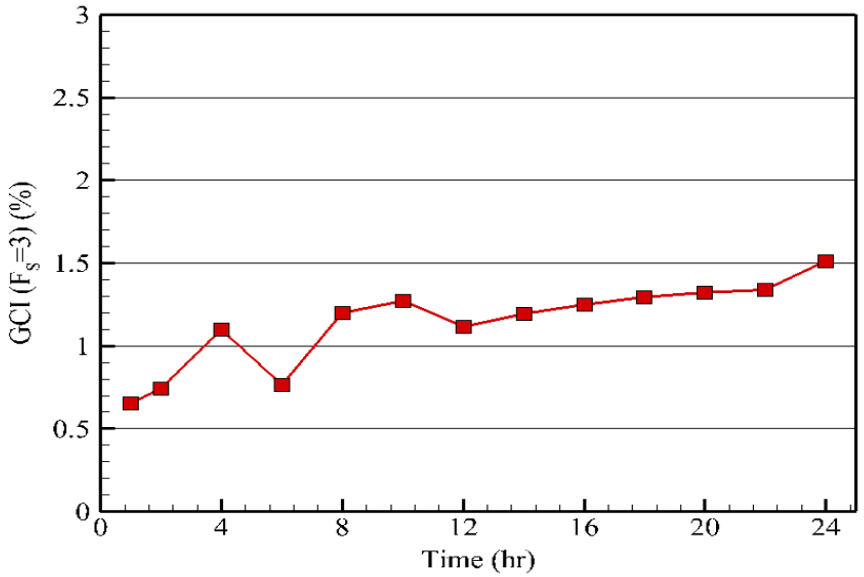

Figure 85: GCI variation of the average temperature of the tank during 24 hr standby period

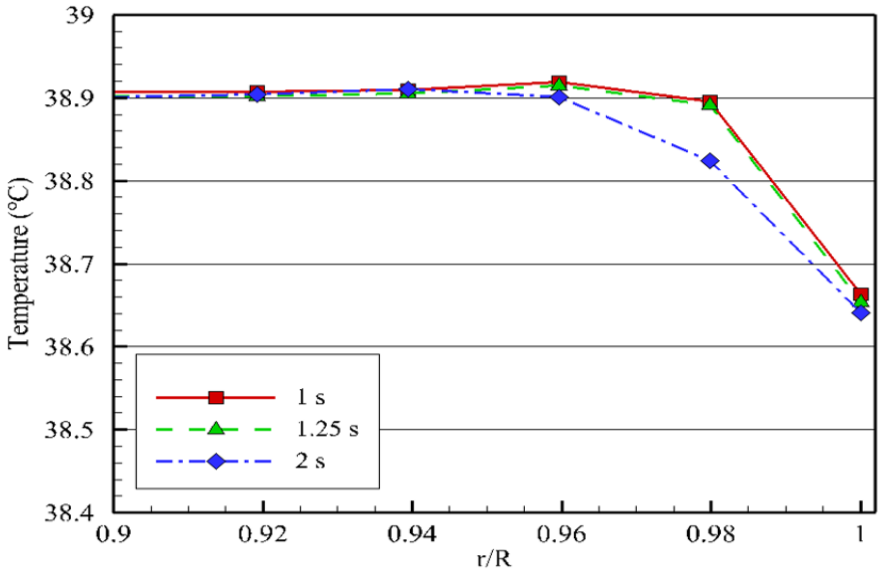

Figure 86: Horizontal temperature variation with solver steps at the height of 0.61 m after 1 hr of cooling

B.2 Boundary condition of CFD model

Given that experimental setup used for validation of transient heat loss was for rectangular tank, it was necessary to develop a CFD model with the same boundary conditions. For ease of comparison with experimental data, the tank model was segmented into eight sections, as shown in Figure 87.

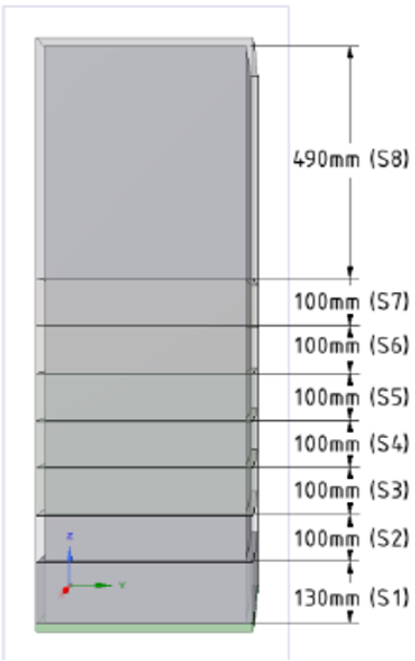

Figure 87: Rectangular CFD tank model along with the divided sections

To specify external heat loss coefficients corresponding to the experiment, measured rate of change of water temperature in each section was fitted based on Newton's law of cooling, as suggested by Mawire and Taole (2013).

As such, the rate of change of temperature of a section can be estimated by an exponential decay given by Equation (62).

$$\frac{\partial T_{f,j}}{\partial t} = -au({T^o}_{f,j} - T_{env})e^{-at} \tag{62}$$

Where, a is a constant.

The rate of heat loss from the tank can be written as Equation 63.

$$\rho_{f,j} c_{p,f,j} A_s H_j \frac{\partial T_{f,j}}{\partial t} = U_j A_s (T^o{}_{f,j} - T_{env}) \tag{63}$$

Hence, the overall heat transfer coefficient of a section, U_j can be expressed as shown in Equation 64.

$$U_j = \frac{1}{\frac{1}{h_{i,conv}} + \frac{L_w}{k_w} + \frac{1}{h_{e,conv}}} \tag{64}$$

In addition, convective boundary conditions were imposed on the outer walls as well as the top and bottom ends to simulate static operation.

At the top and bottom walls, this was given by Equation (65).

$$-k_w \frac{\partial T_w}{\partial h} = h_{e,conv}(T_w - T_{env}) \tag{65}$$

And at the side wall, by Equation (66), where T_{wall} is the tank wall temperature.

$$-k_w \frac{\partial T_w}{\partial x} = h_{e,conv}(T_w - T_{env}) \tag{66}$$

Since the external heat transfer coefficient for each section needs to be specified in the CFD model, they were iteratively adjusted using Equation (64) with known internal convective heat transfer coefficients and fixed heat conduction resistance until the computed overall heat transfer coefficients (U_j) matches those in the experiment, over the sampling period of 24 hours. The obtained external heat transfer coefficients (see Table 12) along with measured ambient temperatures were specified by means of User Defined Function.

Table 12: External heat transfer coefficient specified in the CFD model

Tank section	**Averege** $U\ (W/K)$		**Specified** $h_{e,conv}\ (W/m^2K)$
-	Experiment	CFD	-
S1	1.5680	1.5609	8.0
S2	0.9186	0.9189	11.0
S3	0.8259	0.8280	9.0
S4	0.7594	0.7584	7.7
S5	0.7162	0.7163	7.0
S6	0.6826	0.6843	6.5
S7	0.6596	0.6574	6.1
S8	3.2043	3.2018	3.1

Appendix C

Steady state heat loss from rectangular storage tank

C.1 Mesh and time independence analysis of CFD model

To validate the CFD method using experimental data of Steinberner and Reineke (1978), who investigated steady state cooling of rectangular tank, a rectangular CFD tank model having Rayleigh number, $Ra_{i,gen}$ of 1.56 × 10^{13} was developed. This Rayleigh number represents the tank height of 0.6 m and volume of 216 L The whole flow domain was paved with a coarse mesh with a maximum grid size of 15 mm except the regions close to the tank wall where concentrated grid points were created by inflating the grid with 10 layers having a first-layer thickness of 0.05 mm and a growth rate of 1.2, as shown in Figure 88.

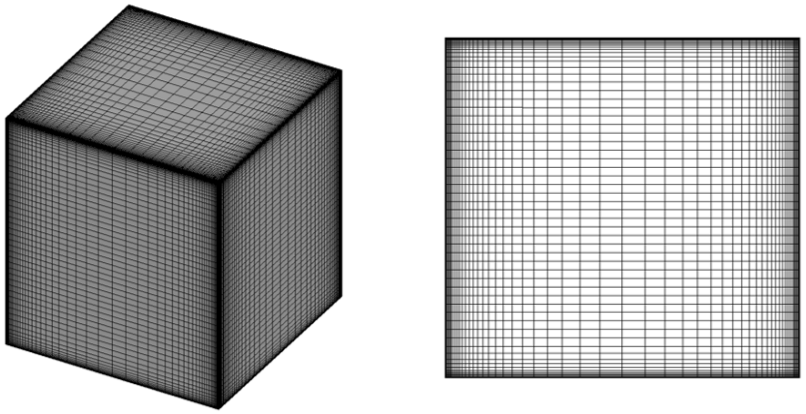

(a) (b)

Figure 88: Mesh of developed rectangular CFD tank model (a) isometric view and (b) side view

Mesh sensitivity analysis was performed using the Grid Convergence Index (GCI) proposed by (Roache, 1998) with two different grids having maximum cell sizes of 15 mm and 7.5 mm. Since the order of the solver method (p_m)nd the mesh refinement ratio (r_m)re equal to 2 in this study, the GCI with the safety coefficient (F_s) 3 directly reflects the relative error of the solutions obtained from two different meshes. The GCI observed based on the temperature of the storage tank model was only 0.013% between the finer and coarse grid sizes, indicating that a mesh with 15 mm cell size, was adequate.

Appendix D

Energy balances for convective cooling of a nodal storage tank model

The rate of change of temperature of water for the top node, intermediate nodes and bottom node can be calculated using Equations (67-69).

$$\frac{dT_{f,t}}{dt} = \frac{\left[\frac{A_t(T_{f,t}-T_{w,t})}{R_{i,conv}}\right]}{\rho_f V_f c_{p,f}} \tag{67}$$

$$\frac{dT_{f,j}}{dt} = \frac{\left[\frac{A_{s,j}(T_{f,j}-T_{w,j})}{R_{i,conv}}\right]}{\rho_f V_f c_{p,f}} \tag{68}$$

$$\frac{dT_{f,b}}{dt} = \frac{\left[\frac{A_b(T_{f,b}-T_{w,b})}{R_{i,conv}}\right]}{\rho_f V_f c_{p,f}} \tag{69}$$

Where j = 2...(n-1), $T_{f,t}$, $T_{f,i}$, $T_{f,b}$ are water temperatures of top, intermediate and bottom nodes (°C) and the internal convection resistance, $R_{(i,conv)}$ can be represented, as shown in Equation (70).

$$R_{i,conv} = \frac{1}{\bar{h}_{i,conv}} \tag{70}$$

The rate of change of temperature of wall for the top node, intermediate nodes and bottom node can be calculated using Equations (71-73).

$$\frac{dT_{w,t}}{dt} = \frac{\left[\frac{A_t(T_{f,t}-T_{w,t})}{R_{i,conv}} - \frac{A_t(T_{w,t}-T_{env})}{R_{w,cond}+R_ins,cond+R_{e,conv}}\right]}{\rho_w V_w c_{p,w}} \tag{71}$$

$$\frac{dT_j}{dt} = \frac{\left[\frac{A_{s,i}(T_{f,j}-T_{w,j})}{R_{i,conv}} - \frac{A_{wall,i}(T_{w,j}-T_{env})}{R_{w,cond}+R_ins,cond+R_{e,conv}}\right]}{\rho_w V_w c_{p,w}} \tag{72}$$

$$\frac{dT_{w,b}}{dt} = \frac{\left[\frac{A_b(T_{f,b}-T_{w,b})}{R_{i,conv}} - \frac{A_b(T_{w,b}-T_{env})}{R_{w,cond}+R_ins,cond+R_{e,conv}}\right]}{\rho_w V_w c_{p,w}} \tag{73}$$

Where, $R_w, cond$ can be represented, as shown in Equation (74).

$$R_{w,cond} = \frac{L_w}{k_w} \tag{74}$$

Where,$R_{ins,cond}$ and external convection resistance, $R_{e,conv}$ can be represented, as indicated in Equation (75) and (76).

$$R_{ins,cond} = \frac{L_{ins}}{k_{ins}} \tag{75}$$

$$R_{e,conv} = \frac{1}{h_{e,conv}} \tag{76}$$

For the developed correlation, the Rayleigh number can be defined, as shown in Equation (77).

$$Ra = \frac{g\beta_f(\bar{T}_{f,n} - \bar{T}_{w,n})H^3}{\upsilon_f \alpha_f} \tag{77}$$

Where, $T_{f,n}$ is the average water temperature of all the nodes defined, as shown in

Equation (78).

$$\bar{T}_{f,n} = \frac{T_{f,t} + \sum_{j=2}^{n-1} T_{f,j} + T_{f,b}}{5} \tag{78}$$

Where, $T_{w,n}$ is the average wall temperature of all the nodes defined, as shown in Equation (79).

$$\bar{T}_{w,n} = \frac{T_{w,t} + \sum_{j=2}^{n-1} T_{w,j} + T_{w,b}}{5} \tag{79}$$

Appendix E

Steady state heat loss from cylindrical storage tank with air gap

E.1 Boundary condition of CFD model

Given that experimental setup used for validation of transient heat loss was for cylindrical tank with a draft of 88° from the horizontal line, it was necessary to develop a CFD model with the same boundary conditions. For ease of comparison with experimental data, the tank model was segmented into six sections, as shown in Figure 89.

Since the external heat transfer coefficient for each section needs to be specified in the CFD model, they were iteratively adjusted using Equation (80) with known internal convective heat transfer coefficient, heat transfer resistance across the air gap and fixed heat conduction resistance until the computed overall heat transfer coefficients U_j matches those in the experiment, over the sampling period of 24 hours. The obtained external heat transfer coefficients (see Table 13) along with measured ambient temperatures were specified by means of User Defined Function.

$$U_j = \frac{1}{\frac{1}{h_{i,conv}} + \frac{L_{w1}}{k_{w1}} + R_{air,total} + \frac{L_{w2}}{k_{w2}} + \frac{1}{h_{e,conv}}} \tag{80}$$

Given that temperature of water inside the inner cylindrical tank was measured, it was included as part of the computational domain to validate the CFD method used. For the included computational domain of water inside the tank, laminar flow model was used to simulate its flow and heat transfer. This is because Rayleigh number for the current study results in Ra < 10^{12}, which was shown in Chapter 2 that for this range of Rayleigh number, the assumption of laminar flow regime in CFD methodology is valid.

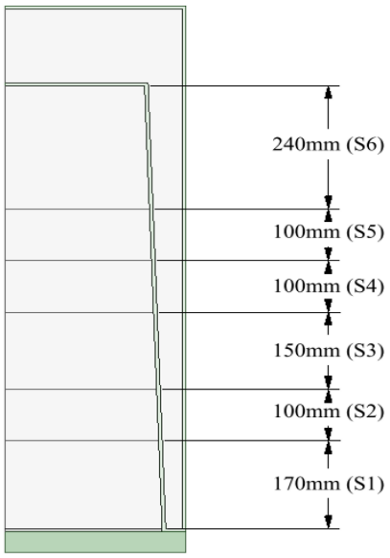

Figure 89: Cylindrical CFD tank model with air gap insulation along with the divided sections

For accurate validation of the CFD method with experimental data, radiation heat transfer inside the air gap was also taken into consideration by using Discrete Ordinates (DO) radiation model, assuming optical thickness of 1 which has been shown to be valid for vertical annulus, having aspect ratios from 1 to 10 and radius ratios from 1.25 to 10, especially when radiation is only one of the heat transfer modes by (Weng and Chu, 1996).

Table 13: External heat transfer coefficient specified in the CFD model

Tank section	**Averege** $U\ (W/K)$		**Specified** $h_{e,conv}\ (W/m^2K)$
-	Experiment	CFD	-
S1	1.9927	1.9512	18.0
S2	0.9674	0.9598	15.0
S3	1.3571	1.3328	20.0
S4	0.8421	0.8387	17.0
S5	0.8151	0.8172	13.5
S6	1.8908	1.8903	14.5

E.2 Mesh and time independence analysis of CFD model

Given that experimental setup used for validation of transient heat loss was for cylindrical tank with a draft of 88° from the horizontal line, it was necessary to develop a CFD model with the same configuration. The whole flow domain was paved with a coarse mesh with a maximum grid size of 4 mm except the regions close to the tank wall where concentrated grid points were created by inflating the grid with 15 layers having a first-layer thickness of 0.1 mm and a growth rate of 1.2. Figure 90 shows the mesh used for the developed CFD model.

A grid convergence index (GCI) with a safety factor of 3 was applied for the grid independence analysis, as suggested by (Roache, 1998). Two grid sizes having maximum cell sizing of 4 mm and 2 mm were chosen for the GCI analysis. The calculated GCI between the coarsest and finest mesh with respect to average temperature of the tank showed a maximum error of 0.2% (see Figure 91) indicating that a mesh with maximum cell sizing of 4 mm, as shown in Figure 88, was satisfactory.

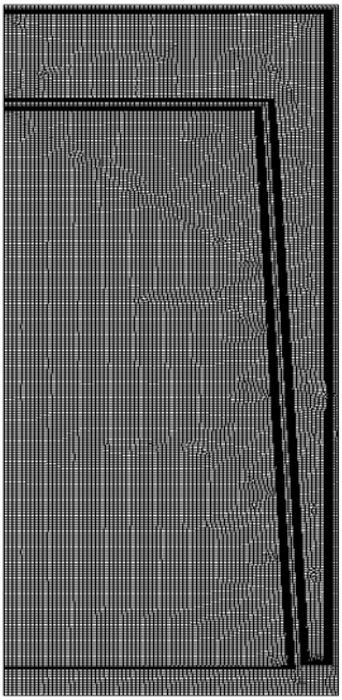

Figure 90: Mesh of developed cylindrical CFD tank model with air gap insulation

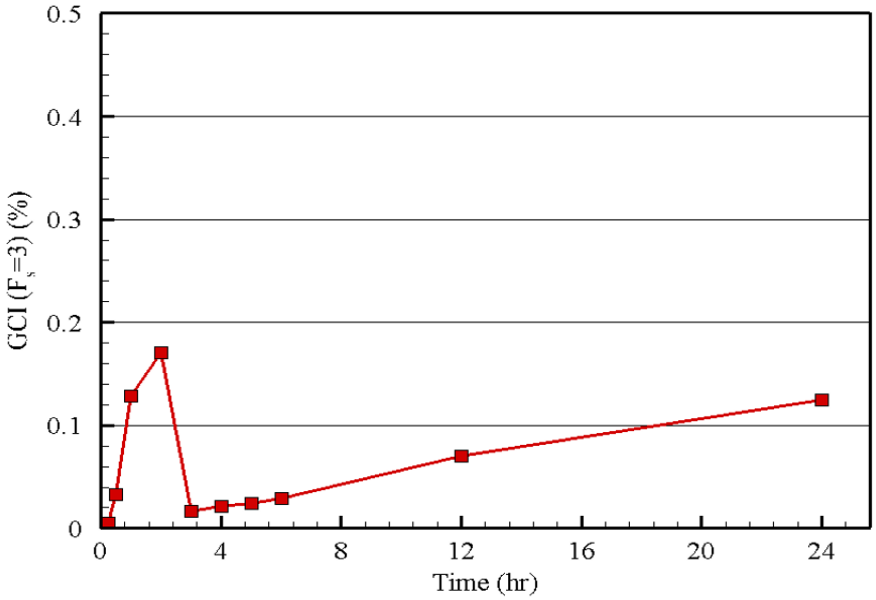

Figure 91: Mesh of developed cylindrical CFD tank model with air gap insulation

To ensure that the solution was independent of the time step size, solution time intervals in the order of 0.05-0.2 s were used, as suggested in the study of Bejan, (2013).

Figure 92 shows CFD predictions of horizontal temperature variation at the height of 0.25 m for different time steps after 1 hour since the start of the test. The result show that the time step of 0.1 s is a good compromise between numerical accuracy and computational cost, hence chosen for this study.

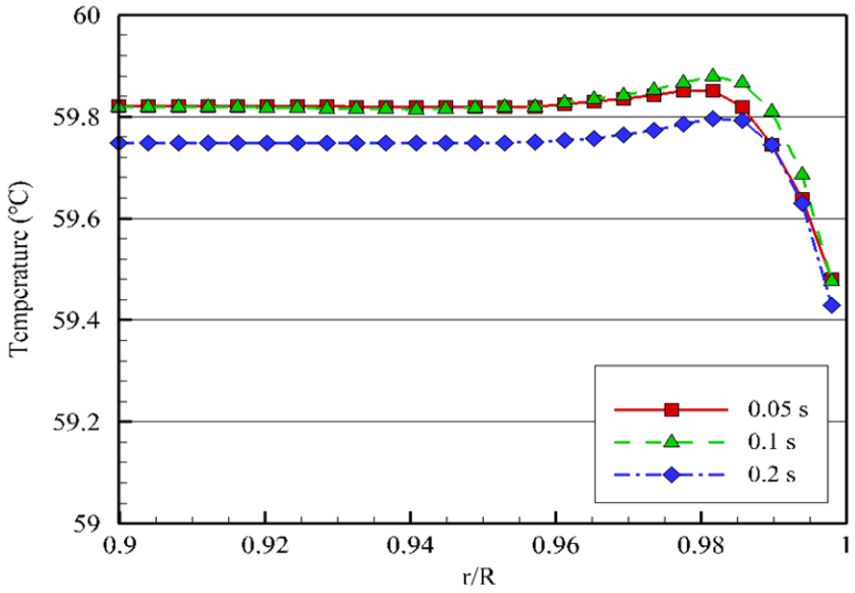

Figure 92: Mesh of developed cylindrical CFD tank model with air gap insulation